Huttunen, Tomi. The ultra weak variational formulation for ultrasound transmission problems. Kuopio University Publications C. Natural and Environmental Sciences 168. 2004. 159 p.

ISBN 951-781-306-6 and 971-27-0001-8 (PDF)
ISSN 1235-0486

ABSTRACT

Linear time-harmonic wave fields in fluids and solids can be characterized by the Helmholtz and Navier equations. Due to the oscillatory nature of the solution, the numerical approximation of wave equations is difficult. To approximate Helmholtz or Navier problems with a tolerable accuracy, a relatively dense spatial discretization must be used. For standard numerical techniques, such as low order finite difference (FD) and finite element (FE) methods, ten points per wavelength is considered as a rule of thumb. Particularly, at ultrasound frequencies in which the wavelength is short, the requirement of a dense mesh can lead to problems with unbearable computational complexity. Fortunately, the computational burden can be reduced by including a priori information of the solution to the approximate subspace of the numerical method. A promising technique for this is the ultra weak variational formulation (UWVF).

In this thesis, the UWVF method is applied to the modeling of ultrasound fields in an inhomogeneous medium. More precisely, the main focus is to develop the UWVF method feasible for the modeling of wave fields in biomedical ultrasonics. The method is examined for two- and three-dimensional Helmholtz problems; and two-dimensional Navier problems. Furthermore, the perfectly matched layer (PML) is used to truncate the computational domain in the three-dimensional Helmholtz problems.

Two practical examples using the Helmholtz model are investigated. In the first case, anomalies due to the needle and membrane hydrophones to continuous wave ultrasound field are simulated. The results indicate that especially in the case of membrane hydrophones, notable standing waves are generated between the membrane and the transducer. Standing waves also contribute a periodic anomaly to the simulated measurement of the hydrophone. In the second example, transmitted ultrasound fields through layered plastic plates are simulated for different incident angles of the sound beam. These results are compared with experimental measurements. Simulated fields have a reasonable agreement with experiments at low angles of incidence but the Helmholtz model becomes insufficient for simulating ultrasound fields in plates at large angles of incidence.

AMS Classification: 74J05, 74J20, 74S30, 76Q05
Universal Decimal Classification: 534-8, 534.2
National Library of Medicine Classification: QT 34,WN 208,WB 515
INSPEC Thesaurus: acoustics; ultrasonics; ultrasonic waves; ultrasonic transmission; elastodynamics; wave equations; Helmholtz equation; numerical analysis; modeling

Acknowledgments

The work for this thesis has been carried out at the Department of Applied Physics in the University of Kuopio in 2000-2004; and during visits at the Department of Mathematical Sciences in the University of Delaware in 1999-2000 and at the Brigham and Women's Hospital in the Harvard Medical School in 2001-2002.

I wish to express my gratitude to my principal supervisor Prof. Jari Kaipio for suggesting me this interesting topic and for providing tireless guidance during the project. In addition, my great appreciation belongs to my other supervisors Prof. Peter Monk and Prof. Kullervo Hynynen, especially, for giving me an opportunity to work at their research groups. In addition, I thank Peter Monk for numerous ideas which I have tried to implement in this thesis and Kullervo Hynynen for the valuable guidance to medical ultrasonics and for helping with the experimental part of the thesis. I also want to thank Jason White (and others) from the Focused Ultrasound Group in the Brigham and Women's Hospital, who conducted the experimental measurements presented in this thesis.

In the final part for finishing this thesis, the official pre-examiners Prof. Jeremy Astley and Dr. Erkki Heikkola gave fruitful suggestions and comments for improving the manuscript.

Along with the faculty and staff of the Department of Applied Physics, I wish to thank Antti Vanne for solving all (and those are not few) computer related problems during this project and Matti Malinen for valuable discussions and comments of many details of the thesis.

Naturally my invaluable gratitude belongs to my family, all friends and relatives, and last but not least, my dearest appreciation goes to my wife Joanna.

This study has been supported by the Academy of Finland, Fulbright Center, Saastamoinen Foundation, Cultural Foundation of Northern Savo, and Jenny and Antti Wihuri Foundation.

Kuopio, January 24th 2004

Tomi Huttunen

Abbreviations

2D	Two dimensional
3D	Three dimensional
ABC	Absorbing boundary condition
BEM	Boundary element method
Bi-CG	Bi-conjugate gradient
Bi-CGStab	Stabilized bi-conjugate gradient
CFL	Courant-Friedrichs-Levy number
CT	Computer tomography
CW	Continuous wave
DEM	Discontinuous enrichment method
DGM	Discontinuous Galerkin method
DOF	Number of degrees of freedom
DtN	Dirichlet-to-Neumann
EPAM	Equivalent phased array method
Err	Relative error
FD	Finite difference
FDTD	Finite difference time domain
FE	Finite element
FEM	Finite element method
FMM	Fast multipole method
FUS	Focused ultrasound surgery
GLS	Galerkin least-squares
MPI	Message passing interface
MRI	Magnetic resonance imaging
NRBC	Non-reflecting boundary condition
PC	Personal computer
PDE	Partial differential equation
PML	Perfectly matched layer
PUM	Partition of unity
PVDF	Polyvinylidene fluoride
PZT	Lead zirconate titanate
RAM	Random access memory
SEM	Spectral element method
UWVF	Ultra weak variational formulation

Nomenclature[1]

a	Unit direction vector
	Bilinear equation $a(p, v)$, 3.2.2
A	Amplitude of a complex valued field, 8.3
A_k	Complex weight coefficient, 3.3
	PML matrix, 3.1.3
b	Unit direction vector
	Right hand side of the UWVF equation, 4.1.1
c	Speed of sound, 2.3
c_P, c_S	Speed of P- and S-waves, 2.2
c_R	Speed of Rayleigh wave, 2.6
C	UWVF matrix, 4.1.1
d	Unit direction vector (d_x, d_y, d_z)
	Spatial dimension, 2.5
	Distance, 7.3
d_x, d_y, d_z	Derivatives of complex stretched variables, 3.1.3
D	UWVF matrix, 4.1.1
D_k	Block of D corresponding to the kth element, 4.1.1
$D_{\xi\xi}$	FD difference operator, 3.2.1
D_F	Diameter of the PVDF film, 7.2
D_N	Diameter of the needle hydrophone, 7.2
E	Young's modulus, 2.2
E'	Real part of E, 2.2
E''	Imaginary part of E, 2.2
f	Frequency, 2.2
f_s	Source term, 3.1.3
F	Body force, 2.1
F_n	Arbitrary function, 3.3
F_k	UWVF operator on ∂K_k, 4.1
g	Boundary source, 3.2.2
h	FD grid size, 3.2.1
	FE element diameter, 3.2.2
h_k^{av}	Average radius of the element K_k, 6.3.3
H	System matrix for the discrete Rayleigh integral, 8.1
i	Imaginary unit $\sqrt{-1}$
I	Unit vector/matrix/tensor
$\Im$	Imaginary part
j	Integer
J	Integer
k	Integer
K_k	kth finite element, 4.1

[1]The number following a line shows the section in which the symbol is first used.

ℓ	Integer
L	Length of the computational domain, 7.2
	Right hand side of the bilinear equation, 3.2.2
L^2	Space of square integrable functions
L_j	Plane wave basis of the FEM, 3.3
m_j	Dirichlet to Neumann kernel, 3.1
M	Dirichlet to Neumann operator, 3.1
	Number of vertices of a FE mesh, 3.2.2
	Integer
M_k	Number of entries in D and C corresponding to the element K_k, 6.2
M_N	Approximate Dirichlet to Neumann operator, 3.1.1
n	Normal vector, 2.4
	Integer
N	Number of finite elements, 3.2.2
	Integer
N_k	Number of scalar basis in the kth element, 4.1.1
N_k^P, N_k^S	Number of P- and S-wave basis functions in the kth element, 4.2.1
p	Time-harmonic acoustic pressure, 2.3
P	Pressure, 2.3
Q	Boundary parameter, 3.2.2
r	Spatial variable $r = (x, y, z)$
	Residual vector, 5.1.3
r'	Spatial variable after deformation, 2.2
	Complex stretched spatial variable, 3.1.3
R	Radial term of polar coordinates (R, θ, ϕ), 2.5
	Radius of the computational domain, 7.2
R_S	Radius of the transducer, 7.2
$\Re$	Real part
s	Entropy, 2.3
	Tangential vector
S	Surface of the transducer, 6.3.3
t	Time
t_R	Relaxation time, 2.3
T	Traction operator, 2.4
$\top$	Transpose
u	Time-harmonic displacement (u_x, u_y, u_z), 2.2
u_P, u_S	Time-harmonic P- and S-wave displacements, 2.2
U	Displacement, 2.2
v	Test function, 3.2.2
v_n	Normal particle velocity, 6.3.3
v^P, v^S	P- and S-wave basis functions, 4.2.1
V	Particle velocity, 2.1
y_k	UWVF impedance functional on ∂K_k, 4.1
X	Vector $X = (\chi_{1,1}, ..., \chi_{k,1}, ..., \chi_{K,N_K})^\top$, 4.1.1

α	Acoustic absorption coefficient, 2.3
α_P, α_S	Acoustic absorption coefficient for P- and S-wave, 2.3
	Decay factors of the Rayleigh wave, 2.6
β	Vector $\beta = (\beta_1, .., \beta_j, ..., \beta_N)^\top$
β_j	FEM coefficient associated with jth node, 3.2.2
	Sequence of random numbers, 5.1.3
γ	Regularization parameter, 8.1
Γ	Exterior boundary of the computational domain, 3.1
δ	Acoustic density, 2.1
δ_ω	Time-harmonic acoustic density, 2.3
ϵ	Strain tensor, 2.2
	Small number, 5.1.3
η	PML parameter $\eta = d_x d_y d_z$, 3.1.3
θ	Angle, 3.1.1
	Parameter κh, 3.2.2
λ	Wavelength
Λ	First Lamé coefficient, 2.2
μ	Second Lamé coefficient, 2.2
μ_f	Viscosity, 2.3
ν	Poisson ratio, 2.2
κ	Wave number, 2.3
κ_P, κ_S	P- and S- wave numbers, 2.2
κ_R	Rayleigh wave number, 2.6
ρ	Mass density, 2.1
σ	Coupling parameter for impedance boundary condition, 3.2.2
	Standard deviation, 8.3
$\sigma_0, \sigma_{0,\xi}$	PML decay parameters, 3.1.3
$\sigma_x, \sigma_y, \sigma_z$	PML decay functions, 3.1.3
$\Sigma_{k,j}$	Interface between jth and kth finite element or subdomain, 2.4, 4.1
τ	Stress tensor, 2.1
ϕ	Angle in polar coordinates (R, θ, ϕ)
	Basis function, 4.1.3
	Phase of a complex valued wave field
Φ	Fundamental solution of the Helmholtz equation, 3.2.3
φ	FEM/UWVF basis function, 3.2.2
χ	Unknown function in the UWVF, 4.1
ω	Angular frequency, 2.2
Ω	Domain, 2.2

Contents

Chapter I

Introduction

Among the fields of computational physics, the modeling of mechanical wave problems is especially challenging. This is due to the oscillatory nature of solutions of the partial differential equations (PDE) which characterize the behavior of the wave fields. Only few wave problems have analytical solutions, and the performance of standard numerical methods for PDEs is related to the wavelength of sound field. In particular at high frequencies, the requirement of a certain number of discretization points per wavelength often leads to an unbearable computational burden. Consequently, instead of using full-wave methods, ray-tracing type techniques have been used in many applications. However, these techniques are not always sufficient to capture the complex phenomena related to wave fields in a general geometry and medium.

The need for accurate methods for modeling mechanical wave fields at high wave numbers in complex geometries is evident. Obvious applications for such a method are, for example, non-destructive testing, exploration seismology and medical ultrasonics. The main focus of this thesis is in computational methods that are feasible for the modeling of wave fields in biomedical ultrasonics. In particular, renewed interest in utilizing focused ultrasound fields for therapeutic purposes has caused a growing need to model accurately wave fields in biological tissues.

The idea of using focused ultrasound fields to destroy deep-seated tissue was first introduced in the 1940's [142]. In this method, the focused ultrasound beam is aimed to target tissue in which the absorption of the sound causes local temperature elevation destroying the tissue. Due to the short wavelength of the ultrasound (typically 0.5-5 mm), the lesion size is relatively small and the treatment can be targeted in a small region without harming the surrounding tissue. Since the 1950's, focused ultrasound surgery (FUS) has been studied as a promising means for brain surgery [12, 67, 139]. However, due to the large discrepancy between the acoustical properties of cranium and soft tissues [66], the method required removal a portion of the skull to create a window for the sound beam. In addition, the early systems for ultrasound surgery lacked a practical device to monitor the

temperature of tissue during the treatment. Consequently, FUS did not become a clinical standard.

The development of magnetic resonance imaging (MRI) techniques for temperature monitoring of tissue [41] has caused a renaissance of FUS, see reviews [110, 187, 188]. Now FUS treatment of brain can be monitored almost in real time using MRI [194]. Furthermore, experimental and numerical studies have shown the feasibility of FUS of brain through intact skull [111, 185, 186]. Due to the strong scattering of the sound from the interfaces of skull and soft tissue; and high absorption of the sound in the skull, the delivery of sufficient energy into the focus requires the use of a large hemispherical phased array [39, 40]. However, the variation in the thickness and acoustical properties of the skull necessitates the use of numerical techniques to predict the distortion of the wave field at different locations of the skull. To date, this has been done either using acoustic ray methods [160, 185] or the finite difference time domain (FDTD) method for the linear acoustic wave equation [7, 159]. A more accurate model should also take into account the elastic properties of the skull [96].

The need for accurate methods to simulate wave fields in complex biological media is not only limited to FUS of brain. Similar techniques must be used when the sound beam propagates through tissues with varying acoustical properties, for example, through the rib cage in the simulation of liver surgery [24, 25].

Although ray-based methods can approximate ultrasonic waves in relatively simple geometries and in homogeneous media, the use of full-wave methods (such as difference methods) is necessary to obtain tolerable accuracy in more complex problems. The linearized approximation to the equations of acoustic wave propagation in a fluid have been found appropriate for modeling therapeutic ultrasound fields [109]. Furthermore, typical sonication times in the FUS are relatively long and hence, in many cases, the sound fields in acoustic and elastic media can be assumed to satisfy the continuous (i.e time-harmonic) Helmholtz and Navier equations.

Finite difference methods for these equations suffer from the requirement of a dense spatial discretization and are therefore computationally rather demanding at ultrasound frequencies. Other candidates for the full-wave methods are finite element methods (FEM) and more recent improved finite element type methods. The flexible spatial discretization of finite element-based methods allows computations in very complex geometries.

The development of FEM for acoustic problems began in the 1970's. The method for unbounded Helmholtz problems was analyzed more detailed in the 1980's [9, 78]. However, standard low order finite element methods require almost as dense spatial discretization as the standard finite difference method and are therefore too costly for most ultrasound simulations. The performance of FEM can be improved by using higher order elements [115] or spectral elements [151].

Another factor affecting the accuracy of domain-based full-wave methods is the truncation of the physically unbounded problem into a problem on a bounded domain. Namely, the boundary condition on the auxiliary exterior boundary of the bounded domain should allow waves to propagate outward without numerical

reflections back into the domain.

While the standard FEM uses polynomial basis functions to approximate the wave field, a notable reduction in computational burden is possible by using basis functions which better imitate the oscillatory behavior of the wave field. This kind of approach was proposed for the infinite element method and the wave envelope method in [3, 6, 21]. In these methods, conventional polynomial finite elements are used in a relatively small domain which encloses the inhomogeneities (or sound sources). Whereas the wave field in the exterior region is approximated using wave-like functions which extend (and decay) from the boundary to infinity.

Since the invention of infinite elements, the incorporation of a priori information into the approximating subspace of the numerical method has been considered as one of the most promising approaches for reducing the complexity of wave simulations. The intensive study of methods of this type has produced variety of new and interesting methods. The extension of the finite element method, called the partition of unity finite element method [10], has been used for the Helmholtz problem by using plane wave basis functions [134, 135, 150, 157]. Plane waves have been utilized for the discretization of the integral equation form of the Helmholtz problem in the micro-local discretization [54, 53] and boundary element method [32, 162]. A similar method has been developed for the integral equation representation of the Navier problem in [161, 163]. Finite element meshes and plane wave basis functions are also used in least-squares methods [152, 184], the discontinuous Galerkin method [64] and the ultra weak variational formulation (UWVF) [29, 30, 31].

The UWVF method has several features which make it an attractive candidate for large-scale wave simulations. First, the new variational formulation reduces the problem to element faces only. This reduces the dimension of the resulting integrals for the system matrix by one. Second, the system matrices can be computed with closed form integrals which speeds up the computations. And third, the structure of the system matrix allows to predict the conditioning of the problem at the same time as building the matrices. Of course, there are drawbacks in the UWVF. For example, the basis functions must be chosen carefully to avoid ill-conditioning. Furthermore, implementation of the method for problems in which the material properties vary within an element is difficult. However, material properties can vary between elements.

Aims and contents of this thesis

In this thesis the ultra weak variational formulation (UWVF) developed in [29, 30, 56] is implemented for the Helmholtz and Navier problems in inhomogeneous media. The derivation of the UWVF in this thesis is similar as in the original works of Cessenat and Després. However, the main focus is on the developing the UWVF feasible for practical acoustic simulations. Particularly, the stability of the method is improved and the perfectly matched layer (PML) is used with the UWVF to reduce spurious numerical reflections associated to truncation of the unbounded Helmholtz problems. A particular emphasis has been on the development of the

UWVF method for the modeling of ultrasound fields in biological tissues.

Some of the material of this thesis has been published previously in [105, 107, 108] or is in peer-review [106]. Furthermore, the acoustic UWVF method has been used as a part of treatment optimization simulations for ultrasound therapy in [143, 144, 145, 146].

The thesis is organized as follows. Chapter 2 outlines the physical background of mechanical waves. Starting from linearized conservation laws, the chapter reviews the basic theory of acoustic and elastic wave propagation.

Chapter 3 is dedicated to numerical methods for wave problems. The discussion begins with a review of methods for the truncation of unbounded wave problems. The main emphasis is on methods which are used later in this thesis, especially on the perfectly matched layer. The standard numerical tools for Helmholtz and Navier problems are outlined next. These include the finite difference, finite element and boundary element methods. Chapter 3 is concluded by a brief review on improved computational methods for the wave problems and a summary on alternative methods to truncate the unbounded problems.

The ultra weak variational formulation is discussed in Chapter 4. Following the ideas of [29], the UWVF for Helmholtz problem in inhomogeneous media is derived and discretized. Then the modifications in the UWVF arising from the use of the PML are introduced. Finally, the UWVF is extended to elastic wave problems characterized by the Navier equation.

In Chapter 5 a stabilization method for the UWVF via a suitable choice of basis functions is proposed. This scheme is studied for the 2D Helmholtz and Navier problems. In both cases, the UWVF method is analyzed for simple test problems for which closed form solutions can be derived. Computational studies for 3D Helmholtz-UWVF using the PML are presented in Chapter 6. Due to the larger size of the 3D problems, a parallelized UWVF scheme is introduced.

Finally, two practical applications for the Helmholtz-UWVF method in ultrasonics modeling are introduced in Chapters 7 and 8. In Chapter 7 the UWVF scheme is used to model anomalies in ultrasound fields caused by devices used for measuring the fields. Simulations for needle and membrane hydrophones are done in the frequency range 0.5-2.0 MHz. In Chapter 8, UWVF simulations are compared with experimental measurements in the case of transmission of ultrasound waves through layered plastic plates. Similar problems to this are of great importance in the modeling of ultrasound surgery of brain. The results of this thesis are concluded in Chapter 9.

Chapter II

Acoustic field equations

In the literature on mechanical wave propagation, two wave types are distinguished depending on the properties of the underlying propagation medium. Traditionally, waves in fluids are called *acoustic waves* whereas waves in solids are termed *elastic waves*. Since the distinction between fluids and solids is based on idealizations and is not sharp for real physical materials, the categorization between acoustic and elastic waves is also artificial. For example, the modeling of acoustic waves includes the assumption that fluids can not bear shear forces. However, this is not true in the case of viscous fluids in which the behavior of the wave field has characteristics typical of fields in solids. Therefore, formulas derived for ideal fluids omit phenomena that are essential for the modeling of real physical fluids. Despite their limitations, the equations for ideal fluids can be used to model many real fluids if the approximations buried in the equations are recognized and empirical information is included in the model.

The separation into elastic and acoustic waves, however, gives a good starting point for a general discussion of mechanical waves. Hence, this approach has been adopted in the following review of mechanical wave phenomena. This chapter is aimed at giving a short introduction to the physical theory of elastic and acoustic wave propagation. Theories related to these wide topics are discussed to an extent that is sufficient for undertanding the rest of this thesis. For a more detailed analyses on elasticity and elastic waves, see for example [1, 8, 79, 137]. The theory of fluid dynamics and acoustics is discussed in [13, 65, 153, 166].

This chapter begins with an introduction to conservation laws and their linear approximation. This is needed in the derivation of the linear wave equation. The wave equation for ideal elastic material is derived next, followed by the formulation of the acoustic wave equation. Since the numerical methods studied in this thesis are developed for time-harmonic wave fields, the main focus is on time-harmonic forms of the wave equations. Furthermore, elastic and acoustic wave equations are compared briefly. The chapter is concluded by a discussion of acoustic and elastic boundary conditions; and elastic surface waves.

2.1 Linearized conservation laws

The linear wave equations for elastic and fluid media can be derived starting from two conservation laws. First, the so-called *equation of continuity* states that the time-rate of mass moving into a volume through its surface must be equal to the mass increase of the volume. Since this integral law must hold for an arbitrary volume it can be written in the differential form as

$$\frac{\partial \rho}{\partial t} + \nabla \cdot (\rho V) = 0, \tag{2.1}$$

where ρ is the mass density and V is the particle velocity.

Second, *conservation of momentum* is a direct consequence from Newton's second law. The acceleration of an arbitrary volume can be expressed as the material derivative $\frac{\partial V}{\partial t} + (V \cdot \nabla)V$ which must be equal to the forces acting on the volume. There gradient of the vector $V = (V_x, V_y, V_z)^\top$ is defined in component form as $\nabla V = (\frac{\partial}{\partial x}, \frac{\partial}{\partial y}, \frac{\partial}{\partial z})^\top (V_x, V_y, V_z)$ where transpose is denoted by $\top$.

Moreover, the forces can be divided into body forces and surface tractions. This yields

$$\rho \left(\frac{\partial V}{\partial t} + (V \cdot \nabla)V \right) = \rho F + \nabla \cdot \tau, \tag{2.2}$$

where τ is the stress tensor and F is the body force. The divergence is applied separately to each column of the stress tensor τ. Hence the divergence of the tensor is a vector [164].

Assuming that changes from the steady state values $V_0 = 0$ and ρ are relatively small, it is possible to write linear approximations for the particle velocity and density as $V_0 + V(r,t)$, $\rho + \delta(r,t)$, respectively. Here $r = (x, y, z)$ is the spatial variable and t is time. Then, in the absence of body forces F, the linearized conservation laws reduce to

$$\frac{\partial \delta}{\partial t} = -\rho \nabla \cdot V, \tag{2.3}$$

$$\rho \frac{\partial V}{\partial t} = \nabla \cdot \tau. \tag{2.4}$$

2.2 Elastic wave equation

Consider an ideal elastic body which undergoes deformation so that the position vector r is after deformation given by r'. The displacement vector is then defined to be $U = r' - r$. If the deformation is small, the linearized strain tensor is given by [137]

$$\epsilon = \frac{1}{2} \left[(\nabla U) + (\nabla U)^\top \right]. \tag{2.5}$$

In addition to appropriate conservation laws, for the derivation of the wave equation, a relation between deformation and stresses is needed. The constitutive

equation defines the strain of the medium under specified forces. Since the strain ϵ and the stress τ are second order tensors, the coupling tensor consists of 81 constants. For an isotropic media, however, the relation between the stress and strain can be postulated as Hooke's law which has only two independent coefficients Λ and μ. The law is typically written in the form

$$\tau = \Lambda \mathrm{tr}(\epsilon) I + 2\mu\epsilon, \tag{2.6}$$

where $\mathrm{tr}(\epsilon) = \nabla \cdot U$ is the trace of the tensor ϵ and I is the unit tensor. The parameters Λ and μ are known as the Lamé coefficients and for an isotropic elastic medium, they can be expressed by means of the Poisson ratio ν and Young's modulus E as follows

$$\mu = \frac{E}{2(1+\nu)}, \qquad \Lambda = \frac{E\nu}{(1+\nu)(1-2\nu)}. \tag{2.7}$$

Using the definition of strain (2.5), Hooke's law can be rewritten as

$$\tau = \Lambda(\nabla \cdot U) I + \mu \left[(\nabla U) + (\nabla U)^\top \right]. \tag{2.8}$$

Assuming that the material parameters are spatially varying so that $\Lambda = \Lambda(r)$ and $\mu = \mu(r)$, a general linear elastic wave equation is obtained by substituting Hooke's law (2.8) to the linear conservation of momentum equation (2.4) (see e.g. [147]). Instead, if it is assumed that the elastic material occupies a domain Ω in which the Lamé coefficients Λ and μ are constants, the differentiation in $\nabla \cdot \tau$ does not affect them. In such a case the substitution gives [79]

$$\rho \frac{\partial^2 U}{\partial t^2} = \mu \Delta U + (\Lambda + \mu) \nabla(\nabla \cdot U) \quad \text{in } \Omega. \tag{2.9}$$

The time-harmonic form of the Navier equation (2.9) for the spatial part of the displacement vector $U(r,t) = u(r)e^{-i\omega t}$ is

$$\mu \Delta u + (\Lambda + \mu) \nabla(\nabla \cdot u) + \omega^2 \rho u = 0 \quad \text{in } \Omega, \tag{2.10}$$

where $\omega = 2\pi f$ is the angular frequency of the field and f is the frequency. Obviously, the displacement $U(r,t)$ in this case is complex valued and the observed physical wave at time t is the real part of U, i.e. $\Re(u(r)e^{-i\omega t})$.

In order to model dissipation in the elastic medium one can allow E to be complex valued and in particular $E = E' - iE''$, $(E',\ E'' \geq 0)$ where E' is the standard Young's modulus and E'' is often called the loss modulus. It is assumed that for a constant Young's modulus E', the loss modulus is a non-negative constant.

In an unbounded homogeneous medium, the solution of the elastic wave equation (2.10) can be decomposed into two orthogonal components. Namely, rewrite the displacement field as a sum $u = u_P + u_S$ which satisfy $\nabla \times u_P = 0$ and $\nabla \cdot u_S = 0$. Then one can easily show that u_P and u_S are both solutions of the Helmholtz equations

$$\Delta u_P + \kappa_P^2 u_P = 0 \quad \text{and} \quad \Delta u_S + \kappa_S^2 u_S = 0, \quad \text{in } \Omega. \tag{2.11}$$

The waves u_P and u_S are called P-wave (or dilatational wave) and S- wave (or shear wave). They have with different wave numbers $k_P = \omega/c_P$ and $k_S = \omega/c_S$ with different wave speeds

$$c_P = \sqrt{\frac{\Lambda + 2\mu}{\rho}} \quad \text{and} \quad c_S = \sqrt{\frac{\mu}{\rho}}. \tag{2.12}$$

2.3 Acoustic wave equation

For a viscous fluid the stress tensor can be written as [13]

$$\tau = -PI + 2\mu_f \left\{ \frac{1}{2}[(\nabla V) + (\nabla V)^\top] - \frac{1}{3}(\nabla \cdot V)I \right\}, \tag{2.13}$$

where P is the acoustic pressure and μ_f is the viscosity.

Substitution of (2.13) to the momentum equation (2.4) gives

$$\rho \frac{\partial V}{\partial t} = -\nabla P + \mu_f \left[\Delta V + \frac{1}{3}\nabla(\nabla \cdot V) \right]. \tag{2.14}$$

Assuming first an ideal inviscid fluid $\mu_f = 0$ (the effect of the viscosity will be discussed later), the equation (2.14) reduces to

$$\frac{\partial V}{\partial t} = -\frac{1}{\rho}\nabla P. \tag{2.15}$$

To be able to use the continuity equation (2.1), a relation between the acoustic pressure P and density δ must be defined. For the linear adiabatic case, the state equation

$$P = P(\delta, s), \tag{2.16}$$

where s is entropy, can be obtained as the first term of the Taylor series expansion of (2.16) around the equilibrium state (ρ, s_0) as [85]

$$P \approx \left(\frac{\partial P}{\partial \rho} \right)_s \delta = c^2 \delta, \tag{2.17}$$

where c is the speed of sound. With relation (2.17), the linearized continuity equation (2.3) can be reformulated as

$$\frac{\partial P}{\partial t} = -\rho c^2 \nabla \cdot V. \tag{2.18}$$

Now by taking the divergence of (2.15) and by differentiating (2.18) with respect to time t one obtains

$$\nabla \cdot \frac{\partial V}{\partial t} = -\nabla \cdot \left(\frac{1}{\rho}\nabla P \right) \quad \text{and} \quad \frac{1}{\rho c^2}\frac{\partial^2 P}{\partial t^2} = -\nabla \cdot \frac{\partial V}{\partial t}.$$

Therefore, linear acoustic wave propagation and scattering in an ideal quiescent heterogeneous medium is characterized by the wave equation

$$\nabla \cdot \left(\frac{1}{\rho} \nabla P \right) - \frac{1}{\rho c^2} \frac{\partial^2 P}{\partial t^2} = 0. \tag{2.19}$$

The restriction to ideal fluids resulted in the wave equation (2.19) for the acoustic pressure. By taking into account the viscosity μ_f, there is a straightforward analogy between the elastic and acoustic wave equations. In particular, as in the case of elastic solids, the wave equation for displacement includes two orthogonal components which propagate with different wave speeds. For most fluids, the S-wave component u_S has negligible effect and the wave field can be modeled using a pressure wave equation with certain additions. These modifications are discussed next.

Consider a time-harmonic wave field for which the acoustic particle velocity V, pressure P and density fluctuation δ can be written as

$$\begin{aligned} V(r,t) &= -i\omega u(r) e^{-i\omega t}, & (2.20)\\ P(r,t) &= p(r) e^{-i\omega t}, & (2.21)\\ \delta(r,t) &= \delta_\omega(r) e^{-i\omega t}. & (2.22) \end{aligned}$$

Moreover, assume that the material parameters c, ρ and μ_f are constants. With these assumptions the linearized continuity (2.3) and momentum (2.14) are

$$\begin{aligned} p &= -\rho c^2 \nabla \cdot u, & (2.23)\\ \rho\omega^2 u &= \nabla p + i\omega\mu_f \left[\Delta u + \frac{1}{3} \nabla(\nabla \cdot u) \right]. & (2.24) \end{aligned}$$

By taking the gradient of the first, substituting $\nabla p = -\rho c^2 \nabla(\nabla \cdot u)$ into the second gives

$$-i\omega\mu_f \Delta u + \left(\rho c^2 - \frac{1}{3} i\omega\mu_f \right) \nabla(\nabla \cdot u) + \rho\omega^2 u = 0. \tag{2.25}$$

This equation is identical with (2.10) if one chooses the Lamé coefficients as

$$\mu = -i\omega\mu_f \quad \text{and} \quad \Lambda = \rho c^2 + \frac{2}{3} i\omega\mu_f. \tag{2.26}$$

Analogously with the elastic medium, the displacement field in a homogeneous viscous fluid can be decomposed into P- and S-waves $u = u_P + u_S$ which satisfy the Helmholtz equations (2.11). Obviously, the substitution of (2.26) to (2.12) leads to complex valued wave speeds and hence complex wave numbers in the Helmholtz equations (2.11). However, it is possible to assume that the wave speeds c_P and c_S are real and the wave numbers for P- and S-waves are written in the complex form as

$$\kappa_P = \frac{\omega}{c_P} + i\alpha_P \quad \text{and} \quad \kappa_S = \frac{\omega}{c_S} + i\alpha_S,$$

where α_P and α_S are the real valued absorption coefficients. Via the substitutions $u_P = ae^{i\kappa_P d\cdot r}$ and $u_P = be^{i\kappa_S d\cdot r}$ where $|a| = |b| = |d| = 1$ and $a \cdot b = 0$ one clearly sees that P- and S-waves decay by factors $e^{-\alpha_P d\cdot r}$ and $e^{-\alpha_S d\cdot r}$, respectively.

Using this representation, the wave speeds and absorption coefficients for the viscous fluid are

$$\begin{aligned} c_P &= c\sqrt{2}\left[\frac{1+(\omega t_R)^2}{\sqrt{1+(\omega t_R)^2}+1}\right]^{1/2}, \\ \alpha_P &= \frac{\omega}{c}\frac{1}{\sqrt{2}}\left[\frac{\sqrt{1+(\omega t_R)^2}-1}{1+(\omega t_R)^2}\right]^{1/2}, \\ c_S &= \alpha_S = \sqrt{\frac{\omega\rho}{2\mu_f}}, \end{aligned}$$

where

$$t_R = \frac{4}{3}\frac{\mu_f}{\rho c^2}.$$

Note that in this form, the P-wave phase speed c_P varies with the frequency and the wave is *dispersive*. However, if $\omega t_R << 1$, the wave speed c_P can be approximated as $c_P \approx c$.

Shear waves in fluids are called *viscous waves*. In fluids with low viscosity, viscous waves are damped in a short distance and have therefore a negligible effect on the acoustic wave field. By ignoring S-waves the resulting field $u = u_P$ is irrotational (i.e. $\nabla \times u = 0$).

The viscous effects are not adequate to characterize the absorption of sound in real physical materials. The so-called classical absorption model takes into account also the effect of heat conduction [22]. However, the complete model should include, for example, various molecular level relaxation mechanisms and the scattering of sound from the internal structures of the material. Consequently, the absorption coefficient for most materials at ultrasound frequencies must be defined by experimental measurements.

Next turn back to equation (2.25) and assume that $u = u_P$ from which it follows that $\nabla \times u = 0$. Using the vector identity $\Delta u = -\nabla(\nabla \cdot u) + \nabla \times \nabla \times u$ and the time-harmonic continuity equation (2.23), the equation for the P-waves in a homogeneous medium reduces to the Helmholtz equation for the acoustic pressure

$$\Delta p + \kappa^2 p = 0, \tag{2.27}$$

where $\kappa = \kappa_P$.

Accordingly, the wave equation for spatially varying density $\rho = \rho(r)$ and speed of sound $c = c(r)$ can be formulated in the time-harmonic case as

$$\nabla \cdot \left(\frac{1}{\rho}\nabla p\right) + \frac{\kappa^2}{\rho} p = 0, \tag{2.28}$$

where $\kappa = \omega/c(r) + i\alpha(r)$.

2.4 Transmission conditions

Many relevant wave problems deal with waves propagating in domains consisting of piecewise homogeneous materials. In such a case, the wave equations (2.10) or (2.27) (depending on whether the material is elastic or fluid) can be used in each homogeneous subdomain. However, at the material interfaces, a suitable transmission conditions must be defined.

Suppose now that the region of interest Ω consist of two subdomains Ω_1 and Ω_2 occupied by two different elastic materials. The Lamé coefficients for Ω_1 and Ω_2 are (Λ_1, μ_1) and (Λ_2, μ_2), respectively. Furthermore, assume that the elastic wave fields in both domains satisfy the time-harmonic Navier equation (2.10).

To couple the two wave fields across the common edge $\Sigma_{1,2} = \overline{\Omega}_1 \cap \overline{\Omega}_2$, physically appropriate transmission conditions must be defined on $\Sigma_{1,2}$. Such conditions can be developed by considering an infinitesimal volume of the body Ω_1 that is located near the interface $\Sigma_{1,2}$. The oscillation of this body causes a force on the adjacent particles in the domain Ω_2. Let the interface $\Sigma_{1,2}$ have a normal n_1 pointing outward from Ω_1. The force that exerts from the body in Ω_1 and that acts on the interface can be written using the traction operator $T^{(n_1)}$ as [8]

$$\tau \cdot n_1 = T^{(n_1)}(u_1) = 2\mu_1 \frac{\partial u_1}{\partial n_1} + \Lambda_1 n_1 \nabla \cdot u_1 + \mu_1 n_1 \times \nabla \times u_1, \tag{2.29}$$

where $u_1 = u|_{\Omega_1}$. The operator T maps local displacements to local tractions on the boundary $\Sigma_{1,2}$.

A similar traction operator (2.29) can be defined on the same part of the interface for forces from Ω_2. Hence, on the interface $\Sigma_{1,2}$, the continuity of the displacement and the stress leads to transmission conditions

$$\left.\begin{array}{rcl} u_1 & = & u_2 \\ T^{(n_1)}(u_1) & = & -T^{(n_2)}(u_2) \end{array}\right\} \quad \text{on } \Sigma_{1,2}, \tag{2.30}$$

where $n_2 = -n_1$, T is given by (2.29) and the Lamé coefficients in Ω_ℓ are used to evaluate $T^{(n_\ell)}(u_\ell)$, $\ell = 1, 2$.

Similarly, consider that the domains Ω_1 and Ω_2 are occupied by different but homogeneous acoustic fluids. Hence the wave fields $p_1 = p|_{\Omega_1}$ and $p_2 = p|_{\Omega_2}$ satisfy the Helmholtz equation (2.27) with the wave numbers κ_1 and κ_2, respectively. Again, the stress and displacement are assumed to be continuous across the interface $\Sigma_{1,2}$. It is assumed next that in the case of the acoustic fluid, the effect of viscosity is negligible. Then, the continuity of stress follows from the continuity of the acoustic pressure. Moreover, since the inviscid acoustic fluid is incapable of bearing shear forces, the continuity of displacement follows if the normal particle displacements $u \cdot n = \frac{1}{\rho} \nabla p \cdot n$, see Eq. (2.15), are equal on both sides of the interface. Therefore, the transmission conditions for the acoustic material are

$$\left.\begin{array}{rcl} p_1 & = & p_2 \\ \dfrac{1}{\rho_1} \dfrac{\partial p_1}{\partial n_1} & = & -\dfrac{1}{\rho_2} \dfrac{\partial p_2}{\partial n_2} \end{array}\right\} \quad \text{on } \Sigma_{1,2}. \tag{2.31}$$

Although not further analyzed in this thesis, coupled fluid-solid boundary conditions are formulated next. Assume that the field in the domain Ω_1 is characterized by the elastic wave equation (2.10) and the field in the domain Ω_2 satisfies the Helmholtz equation (2.27). Analogously with previous formulations, the transmission conditions on the fluid-solid interface $\Sigma_{1,2}$ can be written as

$$\left.\begin{aligned} T^{(n_1)}(u_1)\cdot n_1 &= -p_2 \\ \omega^2 u_1 \cdot n_1 &= -\frac{1}{\rho_2}\frac{\partial p_2}{\partial n_2} \end{aligned}\right\} \quad \text{on } \Sigma_{1,2}. \tag{2.32}$$

Special case: scattering problems

A formulation of the transmission problem (whether elastic, acoustic or coupled) using the transmission conditions (2.30)-(2.32) includes the assumption that the fields in both subdomains are of practical interest and they interact with each other. However, in some applications the field in one subdomain does not alter the field in the other subdomain. Such a case occurs, for example, when the material in one subdomain is acoustically impenetrable. Obviously this must change the boundary conditions.

Two types of impenetrable boundary conditions can be distinguished. Assume first that the domain Ω_2 is vacuum and therefore has no resistance to pressure or traction from domain Ω_1. This results in the free-surface (or cavity or sound-soft) boundary condition on $\Sigma_{1,2}$ which for elastic and acoustic fields in Ω_1 are

$$T^{(n_1)}(u_1) = 0 \quad \text{and} \quad p_1 = 0,$$

respectively. Alternatively, if the material in the domain Ω_2 is perfectly rigid, the particles on $\Sigma_{1,2}$ in acoustic case have vanishing normal velocity component. In terms of pressure this can be written as

$$\frac{\partial p_1}{\partial n_1} = 0.$$

For the elastic problem, the rigid boundary condition means vanishing displacement so that

$$u_1 = 0 \quad \text{on } \Sigma_{1,2}.$$

A useful consequence of the impenetrable boundary conditions is that by decomposing the fields p_1 and u_1 into the incident $(p_1^{\text{in}}, u_1^{\text{in}})$ and scattered parts $(p_1^{\text{sc}}, u_1^{\text{sc}})$ as $p_1 = p_1^{\text{in}} + p_1^{\text{sc}}$ and $u_1 = u_1^{\text{in}} + u_1^{\text{sc}}$, the problems can be formulated for the scattered parts of the fields only. For example, in the case of the classical acoustic *scattering problem* from a perfectly rigid obstacle, the vanishing normal derivative of the total pressure p_1 follows if

$$\frac{\partial p_1^{\text{sc}}}{\partial n_1} = -\frac{\partial p_1^{\text{in}}}{\partial n_1}.$$

Since the known incident field p_1^{in} can be assumed to satisfy the Helmholtz equation (2.27), one needs to solve the scattered part of the field p_1^{sc} only. Similar formulation can be used to define scattering problems for elastic waves from impenetrable obstacles.

2.5 Sommerfeld radiation condition

To guarantee a unique solution for wave problems on unbounded domains, it is necessary to define a condition that characterizes the behavior of the fields at infinity. Hence, consider a wave source at the origin and let R be the radial distance from origin to the observation point. The wave field is said to be outgoing if it propagates in the direction of the increasing distance R. In the case of the Helmholtz problem, the outgoing wave field satisfies the Sommerfeld radiation condition

$$\lim_{R\to\infty} R^{(d-1)/2}\left(\frac{\partial p}{\partial R} - i\kappa p\right) = 0, \tag{2.33}$$

where d is the dimension of the problem [166].

Recalling that the elastic wave field in an infinite homogeneous medium consists of two orthogonal components $u = u_P + u_S$, the radiation condition can be defined independently for both terms as [1]

$$\begin{aligned}\lim_{R\to\infty} R^{(d-1)/2}\left(\frac{\partial u_P}{\partial R} - i\kappa_P u_P\right) = 0 \quad \text{and} \\ \lim_{R\to\infty} R^{(d-1)/2}\left(\frac{\partial u_S}{\partial R} - i\kappa_S u_S\right) = 0.\end{aligned} \tag{2.34}$$

2.6 Surface and edge waves

The boundary conditions discussed in Section 2.4 give rise to additional wave forms beyond those observed in an infinite elastic (or viscous) medium. While in an unbounded homogeneous medium the P- and S-waves propagate independently, they interact on material interfaces. Consequently, near material boundaries, edge or surface waves can be generated. These waves travel along the boundary but decay rapidly into the medium as the distance from the interface increases. The simplest example of such waves are *Rayleigh surface waves* which can be generated on the free surface (i.e. where $T^{(n)}(u) = 0$) whereas edge waves on the interface of two elastic material are called the *Stoneley waves*. In addition to surface and edge waves, the P- and S-waves can couple in waveguides. Those waves are called *Lamb waves*. Coupled waves in plates (i.e. waveguides) on an elastic half space are named *Love waves*. Since the Rayleigh waves are used as a test problem later in this thesis, they are discussed next.

Suppose that an elastic medium occupies a 2D semi-infinite domain $y > 0$. The free-surface boundary condition $T^{(n)}(u) = 0$ on the boundary $y = 0$ allows the formation of Rayleigh waves which are assumed to propagate in the direction

of the positive x-axis. A detailed treatment of Rayleigh waves can be found, for example, in [1, 79, 137]. Only an outline is given here.

The speed of the Rayleigh wave c_R can be obtained as a solution of the equation

$$\left(\frac{c_R}{c_S}\right)^6 - 8\left(\frac{c_R}{c_S}\right)^4 + 8\left[3 - 2\left(\frac{c_S}{c_P}\right)^2\right]\left(\frac{c_R}{c_S}\right)^2 - 16\left[1 - \left(\frac{c_S}{c_P}\right)^2\right] = 0. \quad (2.35)$$

The exact solution of (2.35) is quite complicated, therefore an approximate value is commonly used. For example [8, 79] give an approximation to the wave speed as

$$c_R \approx \frac{0.87 + 1.12\nu}{1+\nu} c_S,$$

where ν is the Poisson ratio. The accuracy of this approximation is better than 0.5 % [8].

Let $\kappa_R = \omega/c_R$ denote the Rayleigh wave number computed using the above approximate wave speed. Then the x- and y-components of the displacement field $u = (u_x, u_y)^\top$ can be written as

$$\begin{aligned} u_x &= \alpha_S \left\{ e^{-\alpha_S y} - \frac{2\kappa_R^2}{\kappa_R^2 + \alpha_S^2} e^{-\alpha_P y} \right\} e^{i\kappa_R x}, \\ u_y &= i\kappa_R \left\{ e^{-\alpha_S y} - \frac{2\alpha_P \alpha_S}{\kappa_R^2 + \alpha_S^2} e^{-\alpha_P y} \right\} e^{i\kappa_R x}, \end{aligned} \quad (2.36)$$

where

$$\alpha_P = \sqrt{\kappa_R^2 - \left(\frac{\omega}{c_P}\right)^2} \quad \text{and} \quad \alpha_S = \sqrt{\kappa_R^2 - \left(\frac{\omega}{c_S}\right)^2}.$$

The Rayleigh wave (2.36) satisfies the time-harmonic Navier equation (2.10) and the displacement amplitude of the wave decays when the distance from the free-surface increases. Particularly, equation (2.36) shows clearly that the wave field decays exponentially in the y-direction but propagates non-dissipatively with the wave speed c_R in the x-direction. Furthermore, the trajectories of the particle motion in the field are ellipses whose major axes are normal to the surface.

Chapter III

Numerical approximation of wave problems

In this chapter, a review of numerical methods for the acoustic and elastic wave problems is given. Since the aim of this thesis is to study feasible methods for the modeling of therapeutic ultrasound fields, the review is not limited to numerical methods for the time-harmonic problems (2.28) and (2.10) only. Instead, other computational tools for wave fields are discussed briefly provided that they have been widely used for medical ultrasonics. Such tools are, for example, time-domain and ray methods. In addition to computational methods, the truncation of the unbounded acoustic problems is vital for the numerical approximation of the wave fields. Feasible methods for this will be also reviewed.

Numerical approximation of wave problems in heterogeneous media and in general geometries is difficult. Analytical solutions can be derived for the simplest wave problems only and the computational complexity of numerical methods increases rapidly with the wave number. Some classical methods for wave propagation problems are reviewed in [120]. In standard numerical tools, such as the finite difference (FD) and low order finite element (FE) methods, *a rule of thumb* is that approximately ten discretization points per wavelength are needed to obtain a tolerable accuracy [113]. This leads rapidly to extremely large computational tasks. Furthermore, at high wave numbers these methods suffer from *numerical pollution* [11, 71] which causes the accuracy of methods to decrease with the wave number even if the mesh density with respect to the wavelength remains unchanged.

Especially in the problems of medical ultrasonics in which the wavelength of the sound field is very short (typically 0.5-5 mm in ultrasound therapy), wave fields must be evaluated in domains whose dimensions can be hundreds of wavelengths. Previously the major interest in the development of computational methods for ultrasonics has been devoted to the ultrasound imaging which is mainly based on short sound pulses. However, the need for modeling fields generated by longer excitations (i.e. continuous-waves) has increased with developments in the ultrasound therapy [110, 187].

Traditionally, ultrasound fields are modeled using different kinds of ray approximation, see e.g. [25, 24, 61, 130]. These methods are accurate and effective

if multiple reflections do not occur and the propagation medium is rather simple. However, they become computationally demanding if the medium is strongly scattering and waves undergo complex interference phenomena.

The use of a time domain method, such as the finite difference time domain (FDTD) method [176], for time-harmonic problems [177] requires a large number of time steps (in addition to a dense spatial discretization) to reach a steady-state solution. Obviously, this also leads to a heavy computational burden [177]. Various improved time-domain methods have been proposed. For ultrasound fields these include, for example, pseudospectral [197] and k-space methods [149]. Despite the recent improvements, realistic 3D applications are still computationally extremely demanding.

To reduce the effect of numerical pollution in the finite element method, various modifications have been proposed. These include, for example, higher order methods [115] (such as spectral elements [151]) and least-squares finite elements [90, 156, 189]. Methods that incorporate *a priori* information about the solution to the approximating space (e.g. the partition of unity finite element method (PUM) [10, 135], least squares method [152], discontinuous Galerkin method [64] and the ultra weak variational formulation (UWVF) [30]) are other promising candidates for reducing the computational burden.

Many problems in acoustics are physically unbounded, this is, the sound field extends from the source to infinity. The behavior of the field at infinity is characterized by the Sommerfeld radiation condition, see Section 2.5. In many cases in order to evaluate the field numerically, the unbounded problem must be replaced with a bounded one. Furthermore, the Sommerfeld condition is approximated on the exterior boundary of the computational domain by an *absorbing boundary condition* (ABC) [73, 75] (also known as non-reflecting boundary conditions (NRBC)) or by using a damping layer called *the perfectly matched layer* (PML) [17] .

In the following section the absorbing boundary conditions and selected numerical methods for full-wave problems are discussed. First, the need for an accurate approximation for the Sommerfeld condition is a general property of most numerical methods and hence the first subsection handles this important issue. In the first section local ABCs, the elastic ABC from [84] and the perfectly matched layer method are formulated. Second, a brief outline on numerical methods for computational acoustics is given. The aim is not to give a thorough treatment of this broad topic. Rather, the goal is to summarize full-wave methods that has been widely utilized in computational acoustics, in particular the finite difference method, finite element method and boundary integral methods. Since the finite element method is a standard tool in acoustics and has been used as a reference method later in this thesis, the FEM approximation of the Helmholtz and Navier equations are discussed in more detail. This chapter is concluded with a summary of recent improvements to finite element type methods and a review of alternative methods for the truncation of the computational domain for unbounded problems.

3.1 Absorbing boundary conditions

As discussed in Section 2.5, the behavior of time-harmonic wave fields from bounded regions at infinity is characterized by the Sommerfeld radiation condition (2.33). To approximate the field in a bounded domain, the region of interest can be surrounded by an artificial boundary Γ that encloses the computational domain Ω containing the material inhomogeneities. In addition, an absorbing boundary condition must be used on Γ. An ideal ABC would allow waves to propagate through the boundary Γ without spurious numerical reflections back into the computational domain. Moreover, to be feasible, the ABC should be easy to implement in general geometries and be numerically stable.

A standard approach in time-harmonic problems for constructing an ABC is to write a Neumann type exterior boundary condition on Γ which approximates the Sommerfeld condition. Therefore one needs a *Dirichlet-to-Neumann (DtN)* operator M which is a mapping between the field p and the normal derivative $\partial p/\partial n$

$$M : p|_\Gamma \rightarrow \frac{\partial p}{\partial n}\Big|_\Gamma.$$

In a general form, using a Fourier series representation of the sound field, an exact ABC for the Helmholtz problem can be constructed as a DtN operator [121]

$$\frac{\partial p}{\partial n}(r) = Mp(r) = \sum_{j=0}^{\infty} \int_\Gamma m_j(r - r_0) p(r_o) dr_0 \quad r, r_0 \in \Gamma, \tag{3.1}$$

where $m_j(r - r_0)$ are the DtN kernels. From the computational point of view the DtN operator (3.1) has two drawbacks. First, it includes an infinite sum which, however, can be truncated to obtain tolerable accuracy [88, 81]. Nevertheless, the use of many Fourier modes can still be computationally costly. Second, the operator is non-local, this is, to compute $\frac{\partial p}{\partial n}(r)$ at a point r on Γ, one must integrate over whole boundary Γ. Obviously, it would be desirable to replace the operator M with an approximating operator M_a which would absorb waves while being spatially dependent on the solution p and its derivatives at r only. The construction of this kind of local operator for Helmholtz problem is discussed in the next section. Following that, a special type of ABC from [84] is introduced for time-harmonic elastic wave propagation.

An alternative to the approximating operator M_a is to surround the domain Ω with a computational "sponge" layer which prevents reflections from the boundary Γ. Bérenger [17] proposed such a perfectly matched layer for electromagnetic waves and it has been later extended to the Helmholtz problem [91, 169]. In Section 3.1.3, the PML for Helmholtz equation is derived using the change of variables method developed in [34] and used, for example, in [45, 46, 138]. Other alternative methods for truncating the computational domain associated with particular numerical schemes are also discussed in Section 3.3.

3.1.1 Local acoustic ABCs

Traditionally, approximations to the non-local DtN operator have been constructed using local differential operators. First order local ABCs were introduced in the late 1970's [60] and early 1980's [14, 116]. Since then various improved conditions have been proposed, see e.g. the reviews [73] and [112]. Although high order local differential operators are accurate, they are typically limited to special boundary geometries (e.g. [81]) or perfectly annihilate waves only from certain incident directions [98]. To reduce problems associated with high-order ABCs, methods that can have a high-order of accuracy without high-order derivatives have also been proposed [74]. This topic, however, is not discussed further here. Instead, the low-order boundary condition used in this study is briefly introduced next and an outline for formulating higher-order Higdon type [98] conditions is given.

The most obvious form for the local ABC follows directly from the Sommerfeld radiation condition (2.33), namely

$$\frac{\partial p}{\partial n} - i\kappa p = 0 \quad \text{on } \Gamma. \tag{3.2}$$

This is often called the zeroth order (or Sommerfeld type) absorbing boundary condition. The Sommerfeld type boundary condition is applied to waves that propagate outward from the computational domain Ω. Particularly, in scattering problems, the Sommerfeld condition is used to the scattered part of the pressure field p^{sc} only.

An advantage of the form (3.2) is its suitability for general boundary geometries since only normal derivatives are needed to compute. But the drawback is poor accuracy if the artificial boundary is close to the sound source [121]. More precisely, the reflection coefficient for (3.2) using a plane wave incidence on a planar surface is

$$R = \frac{\cos\theta - 1}{\cos\theta + 1}, \tag{3.3}$$

where θ is the incident angle of the sound field. From equation (3.3) it follows that increasing the distance of the boundary Γ to the sound source typically reduces the angle θ, causing diminishing reflections. However, if the shape of the absorbing boundary is complex (e.g. it contains corners), the incident angle θ at same parts of the boundary may remain large even if the distance from the source to Γ increases. Hence the boundary geometry affects to the accuracy of the ABC. Despite its limitations, the zeroth order ABC has been used in some numerical experiments of this study and it has also been utilized as a reference method for improved approaches.

To illustrate the higher-order ABCs, this section is ended by a discussion of the Higdon type [98] high-order ABCs for general boundary Γ having the outward normal n. These can be written for an arbitrary order N as

$$M_N p = \left(\prod_{j=1}^{N} \left(\frac{\partial}{\partial n} - i\kappa d_j \cdot n \right) \right) p = 0 \quad \text{on } \Gamma. \tag{3.4}$$

These conditions are perfectly absorbing for all waves propagating in the directions $d_j,\ j = 1, ..., N$. As a trade-off against improved accuracy, the Higdon ABC involves an N-order normal derivative which might be laborious to implement with a numerical scheme. In addition, the method requires *a priori* information of the solution for selecting the directions d_j. In practice, this may be difficult to obtain.

Due to difficulties with high-order local ABCs on general geometries and wave types, the numerical experiments of this study are computed either with the zeroth order ABC (3.2) or with the perfectly matched layer discussed in Section 3.1.3.

3.1.2 Halpern's elastic ABC

In this section an absorbing boundary condition for the 2D Navier equation is briefly outlined. As in the case of the Helmholtz equation, the unbounded elastic wave problem is truncated with an artificial boundary Γ and the exact absorbing boundary condition can be defined by a non-local operator [82]. Also analogously to the previous section, local differential operators are commonly used to reduce spurious numerical reflections. Since the aim is to use the elastic ABC with the ultra weak variational formulation introduced later in this thesis, the special type ABC of [84] has been chosen.

Now suppose that all the coefficients in the Navier equation are constant near the absorbing boundary. Furthermore, consider a time-harmonic elastic plane wave moving in a direction d with $|d| = 1$. As shown in Section 2.2, the plane wave in the homogeneous medium can be split into two components

$$u = a_1 d \exp(i\kappa_P d \cdot r) + a_2 d^{\perp} \exp(i\kappa_S d \cdot r),$$

where the wave numbers $\kappa_P = \omega/c_P$ and $\kappa_S = \omega/c_S$ are obtained using the wave speeds of (2.12), a_1 and a_2 are constants and $d \cdot d^{\perp} = 0$. The first component denoted $u_P = a_1 d \exp(i\kappa_P d \cdot r)$ has the property $\nabla \times u_P = 0$ and is the P-wave solution of the Navier equation. The second component of the plane wave $u_S = a_2 d^{\perp} \exp(i\kappa_S d \cdot r)$ is the S-wave. In this case $\nabla \cdot u_S = 0$. Thus it can be clearly seen that the two components of the wave travel at different velocities and with different wave numbers.

Now the absorbing boundary condition can be developed. First consider a simplified situation in which the domain Ω is a half space $\Omega = \{(x, y), x < 0\}$ and the boundary Γ is the line $x = 0$. A time-harmonic elastic plane wave $u = (u_x, u_y)^{\top}$, traveling at normal incidence to the boundary Γ (i.e. with $d = (1, 0)^{\top}$) is perfectly absorbed if

$$\frac{\partial u_x}{\partial x} - i\kappa_P u_x = 0, \tag{3.5}$$

$$\frac{\partial u_y}{\partial x} - i\kappa_S u_y = 0, \tag{3.6}$$

since in this case $u_P = (u_x, 0)^{\top}$ and $u_S = (0, u_y)^{\top}$. The boundary conditions (3.5) and (3.6) are similar to the zeroth order absorbing boundary conditions that were

developed for the pressure waves in the previous section. Furthermore, ABCs of this type have been used also for elastic waves, see e.g. [99] and [172].

The absorbing properties of the boundary conditions (3.5) and (3.6) are conserved when they are rewritten as

$$\frac{\partial u_x}{\partial x} + \frac{c_P^2 - 2c_S^2}{c_P^2}\frac{\partial u_y}{\partial y} - i\kappa_P u_x = 0, \tag{3.7}$$

$$\frac{\partial u_y}{\partial x} + \frac{\partial u_x}{\partial y} - i\kappa_S u_y = 0. \tag{3.8}$$

These forms are particularly interesting since they allow to relate the boundary conditions to the traction operator (2.29) and the displacement vector u.

According to the definition of the boundary Γ the outward normal in this simplified example is $n = (1,0)^\top$. It follows that the components of the traction operator $T^{((1,0)^\top)}(u) = (T_x, T_y)^\top$ are given by

$$T_x = \rho c_P^2 \frac{\partial u_x}{\partial x} + \rho(c_P^2 - 2c_S^2)\frac{\partial u_y}{\partial y}, \tag{3.9}$$

$$T_y = \rho c_S^2 \left(\frac{\partial u_y}{\partial x} + \frac{\partial u_x}{\partial y} \right). \tag{3.10}$$

Combining equations (3.7)-(3.10) one can formulate the absorbing boundary condition for this case as

$$T^{((1,0)^\top)}(u) - i\sigma u = 0, \tag{3.11}$$

where

$$\sigma = \begin{pmatrix} \omega\rho c_P & 0 \\ 0 & \omega\rho c_S \end{pmatrix}.$$

Correspondingly, the absorbing boundary condition for a general boundary Γ with normal n can be derived. Following the derivation above it follows that

$$T^{(n)}(u) - i\sigma u = 0, \tag{3.12}$$

where

$$\sigma = \omega\rho(c_P n \otimes n + c_S s \otimes s), \tag{3.13}$$

and where s is the tangential vector to the boundary, and $\otimes$ denotes the outer product so that $n \otimes n = nn^\top$.

3.1.3 Perfectly matched layer

Although local absorbing boundary conditions of Section 3.1.1 are effective in many applications, they may either lack sufficient accuracy or, if high order ABCs are used, be difficult to implement in practice. Therefore, Bérenger proposed a virtual damping layer (i.e. the perfectly matched layer (PML)) which surrounds the computational domain Ω and efficiently absorbs waves from Ω. Bérenger's scheme was

first developed for Maxwell's equations but has been later extended to acoustics [91, 169]. One way to develop the PML is to add a *complex stretching* function to the spatial variables (x, y, z) [34, 45, 46]. The PML for the Helmholtz problem in inhomogeneous media using the complex stretching method is formulated next.

Consider the inhomogeneous form of the Helmholtz equation (2.28)

$$\nabla \cdot \left(\frac{1}{\rho}\nabla p\right) + \frac{\kappa^2}{\rho} p = f_s, \tag{3.14}$$

where f_s is a source term. The source term f_s is included to the equation since the numerical analysis of the PML in Chapter 6 is conducted using point sources. In order to utilize the change of variables scheme, a complex stretching for the vector r containing the spatial variables $r = (x, y, z)$ is defined as

$$x' = \begin{cases} x + \frac{i}{\kappa}\int_{x_0}^{x} \sigma_{0,x}(|x| - x_0)^n dx, & |x| \geq x_0, \\ x, & |x| < x_0, \end{cases} \tag{3.15}$$

$$y' = \begin{cases} y + \frac{i}{\kappa}\int_{y_0}^{y} \sigma_{0,y}(|y| - y_0)^n dy, & |y| \geq y_0, \\ y, & |y| < y_0, \end{cases} \tag{3.16}$$

$$z' = \begin{cases} z + \frac{i}{\kappa}\int_{z_0}^{z} \sigma_{0,z}(|z| - z_0)^n dz, & |z| \geq z_0, \\ z, & |z| < z_0, \end{cases} \tag{3.17}$$

where $\sigma_{0,\xi}$, $\xi = x, y, z$ are constants. In addition, one can define a vector of stretched spatial variables as $r' = (x', y', z')$.

The notation can be simplified by defining a function $\sigma_\xi(\xi)$ as

$$\sigma_\xi(\xi) = \sigma_{0,\xi}(|\xi| - \xi_0)^n, \qquad \xi = x, y, z, \tag{3.18}$$

where $\sigma_{0,\xi}$ is a constant and n is an integer. Moreover, for the following discussion it is useful to define

$$d_x(x) = \begin{cases} 1 + \frac{i}{\kappa}\sigma_x(x), & |x| \geq x_0, \\ 1, & |x| < x_0, \end{cases} \tag{3.19}$$

$$d_y(y) = \begin{cases} 1 + \frac{i}{\kappa}\sigma_y(y), & |y| \geq y_0, \\ 1, & |y| < y_0, \end{cases} \tag{3.20}$$

$$d_z(z) = \begin{cases} 1 + \frac{i}{\kappa}\sigma_z(z), & |z| \geq z_0, \\ 1, & |z| < z_0. \end{cases} \tag{3.21}$$

Now observe that the derivative of the stretched variable x' is

$$\frac{\partial x'}{\partial x} = d_x(x) \tag{3.22}$$

with similar expressions for $\frac{\partial y'}{\partial y}$ and $\frac{\partial z'}{\partial z}$. This allows a straightforward substitution

$$\frac{\partial}{\partial x} \to \frac{\partial}{\partial x'} = \frac{1}{d_x}\frac{\partial}{\partial x}. \tag{3.23}$$

To simplify notation, the explicit spatial dependence of d_x, d_y and d_x has been omitted from here on. The Helmholtz equation with stretched variables can be rewritten as

$$\frac{1}{d_x}\frac{\partial}{\partial x}\left(\frac{1}{d_x\rho}\frac{\partial p}{\partial x}\right) + \frac{1}{d_y}\frac{\partial}{\partial y}\left(\frac{1}{d_y\rho}\frac{\partial p}{\partial y}\right) + \frac{1}{d_z}\frac{\partial}{\partial z}\left(\frac{1}{d_z\rho}\frac{\partial p}{\partial z}\right) + \frac{\kappa^2}{\rho}p = f_s. \tag{3.24}$$

In a more compact form Equation (3.24) is

$$\nabla \cdot \left(\frac{1}{\rho}A\nabla\right) p + \frac{\kappa^2\eta^2}{\rho}p = f_s\eta^2, \tag{3.25}$$

where $\eta^2 = d_x d_y d_z$ and

$$A = \operatorname{diag}\left(\frac{d_y d_z}{d_x}, \frac{d_x d_z}{d_y}, \frac{d_x d_y}{d_z}\right). \tag{3.26}$$

It is obvious that the standard inhomogeneous Helmholtz equation (2.28) is obtained from (3.25) by choosing $\eta = 1$ and $A = I$ where I is the identity matrix. Or, in other words, Equation (2.28) follows if one chooses $x' = x$, $y' = y$ and $z' = z$.

3.2 Review of numerical methods for time-harmonic waves

Three commonly used classes of methods for time-harmonic waves are finite difference methods (FDM), finite element methods (FEM) and boundary integral methods (also known as the boundary element methods) (BEM). This section discusses the feasibility of these methods for the Helmholtz problem. In some cases, however, the extension of the method to the elastic wave problems is also discussed. Note that in general, the numerical approximation of elastic waves is more complicated since they consist of two components. In particular, the density of the spatial discretization is commonly dependent on the wavelength of the S-waves which is typically less than a half of the wavelength of the P-wave.

3.2.1 Finite difference methods

In the finite difference method, the computational domain is covered by a set of uniformly spaced discretization points. Then, the second derivative arising in the Laplace operator Δ is approximated using the standard one dimensional pointwise FDM as

$$\frac{\partial^2 p}{\partial x^2}(x) = \frac{p(x+h) - 2p(x) + p(x-h)}{h^2} + \mathcal{O}(h^2) = D_{xx}p + \mathcal{O}(h^2),$$

where h is the grid size and $\mathcal{O}(h^2)$ represents terms that are higher order than h^2. Correspondingly, the FDM approximation for the 3D Helmholtz equation in an homogeneous medium (2.27) is

$$(D_{xx} + D_{yy} + D_{zz} + \kappa^2)p(x, y, z) = 0. \tag{3.27}$$

This scheme is second order accurate for a smooth p but lacks sufficient accuracy (or requires extremely dense discretization) if the field has sharp gradients. In particular, difficulties may arise if the propagation medium has strong inhomogeneities. In such a case, the derivatives of material parameters in the equation (2.28) must be included in the difference operator. Obviously, if the material interfaces are sharp and strong, the approximation of derivatives using a coarse grid becomes unreliable. On the other hand, to be able to capture oscillations of the wave field, the rule of thumb $\lambda/h \approx 10$ must hold. Due to the numerical pollution, the ratio λ/h must grow with the wave number in order to maintain a desired accuracy. These factors indicate that fine grids are required to resolve the wave field with a tolerable accuracy. Furthermore, a drawback of the FD-methods is the difficulty of representing complex geometries using the pointwise grid in a convenient way.

To improve the accuracy, high order FD methods have been developed [92, 181]. For example, in a fourth order method, the second derivative in 1D is approximated using [92, 181]

$$\frac{\partial^2 p}{\partial x^2}(x) = \left(1 + \frac{h^2}{12} D_{xx}\right)^{-1} D_{xx} p(x) + \mathcal{O}(h^4).$$

Alternatively, the undifferentiated terms at a given point can be expressed as a weighted average of values at adjacent points. Or, a resolution κh dependent parameter can be included in the finite difference derivative [92]. The error analysis of the FDM for wave problems is carried out for example in [92, 181, 191]

The time domain variant of FDM is called the finite difference time domain method (FDTD). A typical approach uses second order accurate derivatives in time and the second or fourth order derivatives in space. Although finite difference methods can suffer from the need of fine discretization, they are still extensively used for pulsed waves in medical acoustics , see e.g. [51, 83, 141, 148, 159]. The FDTD for elastic waves has a long history of being used in the simulation of seismic waves, see e.g. [122]. An excellent review of the high-order FDTD (and time domain finite element methods) can be found from [42].

Despite the heavy computational burden, the FDTD method can be used for time-harmonic (i.e. continuous wave (CW)) fields [177]. In that case, the time iteration must be continued until the steady state behavior of the CW field is reached. A significant number of iterations may be needed since the length of a time step dt, in the case of the second order accurate method in space, is limited by the Courant-Friedrichs-Levy number

$$\mathrm{CFL} = c\frac{dt}{h} < \frac{1}{\sqrt{d}},$$

where c is the propagation speed of the wave and d is the spatial dimension of the problem. Similar stability conditions, although more relaxed, can be derived for the high-order methods [42].

The convergence of the time-domain solution to the solution of time-harmonic problem can be remarkably slow. The convergence speeds up if the time-dependent wave problem is reformulated as an exact controllability problem [27]. By using the periodicity of the time-harmonic solution, the problem can be written as a least-squares problem which can be solved with a conjugate gradient algorithm. For time discretization, the method uses the standard finite difference scheme. At each time step one must solve two wave equations and an elliptic problem. Numerical experiments in [27] for Helmholtz scattering problems show huge improvement in convergence compared to a time-domain method without control.

Despite the above mentioned weaknesses, FD methods are widely used for the numerical simulation of acoustic and elastic waves. A strength of these methods is their simple implementation for different kinds (also non-linear) of wave problems. Furthermore, there is an abundance of commercial and freeware software that utilize these methods.

3.2.2 Finite element method

The finite element method (FEM) can be considered as a "gold standard" for solving numerically elliptic partial differential equations. Since the early analysis of the FEM beginning in the 1980's [9, 77, 78], the FEM with an absorbing boundary condition has been actively studied for unbounded Helmholtz problem. To be able to compare the FEM with more novel methods, an outline of the FEM for the Helmholtz and elastic wave equation are given in this section. Since the FE method relies on discretizing a weak formulation of the problem, the standard variational setting for the Helmholtz and elastic wave equation are briefly summarized. Then the weak forms can be discretized using the Galerkin method and standard finite element piecewise polynomial basis functions. For a more detailed treatment of the FEM, see [26, 112].

Helmholtz problem

To obtain a weak formulation, the Helmholtz equation (2.28) is multiplied by a test function $v \in H^1(\Omega)$ and integrated over the computational domain Ω

$$\int_\Omega \left[\nabla \cdot \left(\frac{1}{\rho} \nabla \right) p + \frac{\kappa^2}{\rho} p \right] v = 0, \tag{3.28}$$

where the test function space is defined as the Sobolev space $H^1(\Omega) = \{v \mid ||\nabla v||^2 + ||v||^2 < \infty\}$ and where $|| \cdot ||^2$ is the L^2-norm. Using suitable integration by parts, the variational problem can be defined as finding $p \in H^1(\Omega)$ such that

$$a(p, v) = -\int_\Omega \frac{1}{\rho} \nabla p \cdot \nabla v + \int_\Omega \frac{\kappa^2}{\rho} pv + \int_\Gamma \frac{1}{\rho} \frac{\partial p}{\partial n} v = 0 \quad \forall v \in H^1(\Omega). \tag{3.29}$$

Appropriate boundary conditions can included in the third term on the left hand side or by further restricting the space of trial and test functions. For example, the boundary condition on Γ can be given in the form

$$\left(\frac{1}{\rho}\frac{\partial p}{\partial n} - i\sigma p\right) = Q\left(-\frac{1}{\rho}\frac{\partial p}{\partial n} - i\sigma p\right) + g, \tag{3.30}$$

where $Q \in \mathbb{C}$, $|Q| < 1$ and; g and σ are known functions on Γ. This boundary condition is chosen since it will be used later with the ultra weak variational formulation. By adjusting the parameters Q, σ and g, various different boundary conditions can be implemented using (3.30). For example, by choosing $Q = 1$ equation (3.30) reduces to the Neumann type condition $\frac{\partial p}{\partial n} = \frac{1}{2}\rho g$. Whereas $Q = -1$ gives the Dirichlet condition $p = \frac{i}{2\sigma}g$.

The boundary function σ can be chosen for example as

$$\sigma = \frac{\Re(\kappa)}{\rho}. \tag{3.31}$$

Then, provided that $Q = 0$, $g = 0$ and $\kappa \in \mathbb{R}$, the equation (3.30) reduces to the absorbing boundary condition (3.2).

The boundary condition (3.30) can be rewritten as

$$\frac{1}{\rho}\frac{\partial p}{\partial n} = i\sigma\frac{1-Q}{1+Q}p + \frac{1}{1+Q}g. \tag{3.32}$$

Hence, the substitution of (3.32) in (3.29) leads to the weak problem of finding $p \in H^1(\Omega)$

$$a(p, v) = L(v), \quad \text{for all } v \in H^1(\Omega), \tag{3.33}$$

where

$$a(p, v) = -\int_\Omega \frac{1}{\rho}\nabla p \cdot \nabla v + \int_\Omega \frac{\kappa^2}{\rho}pv + \int_\Gamma i\sigma\frac{1-Q}{1+Q}pv, \tag{3.34}$$

and

$$L(v) = \int_\Gamma \frac{1}{1+Q}gv. \tag{3.35}$$

For the finite element approximation of (3.33), the computational domain Ω is covered with a regular finite element mesh consisting of N elements and M vertices with the element size parameter h denoting the maximum diameter of the elements (types of meshes used in this thesis will be discussed later). To discretize the weak Helmholtz problem (3.33), it is useful to construct a space $S_h = \text{span}\{\varphi_1, ..., \varphi_M\} \subset H^1(\Omega)$ where $\varphi_j,\ j = 1, .., M$ are piecewise linear polynomial finite element basis functions on the mesh with compact support such that

$$\varphi_j(r_\ell) = \begin{cases} 1 & j = \ell \\ 0 & j \neq \ell \end{cases},$$

where r_ℓ is the ℓth node in the mesh.

Now the FEM approximation p_h can be written as

$$p_h = \sum_{j=1}^{M} \beta_j \varphi_j, \tag{3.36}$$

where $\beta_j,\ j = 1, ..., M$ are coefficients to be solved. In addition, in the Galerkin approach the test functions are chosen by $v = \varphi_\ell$. By substituting these to (3.33), the problem can be written as the matrix equation

$$(S - M + B)\beta = F, \tag{3.37}$$

where $\beta = (\beta_1, ..., \beta_M)^\top$. Furthermore, S, M and B correspond to the terms in (3.34), respectively, and F arises from the right hand side of (3.33). Traditionally, S is known as the stiffness matrix and M as the mass matrix. Since this FEM approximation uses piecewise polynomials to represent the field p_h throughout an element it easily provides an approximation of the pressure at any point in space.

To understand the accuracy of the FEM for wave problems, a short review of error estimates is given next. The accuracy of the finite element approximation can be controlled with two factors. First, the element size can be made smaller to improve accuracy. This approach is known as the h-refinement [114]. Or second, the polynomial degree of the basis functions can be increased (known as p-refinement). Combination of these two is called hp-refinement (or hp-FEM [115]).

A rule of thumb for the piecewise linear FEM is that $\lambda/h \approx 10$, that is, approximately ten discretization points per wavelength are needed for tolerable accuracy [114]. For high wave numbers, however, FE (or FD) methods suffer from numerical pollution, meaning that the accuracy deteriorates with the wave number even if κh remains constant. More precisely, the error estimate for the one dimensional FEM using piecewise linear elements is of the form

$$\frac{|p - p_h|_1}{|p|_1} < C_1\theta + C_2\kappa\theta^2, \tag{3.38}$$

where $|\ \cdot\ |_1$ is the $H^1(\Omega)$-seminorm, C_1, C_2 are constants and $\theta = \kappa h$ [112]. From this formula, it is evident that the error increases linearly with κh when κ is small while the second "polluting" term becomes significant when κ is large.

Similar estimate can be derived for higher order basis functions. Then, the error is given by (3.38) with

$$\theta = \left(\frac{\kappa h}{p}\right)^p, \tag{3.39}$$

where p is now the polynomial degree of the basis functions [112].

Navier problem

The finite element formulation of the elastic wave field can be derived correspondingly as for the Helmholtz problem. However, for practical computations, a few

notable exceptions exist. The displacement field u to be solved is vector valued and it consists of two components u_P and u_S which have different wavelengths. The wavelength of S-wave is much shorter (for most solids about a half of the P-wave counterpart) and therefore, the mesh size h must adjusted dense enough to resolve both components.

The derivation of the weak form begins by introducing a shorthand notation. Let

$$\Delta^e u = \mu \Delta u + (\Lambda + \mu) \nabla (\nabla \cdot u).$$

Then the weak form of the Navier equation (2.10) can be written as

$$\int_\Omega (\Delta^e u + \omega^2 \rho u) \cdot v = 0,$$

where $v \in (H^1(\Omega))^d$ is a test vector and d is the dimension of the problem. Following [101] the weak formulation is obtained using the Betti formulas [131]

$$-a(u,v) + \int_\Gamma T^{(n)}(u) \cdot v + \omega^2 \rho \int_\Omega u \cdot v = 0, \tag{3.40}$$

where

$$a(u,v) = \Lambda \int_\Omega (\nabla \cdot u)(\nabla \cdot v) + \frac{\mu}{2} \int_\Omega (\nabla u + (\nabla u)^\top) : (\nabla v + (\nabla v)^\top). \tag{3.41}$$

The double dot operation between two tensors $A = a_{ij}$ and $B = b_{ij}$ is defined as

$$A : B = \sum_i \sum_j a_{ij} b_{ij}. \tag{3.42}$$

Due to the particular choice of example for the comparison of the finite element method with the UWVF later in this thesis, the boundary condition

$$\left(T^{(n)}(u) - i\sigma u\right) = Q\left(-T^{(n)}(u) - i\sigma u\right) + g \quad \text{on } \Gamma, \tag{3.43}$$

where $\sigma \in \mathbb{R}^{d \times d}$ will be used. As for the Helmholtz case, it is assumed that $Q \in \mathbb{C}$ and $|Q| < 1$.

Solving this equation for $T^{(n)}(u)$ gives

$$T^{(n)}(u) - i\left(\frac{1-Q}{1+Q}\right)\sigma u = \left(\frac{1}{1+Q}\right) g \quad \text{on } \Gamma. \tag{3.44}$$

Using this equality in (3.40), the variational problem can be defined as finding $u \in (H^1(\Omega))^d$ such that

$$-a(u,v) + \int_\Gamma \left(i\left(\frac{1-Q}{1+Q}\right)\sigma u + \left(\frac{1}{1+Q}\right) g \right) \cdot v + \omega^2 \rho \int_\Omega u \cdot v = 0, \tag{3.45}$$

for all $v \in (H^1(\Omega))^d$.

The approximation by continuous polynomial finite elements is obvious. The finite element mesh covers the domain Ω and has maximum element diameter h. Analogously to the Helmholtz case, on this mesh one can construct a space S_h of continuous piecewise linear finite element functions. The finite element solution $u_h \in (S_h)^d$ can be represented as a linear combination of the basis functions and it satisfies

$$a(u_h, v_h) - \int_\Gamma \left(i \left(\frac{1-Q}{1+Q} \right) \sigma u_h + \left(\frac{1}{1+Q} \right) g \right) \cdot v_h - \omega^2 \rho \int_\Omega u_h \cdot v_h = 0, \quad (3.46)$$

for all $v_h \in (S_h)^d$. For example, in 2D ($d = 2$) piecewise linear Galerkin scheme, the FEM approximation and the test function can be selected as

$$u_h = \sum_{j=1}^{M} \begin{pmatrix} \beta_j^1 \\ \beta_j^2 \end{pmatrix} \varphi_j \quad \text{and;} \quad v_h = \begin{pmatrix} \varphi_\ell \\ 0 \end{pmatrix} \quad \text{or} \quad v_h = \begin{pmatrix} 0 \\ \varphi_\ell \end{pmatrix}, \quad \ell = 1, ..., M, \quad (3.47)$$

where β_j^1 and β_j^2 are the coefficients to be solved and φ_ℓ is the piecewise linear basis function associated with node number ℓ.

3.2.3 Boundary integral methods

Consider an acoustically impenetrable inhomogeneity Ω surrounded by an infinite homogeneous medium in $\Omega^+ = \mathbb{R}^d \backslash \Omega$. Furthermore, let Γ be the boundary of Ω. The boundary integral equation methods are based on the Green's representation of the Helmholtz problem [47, 132]

$$p(r) = \int_\Gamma \left[p(r_0) \frac{\partial \Phi(r, r_0)}{\partial n} - \Phi(r, r_0) \frac{\partial p(r_0)}{\partial n} \right] ds(r_0) \quad \text{in } \Omega^+, \quad (3.48)$$

where $r_0 \in \Gamma$ and $r \in \Omega^+$. The function $\Phi(r, r_0)$ is the fundamental solution of the Helmholtz problem in a homogeneous medium. For 2D and 3D the fundamental solution is

$$\Phi(r, r_0) = \frac{i}{4} H_1^{(0)}(\kappa |r - r_0|) \quad \text{and} \quad \Phi(r, r_0) = \frac{1}{4\pi} \frac{e^{i\kappa |r - r_0|}}{|r - r_0|}, \quad (3.49)$$

respectively. The Green's representation follows from the weak form of the Helmholtz problem (3.28) with the choice $v = \Phi$ and a suitable integration by parts [132].

The main advantage of the boundary integral methods is that the solution is sought utilizing the fundamental solutions of the problem. Therefore, the solution automatically satisfies the Sommerfeld radiation condition. In addition, since the formulation reduces to medium interfaces only, the spatial dimension of the problem is reduced by one.

Various discretization methods for the boundary integral formulations of the Helmholtz problem have been proposed. These include, for example, the Nyström

method [48], collocation method [129] and different types of Galerkin boundary element methods [132].

However, the integral equation approach suffers from the computational complexity. Although only the surfaces of the inhomogeneities must be discretized, the resulting matrix systems are relatively large at high wave numbers. This is due to need of dense discretization (typically, the rule of thumb $\lambda/h \approx 10$ must hold). Furthermore, the matrices arising from the boundary integral method are full and non-symmetric. If the computational domain consists of multiple inhomogeneities, a drawback of the method is that each material interface must be discretized which leads to a complex system of coupled integral equations.

In a computational cost comparison, the boundary element methods have been shown to be more expensive than the previously introduced finite element method [28, 89]. The solving of boundary integral equations with iterative methods requires the computation of multiple full matrix-vector products. This procedure can be accelerated by using the fast multipole method (FMM), see e.g. [43, 52, 174]. Improved by the FMM, boundary integral equations have become an efficient and popular means for solving large-scale scattering problems [52].

3.3 Improved methods

This section is dedicated to the discussion of improved finite element (or finite element type) methods. Moreover, improvements of the boundary element method and alternatives for the ABC or PML to truncate the computational domain are reviewed briefly.

The rule of thumb for low order FEM indicates that the computation mesh must be sufficiently dense to guarantee an accurate approximation for wave problems. At high wave numbers this rapidly leads to computational burden which is intolerable even for the largest existing computers. To reduce the computational complexity, various improvements for the FEM have been proposed. Also other finite element type methods have shown significant improvement in comparison to the low order FEM.

Due to the oscillatory nature of solutions of the wave problems, it is clear that very high order polynomial basis functions must be used to capture the wave solution in large elements [2]. A high order finite element methods is obtained by choosing the basis functions as high order polynomials. This so-called spectral element method (SEM) for the 2D Helmholtz problem has been studied in [151]. The results show that the SEM reduces the computational burden, time and numerical pollution in comparison to the second order finite elements.

In the least-squares finite element approach an additional term is included to the weak forms (3.33) or (3.40) which contains least-squares of the residuals for the problem at hand. In the Galerkin least-squares (GLS) method [90, 189] the added term contains residuals in the element interiors while in the residual-based finite element method of [156], the residuals are computed in element interiors and on inter-element boundaries. A comparison of these two approaches with piecewise linear FEM is made in [155]. Both least-squares methods performed better

than the standard FEM and the residual-based method showed reduced numerical pollution error. The GLS method for elastic wave propagation is analyzed in [87].

Although the residual-based least-squares approach reduces the pollution effect, it does not significantly relax the rule of thumb for the mesh density. An improvement toward coarser meshes has been made in [10] where a method for including a priori information of the solution into the FEM basis functions is proposed. The method is named the partition of unity finite element method (PUM). In the PUM, the finite element basis contains the standard polynomial shape function $\varphi_j(r)$, having the property (3.2.2), multiplied by a function $L_j(r)$ which is a solution of the underlying equation. The PUM approximation for the Helmholtz equation can be written now as

$$p_h = \sum_{j=1}^{M} L_j(r)\varphi_j(r). \tag{3.50}$$

To capture the oscillatory behavior of the solution, plane waves of the form

$$L_j(r) = \sum_{k=1}^{N_k} A_k e^{i\kappa d_k \cdot r} \tag{3.51}$$

are typically used in the basis functions [134, 135, 150, 157]. Here $A_k,\ k = 1, ..., N_k$ are the coefficients to be solved and d_k is the direction of propagation of the plane wave.

In the case of piecewise polynomial basis functions, the entries for the FEM matrices (3.37) can be computed exactly with a simple Gauss integration quadrature. For oscillatory basis functions in the PUM, very high order quadratures are needed which has led to the development of semi-analytical quadratures specialized for the plane waves [20]. Moreover, the PUM can suffer from severe ill-conditioning if too many plane waves are used for a single element. This originates partly from the fact that adjacent plane waves in the basis become nearly linearly dependent if the number of basis functions is increased too high [135, 136]. However, further studies are needed for understanding better the origin of the instability. To improve the stability of PUM, a regularization-type approach has been proposed in [157].

An alternative approach to the FEM with continuous plane basis functions is called the discontinuous enrichment method (DEM) [63] in which the plane wave function L_j is added to the continuous polynomial finite element basis φ_j. The continuity of the enrichment functions is approximately enforced by Lagrange multipliers. Omitting the finite element basis, the method reduces to the discontinuous Galerkin method (DGM) [64]. In terms of the number of degrees of freedom, the DGM shows superior performance compared with low order finite element methods [64]. The same study shows that in comparison to the PUM, the discontinuous Galerkin method leads to improved conditioning of the resulting matrix system. Methods for eliminating the Lagrange multipliers on the inter-element coupling in the DGM (although not for wave problems) are discussed in the review article [200].

While the DGM in [64] uses Lagrange multipliers and a variational method to enforce continuity of the solution across element interfaces, in the least-squares (LS) method the continuity is achieved by minimizing a quadratic functional [152, 184]. The solution of the LS-method can be approximated using plane wave basis functions as in (3.50). In [152], the use of Bessel functions as a basis functions is also analyzed. However, the results suggest that plane waves are more practically useful since the resulting integrals arising in the building of the matrix entries can be computed in a closed form.

The use of plane wave basis functions is not limited to domain based (i.e. volume discretization) methods only. A method to include plane wave basis functions in the integral equation formulation of the Helmholtz equation was first proposed in the micro local discretization scheme [54, 53]. In [162], similar basis functions to those in (3.50) are used for the 3D boundary element formulation of the Helmholtz equation. Using separate sets of plane wave basis functions for P- and S- waves, the method has been extended also to the Navier equation [161, 163]. Although these methods have shown notable reduction in the number of degrees of freedom, their drawback is the need for using high-order integration quadratures which causes extremely slow computation of the system matrix.

An important step in the numerical simulation of wave problems has been the development of parallel computing. A sophisticated numerical scheme on multiprocessor supercomputers or PC-cluster makes possible very large-scale wave simulations. An impressive example of this is the parallelized time-domain spectral element simulation of seismic wave propagation [126, 127, 128].

To be able to compute finite element methods on parallel computers, a wave problem can be decomposed into a set of subproblems with a smaller size. Then the subproblems are distributed into and handled by separate processors. A widely used approach for wave problems is the non-overlapping domain decomposition method in which the computational mesh is divided into smaller parts on which a new subproblem is defined. The method is non-overlapping since the subproblems communicate only through their interfaces, see e.g. [16, 44, 124, 165, 170]. The coupling can be done using suitable physical transmission conditions and the solution in each subdomain is updated iteratively.

An interesting parallelized solver for the 3D Helmholtz scattering problems has been proposed in [97]. It is based on the algebraic *fictitious domain method* in which the original discrete matrix equation is replaced with a new enlarged system. The term fictitious domain follows from the fact that the new system corresponds to the geometric embedding of the original computational domain into another domain with a simple geometry. The new enlarged matrix system allows the construction of efficient preconditioners and the iterative solution of the problem can be carried out in a low-dimensional subspace.

A common feature of all methods in this section which use plane-wave basis functions is the lack of analysis of the methods for problems with variable material properties. An exception to this will be given next. By using a similar splitting of the problem as the domain decomposition methods, a different variational formulation (called the ultra weak variational formulation (UWVF) by its developers)

has been proposed. The UWVF was first introduced for general PDEs in [56] and applied to the Helmholtz and Maxwell problems in [29, 30, 31]. Furthermore, the method for Helmholtz problem in an inhomogeneous medium has been outlined in [29].

The UWVF method has similarities with the improved finite element methods since it can use standard finite element meshes for the spatial discretization and allows the incorporation of a priori information into the approximating subspace. In particular, the implementation with plane wave basis functions is relatively simple. In addition, as will be shown later in this thesis, it is possible to develop a feasible preconditioning method for UWVF matrices.

The UWVF method for ultrasound problems is the main theme of this thesis hence the method is analyzed in more detail in the following chapters. Before proceeding to the UWVF, some additional numerical methods to ABC and PML for approximating the Sommerfeld radiation condition are considered briefly.

Alternative methods to approximate the Sommerfeld condition

Hitherto, the review of improved methods has been limited to methods that reduce the computational burden related to high-frequency wave problems. The other important factor affecting the accuracy of numerical methods for unbounded problems is the truncation of the computational domain. As discussed in Section 3.1, differential operators can used to approximate the Sommerfeld radiation condition on the external boundary of the domain or the domain can be surrounded by the PML.

Since the solution of the integral equation method (3.48) satisfies the Sommerfeld condition, coupling these methods with the FEM provides an accurate alternative for the ABCs or PML [100]. More precisely, the finite element scheme is used in an interior region which encloses possible material inhomogeneities. On the exterior boundary, the discretized integral equation is formulated and coupled with the finite element method. This approach provides an excellent accuracy but is computationally rather heavy due to the presence of full integral equation matrices. A similar idea is analyzed in [125] where the FEM is coupled with a Hankel function expansion for the field.

In some applications, elastic or viscoelastic medium can be embedded in an acoustic fluid. For such problems, methods which couple the elastic finite element formulation with acoustic boundary element formulation has been proposed [33, 55]

Another alternative is to couple the finite element scheme with *infinite elements* (see reviews [4, 18, 70]) which extend from the exterior boundary to infinity. The behavior of the 3D Helmholtz problem at a large distance from the source is defined by the Atkinson-Wilcox expansion [196]

$$p(R,\theta,\phi) = \frac{e^{i\kappa R}}{R} \sum_{n=0}^{\infty} \frac{F_n(\theta,\phi)}{R^n},$$

where (R,θ,ϕ) are the spherical coordinates and F_n are arbitrary functions. A similar expansion can derived also for the 2D problems [117].

Then, if the FEM is used in the spherical domain Ω, the infinite element approximation for the Helmholtz problem in the exterior region $\mathbb{R}^3\backslash\Omega$ can be written in the form

$$p_h^M(R,\theta,\phi) = p_M(R)p_h(\theta,\phi),$$

where

$$p_M(R) = \sum_{k=1}^{M} A_k \frac{e^{i\kappa R}}{R^k}.$$

Thus infinite elements can efficiently imitate the far-field behavior of the Helmholtz problem. Moreover, the infinite element approximation extends from the boundary $\partial\Omega$ to infinity which in some infinite element formulations provides a means to solve the far-field in the region $\mathbb{R}^3\backslash\Omega$. This is a considerable improvement compared to differential operator ABCs. Those provide the solution in the bounded region Ω only. The extension of the solution outside the bounded domain necessitates the use of the integral equation formulation of the Helmholtz problem (3.48).

Comparison of the infinite element method with various differential operator ABCs is done in [180]. The results suggest that the accuracy of infinite elements approximation in high wave numbers is better than the accuracy of the ABCs. However, the use of high order infinite elements leads to poorer conditioning of the problem and increased computational effort. Applied to a class of coupled structural acoustic problems in [28], the infinite elements have, however, a superior computational cost reduction over the boundary element methods.

Chapter IV

Ultra weak variational formulation

The general form of the ultra weak variational formulation (UWVF) was first introduced in [56]. Subsequently, the method was analyzed for the Helmholtz and Maxwell equation in 2D and 3D [29, 30, 31]. In addition, [29] includes the formulation of the UWVF for the Helmholtz problem in an inhomogeneous medium.

The idea of the UWVF is to decompose the original problem into a set of subproblems which are connected using an impedance boundary condition. For the geometric partition of the computational domain, the UWVF uses standard disjoint finite element meshes. Furthermore, each element of the mesh determines a single subproblem for the UWVF. By setting the material properties for each element to be constant, the approximating space for the discrete UWVF can be constructed using free-space solutions of each subproblem.

In this chapter, the UWVF for the Helmholtz and time-harmonic Navier equation are derived. Moreover, the discretized UWVFs are introduced for both problems. Since the perfectly matched layer discussed in Section 3.1.3 leads to a modified Helmholtz equation, the PML version of the UWVF for the Helmholtz problem is also introduced.

4.1 Helmholtz problem

In this section the UWVF for the inhomogeneous Helmholtz problem (2.28) is outlined. Using the notation of the previous section, one can define a domain Ω having the boundary Γ and outward unit normal n. The Helmholtz problem for the acoustic pressure field in an inhomogeneous medium occupying Ω can be formulated as follows

$$\nabla \cdot \left(\frac{1}{\rho}\nabla p\right) + \frac{\kappa^2}{\rho} p = 0 \quad \text{in } \Omega, \tag{4.1}$$

$$\left(\frac{1}{\rho}\frac{\partial p}{\partial n} - i\sigma p\right) = Q\left(-\frac{1}{\rho}\frac{\partial p}{\partial n} - i\sigma p\right) + g \quad \text{on } \Gamma, \tag{4.2}$$

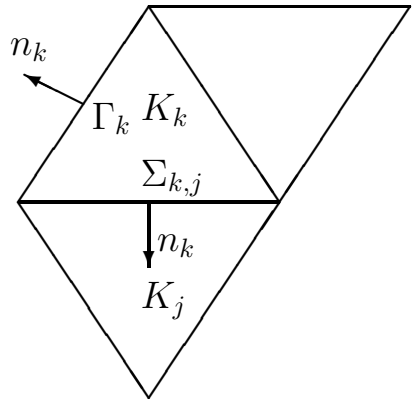

Figure 4.1: A part of the mesh. The interface between elements K_k and K_j is $\Sigma_{k,j}$. The outward unit normal on the boundary ∂K_k is n_k. Furthermore, if the element is on the exterior boundary, the corresponding part of ∂K_k is denoted by Γ_k.

where $\kappa = \kappa(r) \in \mathbb{C}$ is the spatially varying wave number that satisfies $\Re(\kappa) > 0$ and $\Im(\kappa) \geq 0$. On the boundary the parameter $Q \in \mathbb{C}$ with $|Q| \leq 1$. The material density $\rho = \rho(r)$ and the parameter σ are real and positive. Finally, the complex valued source function on the exterior boundary Γ is denoted by g.

For the UWVF, let the domain Ω be partitioned into a collection of disjoint finite elements $\{K_k\}_{k=1}^N$. In two dimensional problems each element K_k is a triangle except near curved interfaces or boundaries where K_k can be curvilinear triangle. In three dimensional studies, tetrahedral elements have been used. The limitation to triangular and tetrahedral elements is not a property of the UWVF but rather these shapes are chosen due to the abundance of mesh generators using these elements. In principle, elements of other shapes are possible or even a mixture of different element in a same mesh can be used. This aspect, however, is not studied further here.

Now, let $\Sigma_{k,j}$ denote the edge between element K_k and element K_j, and let n_k denote the outward unit normal on ∂K_k . The exterior edges are denoted by $\Gamma_k = \partial\Omega \cap \partial K_k$, see Fig 4.1.

The parameters ρ and κ are assumed to be piecewise constants, so that $\rho_k \equiv \rho|_{K_k}$ and $\kappa_k \equiv \kappa|_{K_k}$. The problem (4.1)-(4.2) can now be decomposed into sub-

problems for each element K_k, $k = 1, \cdots, N$

$$\Delta p_k + \kappa_k^2 p_k = 0 \qquad \text{in } K_k, \tag{4.3}$$

$$p_k = p_j \qquad \text{on } \Sigma_{k,j}, \tag{4.4}$$

$$\frac{1}{\rho_k}\frac{\partial p_k}{\partial n_k} = -\frac{1}{\rho_j}\frac{\partial p_j}{\partial n_j} \qquad \text{on } \Sigma_{k,j}, \tag{4.5}$$

$$\left(\frac{1}{\rho_k}\frac{\partial p_k}{\partial n_k} - i\sigma p_k\right) = Q\left(-\frac{1}{\rho_k}\frac{\partial p_k}{\partial n_k} - i\sigma p_k\right) + g \qquad \text{on } \Gamma_k, \tag{4.6}$$

where $p_k = p|_{K_k}$. As discussed in Section 2.4, the transmission conditions (4.4) and (4.5) guarantee the continuity of the acoustic pressure and particle velocity over the element interfaces.

It is shown in [16] that the transmission conditions can be written in the coupled form

$$\frac{1}{\rho_k}\frac{\partial p_k}{\partial n_k} - i\sigma p_k = -\frac{1}{\rho_j}\frac{\partial p_j}{\partial n_j} - i\sigma p_j, \text{ and } \frac{1}{\rho_k}\frac{\partial p_k}{\partial n_k} + i\sigma p_k = -\frac{1}{\rho_j}\frac{\partial p_j}{\partial n_j} + i\sigma p_j, \tag{4.7}$$

where σ is an appropriate real valued parameter that is defined on the element boundary ∂K_k. More precisely, σ is a piecewise constant parameter so that it is constant on each face of the element but the value of σ can vary between faces of the element. In addition, σ is continuous across interfaces $\Sigma_{k,j}$. Since σ must have the same dimensions as κ/ρ [16], an obvious choice is the mean value of $\Re(\kappa)/\rho$ over the interface $\Sigma_{k,j}$

$$\sigma = \frac{1}{2}\left(\frac{\Re(\kappa_k)}{\rho_k} + \frac{\Re(\kappa_j)}{\rho_j}\right) \quad \text{on } \Sigma_{k,j}. \tag{4.8}$$

Analogously to the finite element method in Section 3.2.2, on the exterior boundary Γ, the choice of the parameters Q, σ and g must be consistent with the boundary condition on Γ. For example, an important boundary condition is obtained with $Q = 0$, $g = 0$ and

$$\sigma = \frac{\Re(\kappa_k)}{\rho_k}.$$

Provided that $\kappa_k \in \mathbb{R}$, equation (4.6) corresponds to the zeroth order (i.e. Sommerfeld type) absorbing boundary condition

$$\frac{\partial p_k}{\partial n_k} - i\sigma p_k = 0. \tag{4.9}$$

Having decomposed the problem, the UWVF can be developed. Using integration by parts it is easy to see that provided that p_k is sufficiently smooth

($p_k \in H^2(K_k)$ for all k is sufficient) the following equality holds

$$\begin{aligned}
&\sum_{k=1}^{N} \int_{\partial K_k} \frac{1}{\sigma} \left(-\frac{1}{\rho_k} \frac{\partial}{\partial n_k} - i\sigma \right) p_k \overline{\left(-\frac{1}{\rho_k} \frac{\partial}{\partial n_k} - i\sigma \right) v_k} \\
&= \sum_{k=1}^{N} \int_{\partial K_k} \frac{1}{\sigma} \left(\frac{1}{\rho_k} \frac{\partial}{\partial n_k} - i\sigma \right) p_k \overline{\left(\frac{1}{\rho_k} \frac{\partial}{\partial n_k} - i\sigma \right) v_k} \\
&- \sum_{k=1}^{N} 2\frac{i}{\rho_k} \int_{\partial K_k} \left(\frac{\partial p_k}{\partial n_k} \overline{v}_k - p_k \frac{\partial \overline{v}_k}{\partial n_k} \right),
\end{aligned} \tag{4.10}$$

for all smooth test functions v_k and where the bars stand for complex conjugate.

Assuming that p_k is the solution of the Helmholtz equation (4.3). Then, for all piecewise smooth test functions v_k that are solutions of the adjoint Helmholtz equation

$$\Delta \overline{v}_k + \kappa_k^2 \overline{v}_k = 0, \quad \text{in } K_k, \tag{4.11}$$

the integral in the last term of (4.10) vanishes via the Green's theorem

$$\begin{aligned}
&\int_{\partial K_k} \left(\frac{\partial p_k}{\partial n_k} \overline{v}_k - p_k \frac{\partial \overline{v}_k}{\partial n_k} \right) = \int_{K_k} \left(\Delta p_k \overline{v}_k - p_k \Delta \overline{v}_k \right) \\
= &\int_{K_k} \left(\kappa_k^2 p_k \overline{v}_k - p_k \kappa_k^2 \overline{v}_k \right) = 0.
\end{aligned}$$

For the UWVF a new function χ_k is defined on the skeleton of the mesh

$$\chi_k = \left(\left(-\frac{1}{\rho_k} \frac{\partial}{\partial n_k} - i\sigma \right) p_k \right) \Big|_{\partial K_k}, \quad 1 \le k \le N. \tag{4.12}$$

By substituting the impedance boundary conditions (4.6) and (4.7) to the first term on the right hand side of (4.10) and by using (4.12) one obtains

$$\begin{aligned}
&\sum_{k=1}^{N} \int_{\partial K_k} \frac{1}{\sigma} \chi_k \overline{\left(-\frac{1}{\rho_k} \frac{\partial}{\partial n_k} - i\sigma \right) v_k} - \sum_{k=1}^{N} \sum_{j=1}^{N} \int_{\Sigma_{k,j}} \frac{1}{\sigma} \chi_j \overline{\left(\frac{1}{\rho_k} \frac{\partial}{\partial n_k} - i\sigma \right) v_k} \\
- &\sum_{k=1}^{N} \int_{\Gamma_k} \frac{Q}{\sigma} \chi_k \overline{\left(\frac{1}{\rho_k} \frac{\partial}{\partial n_k} - i\sigma \right) v_k} = \sum_{k=1}^{N} \int_{\Gamma_k} \frac{1}{\sigma} g \overline{\left(\frac{1}{\rho_k} \frac{\partial}{\partial n_k} - i\sigma \right) v_k},
\end{aligned} \tag{4.13}$$

for all piecewise smooth functions v_k satisfying (4.11). Terms of the double summation in the second term of the left hand side are assumed to exist only if two elements share a common face $\Sigma_{k,j}$. Equation (4.13) is called the ultra weak variational formulation of the Helmholtz problem in an inhomogeneous medium (4.1) and (4.2).

To simplify the discussion on the discrete problem and to allow comparison with the UWVF for the elastic wave problems introduced later in this thesis, it is possible define an operator

$$F_k : L^2(\partial K_k) \to L^2(\partial K_k) \tag{4.14}$$

such that if $y_k \in L^2(\partial K_k)$ then $F_k(y_k) \in L^2(\partial K_k)$ is given by

$$F_k(y_k) \quad = \quad \left(\frac{1}{\rho_k}\frac{\partial}{\partial n_k} - i\sigma\right) v_k \quad \text{on } \partial K_k \tag{4.15}$$

where $v_k \in H^1(K_k)$ satisfies (4.11) and

$$\left(-\frac{1}{\rho_k}\frac{\partial}{\partial n_k} - i\sigma\right) v_k = y_k \text{ on } \partial K_k. \tag{4.16}$$

Using F_k the UWVF problem (4.13) may be rewritten as the problem of finding $\chi_k \in L^2(\partial K_k),\ k = 1, 2, \ldots, N$ such that

$$\begin{aligned} &\sum_{k=1}^{N} \int_{\partial K_k} \frac{1}{\sigma}\chi_k \overline{y}_k - \sum_{k=1}^{N}\sum_{j=1}^{N} \int_{\sum_{k,j}} \frac{1}{\sigma}\chi_j \overline{F_k(y_k)} - \sum_{k=1}^{N} \int_{\Gamma_k} \frac{Q}{\sigma}\chi_k \overline{F_k(y_k)} \\ = \quad &\sum_{k=1}^{N} \int_{\Gamma_k} \frac{1}{\sigma} g \overline{F_k(y_k)}, \end{aligned} \tag{4.17}$$

for all $y_k \in L^2(\partial K_k),\ k = 1, 2, \ldots K$. This formulation makes it clear that the unknown functions χ_k are computed on ∂K_k using as test functions y_k that are also functions on ∂K_k. Thus the UWVF generates a direct approximation to the field u and $\partial u/\partial n_k$ on the skeleton of the mesh $\partial K_k, k = 1, \ldots, N$. To compute u away from the skeleton involves a local post-processing step that will be discussed in Section 4.1.3. The discrete form of (4.17) will be formulated in the following section.

4.1.1 Discretization

Following [29, 30], a Galerkin approach is used for the discretization of the UWVF (4.17). For this, it is necessary to choose subspaces of the spaces $L^2(\partial K_k), k = 1, \ldots, N$ for the functions appearing in (4.17). To implement (4.17) one must be able to compute $F_k(y_k^a)$ for discrete functions y_k^a. Cessenat and Despŕes [29, 30] suggest the following strategy for constructing a discretization of $L^2(\partial K_k)$ that makes the computation of F_k trivial. For each K_k a finite family of functions $\varphi_{k,\ell}, \ell = 1, \ldots, N_k$ is chosen which satisfy equation (4.11) so

$$\Delta\overline{\varphi}_{k,\ell} + \kappa_k^2 \overline{\varphi}_{k,\ell} = 0 \quad \text{in } K_k \tag{4.18}$$

and $\varphi_{k,\ell} = 0$ on $\Omega \backslash \bar{K}_k$. Then the discrete space approximating $L^2(\partial K_k)$ consists of all functions y_k^a such that

$$y_k^a = \sum_{\ell=1}^{N_k} y_{k,\ell} \left(-\frac{1}{\rho_k}\frac{\partial}{\partial n_k} - i\sigma\right) \varphi_{k,\ell} \quad k = 1, 2, \ldots, N, \tag{4.19}$$

where $\{y_{k,\ell}\}_{\ell=1}^{N_k}$ are arbitrary constants. Similarly,

$$\chi_k^a = \sum_{\ell=1}^{N_k} \chi_{k,\ell} \left(-\frac{1}{\rho_k}\frac{\partial}{\partial n_k} - i\sigma\right) \varphi_{k,\ell}, \tag{4.20}$$

where the expansion coefficients $\{\chi_{k,\ell}\}_{\ell=1}^{N_k}$ are the unknown parameters to be computed. Of course $F_k(y_k^a)$ is easy to compute since

$$F_k(y_k^a) = \sum_{\ell=1}^{N_k} y_{k,\ell} \left(\frac{1}{\rho_k} \frac{\partial}{\partial n_k} - i\sigma \right) \varphi_{k,\ell}. \tag{4.21}$$

The discrete UWVF is then obtained by replacing χ_k by χ_k^a and y_k by y_k^a in (4.17). One must bear in mind that the aim of the discrete UWVF is to obtain an approximation for the function χ_k. A method for computing the approximation of the pressure field p_k from χ_k^a is discussed in Section 4.1.3.

There are still a number of possible choices for the functions $\varphi_{k,\ell}$. Obviously $\{\varphi_{k,\ell}\}_{\ell=1}^{\infty}$ is required to be a complete family of solutions in the sense that any function in $L^2(\partial K_k)$ can be approximated to any desired accuracy by a function of the form (4.19) provided N_k is chosen large enough. For example in 2D it would be possible to choose

$$\varphi_{k,\ell}(x) = J_{\ell-1}\left(\overline{\kappa}_k |x - x_k|\right) e^{i(\ell-1)\theta}, \quad 1 \leq \ell \leq N_k, \tag{4.22}$$

where $x \in \mathbb{R}^2$, $x_k \in K_k$, $J_{\ell-1}$ is the Bessel function of first kind and order $\ell - 1$; and θ is the angle in polar coordinates. For the least squares problem this basis does not offer a significant advantage over the basis that is chosen next [152]. In addition, the integrals in (4.17) must be computed by quadrature.

Thus, the choice advocated by Cessenat and Despŕes [29, 30] is used. This is the plane wave basis given by

$$\varphi_{k,\ell} = \begin{cases} \exp(i\overline{\kappa}_k d_{k,\ell} \cdot x) & \text{in } K_k \\ 0 & \text{elsewhere,} \end{cases}$$

where $d_{k,\ell}$ is a unit vector giving the direction of propagation of the wave. The wave plane basis for the element K_k in 2D can be constructed using angularly equispaced directions

$$d_{k,\ell} = \left(\cos\left(2\pi \frac{\ell - 1}{N_k} \right), \sin\left(2\pi \frac{\ell - 1}{N_k} \right) \right). \tag{4.23}$$

In 3D the equispaced directions are obtained from optimized spherical coverings [93]. These are computed by minimizing the maximum distance of any point on the unit sphere from the set of the N_k points.

The choice of equally spaced directions is not required by the UWVF. It is possible that another choice of directions might reduce the number of required directions if some *a priori* information on the solution is available but this topic is not studied here. Instead, the choice of basis functions is limited to varying the number of directions N_k between elements.

In the Galerkin approach the test function $v_{k,\ell}$ is chosen from the basis functions so that successively $v_{k,\ell} = \varphi_{k,\ell}$, $1 \leq \ell \leq N_k$ and $1 \leq k \leq N$. Then the discrete form of the UWVF can be written as the matrix equation [30]

$$(D - C)X = b, \tag{4.24}$$

where $X = (\chi_{11}, \ldots, \chi_{1N_k}, \chi_{21}, \ldots)^\top$ and D is the positive definite Hermitian block diagonal matrix

$$D = \begin{pmatrix} D_1 & 0 & \ldots & \ldots & 0 \\ 0 & \ddots & 0 & \ldots & 0 \\ \vdots & 0 & D_k & 0 & 0 \\ \vdots & \vdots & 0 & \ddots & 0 \\ 0 & 0 & 0 & 0 & D_N \end{pmatrix}.$$

The entries in D are

$$D_k^{\ell,m} = \int_{\partial K_k} \frac{1}{\sigma} \left(-\frac{1}{\rho_k} \frac{\partial \varphi_{k,m}}{\partial n_k} - i\sigma\varphi_{k,m} \right) \overline{\left(-\frac{1}{\rho_k} \frac{\partial \varphi_{k,\ell}}{\partial n_k} - i\sigma\varphi_{k,\ell} \right)}, \tag{4.25}$$

where the subscript of D refers to the block and the superscripts refer to the element in the block. The matrix C is also sparse and has a block structure. In the kth block row of the matrix C , the number of blocks corresponds to the number of faces in the element K_k. The entries in C are given by

$$\begin{aligned} C_{k,j}^{\ell,m} &= \int_{\Sigma_{k,j}} \frac{1}{\sigma} \left(\frac{1}{\rho_j} \frac{\partial \varphi_{j,m}}{\partial n_k} - i\sigma\varphi_{j,m} \right) \overline{\left(\frac{1}{\rho_k} \frac{\partial \varphi_{k,\ell}}{\partial n_k} - i\sigma\varphi_{k,\ell} \right)} \\ &+ \int_{\Gamma_k} \frac{Q}{\sigma} \left(-\frac{1}{\rho_k} \frac{\partial \varphi_{k,m}}{\partial n_k} - i\sigma\varphi_{k,m} \right) \overline{\left(\frac{1}{\rho_k} \frac{\partial \varphi_{k,\ell}}{\partial n_k} - i\sigma\varphi_{k,\ell} \right)}. \end{aligned} \tag{4.26}$$

The entries for the right hand side of the system are

$$b_k^\ell = \int_{\Gamma_k} \frac{1}{\sigma} g \overline{\left(\frac{1}{\rho_k} \frac{\partial \varphi_{k,\ell}}{\partial n_k} - i\sigma\varphi_{k,\ell} \right)}. \tag{4.27}$$

If the edges (or faces in 3D) of the elements are straight, the integrals above can be evaluated in closed form. The details for the analytical forms of the integrals in the 2D and 3D UWVF can be found from [29, 30]. In some of the 2D examples in next chapter, curved elements are also used. On curved element edges the integrals must be computed numerically. Note that it is vital to use curved elements, otherwise large errors can occur from approximating curved boundaries by multi-wavelength sized elements. However, in 3D studies of Chapter 6, only straight faced tetrahedra will be used.

For numerical stability it is suggested [29] that equation (4.24) can be solved in the form

$$(I - D^{-1}C)X = D^{-1}b. \tag{4.28}$$

This preconditioned approach requires inversion of the matrix D. Due to the block diagonal structure of D the inversion can be done block wise for each D_k separately. Using knowledge of the conditioning of the blocks the stability of the resulting matrix system (4.28) can be improved. This will be discussed in the following sections.

4.1.2 Changes in the UWVF due to the PML

The previous derivation of the UWVF was carried out for the Helmholtz equation (2.28). In this section the modifications in the UWVF arising from the use of the PML are given. Furthermore, the source term f_s of the inhomogeneous Helmholtz-PML equation (3.25) is also included to the UWVF.

Analogously to the standard Helmholtz equation, the Helmholtz-PML equation (3.25) can be decomposed into subproblems for each element K_k, $k = 1, \cdots, N$. In this way, one can define a collection of coupled problems as

$$\nabla \cdot A_k \nabla p_k + \kappa_k^2 \eta_k^2 p_k = f_s \eta_k^2 \qquad \text{in } K_k, \tag{4.29}$$

$$\frac{1}{\rho_k} n_k \cdot (A_k \nabla p_k) - i\sigma p_k = -\frac{1}{\rho_j} n_j \cdot (A_j \nabla p_j) - i\sigma p_j \qquad \text{on } \Sigma_{k,j}, \tag{4.30}$$

$$\frac{1}{\rho_k} n_k \cdot (A_k \nabla p_k) + i\sigma p_k = -\frac{1}{\rho_j} n_j \cdot (A_j \nabla p_j) + i\sigma p_j \qquad \text{on } \Sigma_{k,j}, \tag{4.31}$$

$$\left(\frac{1}{\rho_k} n_k \cdot (A_k \nabla p_k) - i\sigma p_k\right) = Q\left(-\frac{1}{\rho_k} n_k \cdot (A_k \nabla p_k) - i\sigma p_k\right) + g \quad \text{on } \Gamma_k, \tag{4.32}$$

where $p_k = p|_{K_k}$, $Q \in \mathbb{C}$, $|Q| \leq 1$ and σ is a positive real valued constant on $\cup_{k=1}^N \partial K_k$. For convenience it is denoted $A_k = A|_{K_k}$ and $\eta_k = \eta|_{K_k}$. Note that A_k is either the identity matrix and $\eta_k = 1$ or the element is in the PML.

Provided that $Q = 0$, $\kappa_k \in \mathbb{R}$, $A_k = I$, $g = 0$ and σ is given by (4.9), the exterior boundary condition (4.32) corresponds to the zeroth order (i.e. Sommerfeld type) absorbing boundary condition (4.9).

For the formulation of the UWVF-PML the operator F_k is redefined as

$$F_k : L^2(\partial K_k) \to L^2(\partial K_k) \tag{4.33}$$

such that if $y_k \in L^2(\partial K_k)$ then $F_k(y_k) \in L^2(\partial K_k)$ is given by

$$F_k(y_k) \quad = \quad \left(\frac{1}{\rho_k} n_k \cdot (\overline{A}_k \nabla) - i\sigma\right) v_k \quad \text{on } \partial K_k, \tag{4.34}$$

where $v_k \in H^1(K_k)$ satisfies

$$\nabla \cdot A_k \nabla \overline{v}_k + \kappa_k^2 \eta_k^2 \overline{v}_k = 0, \quad \text{in } K_k, \tag{4.35}$$

$$\left(-\frac{1}{\rho_k} n_k \cdot (\overline{A}_k \nabla) - i\sigma\right) v_k = y_k \text{ on } \partial K_k. \tag{4.36}$$

In addition, the unknown function χ_k on ∂K_k is defined by

$$\chi_k = \Big(\big(-\frac{1}{\rho_k} n_k \cdot (A_k \nabla) - i\sigma\big) p_k\Big)\Big|_{\partial K_k}, \quad 1 \leq k \leq N. \tag{4.37}$$

Using the above definitions, the UWVF for the Helmholtz-PML equation can be written in the same form as for the standard Helmholtz equation (4.17). An exception follows from the source term f_s which gives rise for an additional term in the right hand side of (4.17) which is then

$$\sum_{k=1}^{N}\int_{\Gamma_k}\frac{1}{\sigma}g\overline{F_k(y_k)}+\frac{2i}{\rho_k}\sum_{k=1}^{N}\int_{K_k}f_s\eta_k^2\overline{v}_k. \tag{4.38}$$

In order to discretize (4.13) a plane wave basis is used. For those a set of directions $\{d_{k,\ell}\}_{\ell=1}^{N_k}$ associated with K_k (with $|d_{k,\ell}|=1$) must be defined. Then the plane wave basis functions are

$$\varphi_{k,\ell}=e^{i\overline{\kappa}_k d_{k,\ell}\cdot\overline{r}'}. \tag{4.39}$$

where $\overline{r}'=(\overline{x}',\overline{y}',\overline{z}')$. Note that this special basis is a solution of the adjoint problem (4.3) on K_k when either $A_k=I$ or when the element is in the PML.

The discrete form of the UWVF is obtained via the substitution $v_k=\varphi_{k,\ell}$ and

$$\chi_k^a=\sum_{\ell=1}^{N_k}\Big(\chi_{k,\ell}\big(-\frac{1}{\rho_k}n_k\cdot(A_k\nabla)-i\sigma\big)\varphi_{k,\ell}\Big),\quad 1\le k\le N. \tag{4.40}$$

Analogously to the discrete Helmholtz problem in Section 4.1.1, the weights $\chi_{k,\ell}$ can be computed from the matrix equation (4.28). Due to the source term f_s, the entires of the data vector b are computed as

$$b_k^\ell=\int_{\Gamma_k}\frac{1}{\sigma}g\overline{\Big(\frac{1}{\rho_k}\frac{\partial\varphi_{k,\ell}}{\partial n_k}-i\sigma\varphi_{k,\ell}\Big)}+\frac{2i}{\rho_k}\int_{K_k}f_s\eta_k^2\overline{\varphi}_{k,\ell}. \tag{4.41}$$

4.1.3 Resolving the field from the boundary function χ_k

The discrete UWVF gives an approximation for the function χ_k which consists of the sum of $\partial p/\partial n$ and p on ∂K_k for each k. By using χ_k and χ_j for the common interface $\Sigma_{k,j}$ one can compute an approximation for p on $\Sigma_{k,j}$. However, away from ∂K_k a direct approximation is only given in the elements where $\kappa_k\in\mathbb{R}$. Since elements K_k are typically large compared to wavelength of sound, one needs to compute the field away from ∂K_k when medium is absorbing. This procedure is discussed next.

Let K_k and K_j share a common boundary $\Sigma_{k,j}$ then using the coupled transmission conditions (4.30) and (4.31); and the definition of the function χ_k (4.37), the pressure field on $\Sigma_{k,j}$ can be computed as

$$p|_{\Sigma_{k,j}}=\frac{i}{2\sigma}(\chi_k+\chi_j). \tag{4.42}$$

On the other hand, provided that A_k is identity matrix, $\kappa_k\in\mathbb{R}$ and $r'=r$ in K_k, equations (4.3) and (4.35) are identical and it easily follows from (4.37) and (4.40)

that

$$p^a|_{K_k} = \sum_{\ell=1}^{N_k} \chi_{k,\ell}\varphi_{k,\ell} \quad \text{in } K_k. \tag{4.43}$$

However, in the case of an absorbing medium, the extension of the field into the element requires a new post-processing step. (Note that this is not necessary during the solution of (4.28) but only for obtaining the field away from $\cup_{k=1}^{N}\partial K_k$.)

Analogously to original UWVF discretization (4.37) and (4.39), plane wave solutions are utilized to construct a new set of basis functions. Unlike in the discrete UWVF, however, the plane waves are now solutions of the local Helmholtz equation (4.29) of the form

$$\phi_{k,\ell} = e^{i\kappa_k a_{k,\ell}\cdot r'}. \tag{4.44}$$

Rewriting the impedance equation (4.40) with the new set basis functions gives

$$\psi_k^a = \sum_{\ell=1}^{N_k} \Big(\psi_{k,\ell}\big(-\frac{1}{\rho_k}n_k\cdot(A_k\nabla) - i\sigma\big)\phi_{k,\ell}\Big), \quad 1 \le k \le N. \tag{4.45}$$

To approximate the solution using the new basis, one needs to compute the weights $\psi_{k,\ell}$, $1 \le \ell \le N_k$ for which $\psi_k^a \cong \chi_k^a$.

In the UWVF context, the weights can be easily obtained for each element K_k, $1 \le k \le N$ as a solution of

$$\begin{aligned}
&\sum_{\ell=1}^{N_k}\int_{\partial K_k}\Big(\psi_{k,\ell}\big(-\frac{1}{\rho_k}n_k\cdot(A_k\nabla) - i\sigma\big)\phi_{k,\ell}\Big)\overline{\Big(\big(-\frac{1}{\rho_k}n_k\cdot(\overline{A}_k\nabla) - i\sigma\big)\phi_{k,m}\Big)} \\
&= \sum_{\ell=1}^{N_k}\int_{\partial K_k}\Big(\chi_{k,\ell}\big(-\frac{1}{\rho_k}n_k\cdot(A_k\nabla) - i\sigma\big)\varphi_{k,\ell}\Big)\overline{\Big(\big(-\frac{1}{\rho_k}n_k\cdot(\overline{A}_k\nabla) - i\sigma\big)\phi_{k,m}\Big)},
\end{aligned} \tag{4.46}$$

for all $1 \le m \le N_k$. For each element, the equations (4.46) can be written in the form of matrix equation

$$Y_k = D_k^{-1}(\phi_{k,\ell},\phi_{k,m})D_k(\varphi_{k,\ell},\phi_{k,m})X_k, \tag{4.47}$$

where $X_k = (\chi_{k,1},...,\chi_{k,N_k})^\top$ and $Y_k = (\psi_{k,1},...,\psi_{k,N_k})^\top$. The entries for the matrix D_k are

$$\begin{aligned}
&D_k(\phi_{k,\ell},\phi_{k,m}) = \\
&\int_{\partial K_k}\Big(\big(-\frac{1}{\rho_k}n_k\cdot(A_k\nabla) - i\sigma\big)\phi_{k,\ell}\Big)\overline{\Big(\big(-\frac{1}{\rho_k}n_k\cdot(\overline{A}_k\nabla) - i\sigma\big)\phi_{k,m}\Big)},
\end{aligned} \tag{4.48}$$

where $1 \leq \ell, m \leq N_k$. Note that in the case of $\kappa_k \in \mathbb{R}$ and $r' = r$ in K_k, the term $D_k^{-1}(\phi_{k,\ell}, \phi_{k,m}) D_k(\varphi_{k,\ell}, \phi_{k,m}) = I$ and no post-processing is needed.

After the coefficients $\psi_{k,\ell}$ are found, the approximation for the field in each element is obtained as

$$p^a|_{K_k} = \sum_{\ell=1}^{N_k} \psi_{k,\ell} \phi_{k,\ell} \quad \text{in } K_k. \tag{4.49}$$

4.2 Navier Equation

In this section the UWVF for the elasticity problem is derived. As in the case of the Helmholtz equation, the derivation starts by partitioning the domain Ω into disjoint regular finite elements $K_k,\ k = 1, ..., N$. The mesh must be chosen so that the coefficients Λ, μ and ρ are constant on each element (of course they can be discontinuous across element boundaries). Furthermore, let the domain Ω consist of subdomains Ω_ℓ (i.e. $\overline{\Omega} = \cup_{\ell=1}^{L} \overline{\Omega_\ell}$) in which material properties are constants and assume that the boundaries of the subdomains $\partial\Omega_\ell$ do not intersect any of the elements K_k. In other words, it is required that the subdomain boundaries $\partial\Omega_\ell$ coincide with the element edges ∂K_k.

Unlike for the Helmholtz problem where the coupling parameter σ was a real valued scalar, it is now a positive-definite real valued matrix function of position on $\Sigma_{k,j}$. The elastic transmission conditions on $\Sigma_{k,j}$ from Section 2.4 are written in a coupled form as

$$\begin{aligned} T^{(n_k)}(u_k) + i\sigma u_k &= -T^{(n_j)}(u_j) + i\sigma u_j, \\ T^{(n_k)}(u_k) - i\sigma u_k &= -T^{(n_j)}(u_j) - i\sigma u_j, \end{aligned}$$

where $u_k = u|_{K_k}$ so that

$$\Delta^e u_k + \omega^2 \rho_k u_k = 0 \quad \text{in } K_k. \tag{4.50}$$

The material properties $\rho_k = \rho|_{K_k}$ and $\Lambda|_{K_k}$ and $\mu|_{K_k}$ are used in Δ^e. Obviously the above transmission conditions are equivalent to the original pair (2.30).

Moreover, to be able to write the coupled transmission conditions for the test function, the complex conjugate of the traction operator is defined as

$$\overline{T^{(n)}}(u) = 2\overline{\mu}\,\frac{\partial u}{\partial n} + \overline{\Lambda}\, n \nabla \cdot u + \overline{\mu}\, n \times \nabla \times u, \tag{4.51}$$

where the overline indicates complex conjugation. Thus $\overline{\overline{T^{(n)}}(u)} = T^{(n)}(\overline{u})$. For the following use, suppose $u_k \in (H^1(K_k))^2$ is a solution of Navier equation (4.50) in K_k such that

$$T^{(n_k)}(u_k) - i\sigma u_k \in (L^2(\partial K_k))^2.$$

And let the test function $v_k \in (H^1(K_k))^2$ satisfy

$$\Delta^e \overline{v}_k + \omega^2 \rho_k \overline{v}_k = 0 \quad \text{in } K_k, \tag{4.52}$$

such that

$$\overline{T^{(n_k)}}(v_k) - i\sigma v_k \in (L^2(\partial K_k))^2.$$

The derivation of the UWVF for the Navier equation begins from the equality

$$\begin{aligned}
&\sum_{k=1}^{N} \int_{\partial K_k} \sigma^{-1}(-T^{(n_k)}(u_k) - i\sigma u_k) \cdot \overline{(-\overline{T^{(n_k)}}(v_k) - i\sigma v_k)} \\
= &\sum_{k=1}^{N} \int_{\partial K_k} \sigma^{-1}(T^{(n_k)}(u_k) - i\sigma u_k) \cdot \overline{(\overline{T^{(n_k)}}(v_k) - i\sigma v_k)} \\
&\qquad - \sum_{k=1}^{N} 2i \int_{\partial K_k} \big(u_k \cdot \overline{\overline{T^{(n_k)}}(v_k)} - T^{(n_k)}(u_k) \cdot \overline{v}_k\big).
\end{aligned}$$

The right hand side is only a straightforward expansion of the left hand side.

As noted above $\overline{\overline{T^{(n_k)}}(v_k)} = T^{(n_k)}(\overline{v}_k)$ so that using Betti's third identity [131]

$$\int_{\partial K_k} \big(u_k \cdot T^{(n_k)}(\overline{v}_k) - T^{(n_k)}(u_k) \cdot \overline{v}_k\big) = \int_{K_k} \big(u_k \cdot \Delta^e \overline{v}_k - \overline{v}_k \cdot \Delta^e u_k\big),$$

and the fact that u_k and $\overline{v}_k$ satisfy the Navier equation one obtains

$$\begin{aligned}
\int_{\partial K_k} \big(u_k \cdot T^{(n_k)}(\overline{v}_k) - T^{(n_k)}(u_k) \cdot \overline{v}_k\big) &= \int_{K_k} \big(u_k \cdot \Delta^e \overline{v}_k - \overline{v}_k \cdot \Delta^e u_k\big) \\
&= \omega^2 \rho_k \int_{K_k} (u_k \cdot \overline{v}_k - u_k \cdot \overline{v}_k) = 0.
\end{aligned}$$

Then

$$\begin{aligned}
&\sum_{k=1}^{N} \int_{\partial K_k} \sigma^{-1}(-T^{(n_k)}(u_k) - i\sigma u_k) \cdot \overline{(-\overline{T^{(n_k)}}(v_k) - i\sigma v_k)} \\
= &\sum_{k=1}^{N} \int_{\partial K_k} \sigma^{-1}(T^{(n_k)}(u_k) - i\sigma u_k) \cdot \overline{(\overline{T^{(n_k)}}(v_k) - i\sigma v_k)}. \qquad (4.53)
\end{aligned}$$

By using (4.53) the UWVF scheme is obtained. Suppose the element K_j shares a boundary with element K_k. The transmission conditions (2.30) imply that

$$T^{(n_k)}(u_k) - i\sigma u_k = -T^{(n_j)}(u_j) - i\sigma u_j, \quad \text{on } \Sigma_{k,j}, \qquad (4.54)$$

where it has been taken into account that $n_j = -n_k$ on $\Sigma_{k,j}$. Using the boundary condition

$$T^{(n)}(u) - i\sigma u = Q(-T^{(n)}(u) - i\sigma u) + g \qquad (4.55)$$

on the exterior boundary Γ, the substitution of these into (4.53) yields

$$\begin{aligned}
&\sum_{k=1}^{N}\int_{\partial K_k}\sigma^{-1}\chi_k\cdot\overline{(-\overline{T^{(n_k)}}(v_k)-i\sigma v_k)}\\
-\;&\sum_{k=1}^{N}\sum_{j=1}^{N}\int_{\Sigma_{k,j}}\sigma^{-1}\chi_j\cdot\overline{(\overline{T^{(n_k)}}(v_k)-i\sigma v_k)}\\
-\;&\sum_{k=1}^{N}\int_{\Gamma_k}Q\sigma^{-1}\chi_k\cdot\overline{(\overline{T^{(n_k)}}(v_k)-i\sigma v_k)}=\sum_{k=1}^{N}\int_{\Gamma_k}\sigma^{-1}g\cdot\overline{(\overline{T^{(n_k)}}(v_k)-i\sigma v_k)},
\end{aligned}\tag{4.56}$$

where $\chi_k=-T^{(n_k)}(u_k)-i\sigma u_k$ on ∂K_k.

To clarify the analogy of this variational formulation with the Helmholtz case, it is possible to define the test function $y_k=-\overline{T^{(n_k)}}(v_k)-i\sigma v_k$ on ∂K_k and the operator $F_k:(L^2(\partial K_k))^2\to(L^2(\partial K_k))^2$ by

$$F_k(y_k)=\overline{T^{(n_k)}}(v_k)-i\sigma v_k\tag{4.57}$$

on ∂K_k. Then the above equation gives the UWVF of finding $\chi_k\in(L^2(\partial K_k))^2$, $k=1,2,...,N$ such that

$$\begin{aligned}
&\sum_{k=1}^{N}\int_{\partial K_k}\sigma^{-1}\chi_k\cdot\overline{y_k}-\sum_{k=1}^{N}\sum_{j=1}^{N}\int_{\Sigma_{k,j}}\sigma^{-1}\chi_j\cdot\overline{F_k(y_k)}\\
-\;&\sum_{k=1}^{N}\int_{\Gamma_k}Q\sigma^{-1}\chi_k\cdot\overline{F_k(y_k)}=\sum_{k=1}^{N}\int_{\Gamma_k}\sigma^{-1}g\cdot\overline{F_k(y_k)},
\end{aligned}\tag{4.58}$$

for all $y_k\in(L^2(\partial K_k))^2$, $k=1,2,...,N$. This makes it clear that the unknowns in the UWVF are the functions χ_k on ∂K_k. Of course, once these have been computed it is possible to find u and $T^{(n)}(u)$ on ∂K_k for any k. For example, if K_k and K_j share a common boundary $\Sigma_{k,j}$ then

$$u|_{\Sigma_{k,j}}=\frac{i}{2}\sigma^{-1}(\chi_k+\chi_j)\quad\text{and}\quad T^{(n_k)}(u)=\frac{\chi_j-\chi_k}{2}.\tag{4.59}$$

A similar formula holds on the exterior boundary using the exterior boundary condition.

The details of how to choose σ for each face are given next. For some faces the choice of σ may be dictated by modeling considerations. For most faces it needs to be chosen as a positive definite matrix in a way that helps the conditioning of the linear system resulting from the UWVF. There are many possible choices for the coupling matrix σ. In principle, the only requirement is that entries of σ must be of the order $\omega\rho\,|c|$ where c is, for example, either c_P or c_S. Therefore on the boundary $\Sigma_{k,j}$ one could choose

$$\sigma=\omega\hat{\rho}\,\hat{c}_P I,\tag{4.60}$$

where $\hat{\rho}$ and $\hat{c}_P$ are mean values of ρ and $|c_P|$, respectively, across the boundary and I is the identity matrix. On the external boundaries $\hat{\rho}$ and $\hat{c}_P$ can be replaced with ρ and c_P, respectively.

Another possibility, more in accordance with the original philosophy of the UWVF, is to utilize the absorbing boundary condition derived in Section 3.1. Again, on the internal boundaries the coupling parameter is written by means of the mean values of the moduli of the appropriate quantities if the coefficients are complex.

$$\sigma = \omega\hat{\rho}(\hat{c}_P n \otimes n + \hat{c}_S s \otimes s). \tag{4.61}$$

On the exterior boundary this form reduces to (3.13) and the boundary condition equals to the absorbing boundary condition (3.12). This is the choice used in the numerical experiments later in this thesis.

4.2.1 Discretization of the elastic UWVF

In this section it will be shown how to discretize the UWVF developed in the previous section. The discrete form is given for 2D problems. Clearly in that case $(L^2(\partial K_k))^2$, $1 \leq k \leq N$ needs to be discretized. As noted earlier in Section 4.1.1, the discretization should make it possible to compute the operator F_k defined in (4.57) easily. As in the case of the Helmholtz problem this leads to the use of a plane wave expansion.

On each element the solution of the adjoint Navier equation (4.52) can be separated into two components using the Helmholtz decomposition

$$v_k = v_k^P + v_k^S,$$

which satisfy $\nabla \times v_k^P = 0$ and $\nabla \cdot v_k^P = 0$. In a homogeneous medium (i.e. on any Ω_j, $j = 1, \ldots, J$ and hence on any element K_k) the compressional (P) wave v_k^P and shear (S) wave v_k^S satisfy the Helmholtz equations

$$\Delta\overline{v_k^P} + \kappa_P^2\overline{v_k^P} = 0, \tag{4.62}$$

$$\Delta\overline{v_k^S} + \kappa_S^2\overline{v_k^S} = 0, \tag{4.63}$$

in K_k with the wave numbers $\kappa_P = \omega/c_P$ and $\kappa_S = \omega/c_S$. The corresponding wave velocities c_P and c_S are functions of the Lame constants μ, Λ and the density ρ on K_k and are given by (2.12). Recall from Section 2.2 that these two component waves propagate independently in the homogeneous medium in K_k but interact on the medium interfaces.

Hence, the function χ_k is approximated using two sets of plane waves with the wave numbers κ_P and κ_S

$$\begin{aligned}\chi_k \approx & \sum_{\ell=1}^{N_k^P}\left[\chi_{k,\ell}^P\left(-T^{(n_k)}(v_{k,\ell}^P) - i\sigma v_{k,\ell}^P\right)\right] \\ & + \sum_{\ell=1}^{N_k^S}\left[\chi_{k,\ell}^S\left(-T^{(n_k)}(v_{k,\ell}^S) - i\sigma v_{k,\ell}^S\right)\right],\end{aligned} \tag{4.64}$$

where

$$v^P_{k,\ell} = \begin{cases} d_{k,\ell} \exp(i\overline{\kappa}_P d_{k,\ell} \cdot r) & \text{in } K_k \\ 0 & \text{elsewhere} \end{cases} \tag{4.65}$$

$$v^S_{k,\ell} = \begin{cases} d^{\perp}_{k,\ell} \exp(i\overline{\kappa}_S d_{k,\ell} \cdot r) & \text{in } K_k \\ 0 & \text{elsewhere} \end{cases}, \tag{4.66}$$

and where $d_{k,\ell} = (d^1_{k,\ell}, d^2_{k,\ell})$, $\quad |d_{k,\ell}| = 1$ and $d^{\perp}_{k,\ell} = (-d^2_{k,\ell}, d^1_{k,\ell})$.

As advocated in previous studies of the Helmholtz problem, in equation (4.23) equispaced directions on the unit circle are used in 2D examples (note that in this thesis, the numerical studies for the Navier problem are limited to 2D)

$$d_{k,\ell} = \left(\cos\left(2\pi \frac{\ell - 1}{q} \right), \sin\left(2\pi \frac{\ell - 1}{q} \right) \right), \quad 1 \le \ell \le q, \tag{4.67}$$

where q is the number of directions (i.e. $q = N^S_k$ or $q = N^P_k$).

For $k = 1, \ldots, N$, let

$$\begin{aligned} V_{h,k} \;=\; & \operatorname{span}\Big\{ \overline{T^{(n_k)}}(v^S_{k,\ell}) + i\sigma v^S_{k,\ell},\ 1 \le \ell \le N^S_k, \\ & \overline{T^{(n_k)}}(v^P_{k,\ell}) + i\sigma v^P_{k,\ell},\ 1 \le \ell \le N^P_k \Big\}. \end{aligned} \tag{4.68}$$

Then the discrete UWVF problem is to compute $\chi_{h,k} \in V_{h,k}$, $k = 1, 2, ..., N$, such that

$$\begin{aligned} & \sum_{k=1}^{N} \int_{\partial K_k} \sigma^{-1} \chi_{h,k} \cdot \overline{y_{h,k}} - \sum_{k=1}^{N} \sum_{j=1}^{N} \int_{\Sigma_{k,j}} \sigma^{-1} \chi_{h,j} \cdot \overline{F_k(y_{h,k})} \\ - \; & \sum_{k=1}^{N} \int_{\Gamma_k} Q\sigma^{-1} \chi_{h,k} \cdot \overline{F_k(y_{h,k})} = \sum_{k=1}^{N} \int_{\Gamma_k} \sigma^{-1} g \cdot \overline{F_k(y_{h,k})}, \end{aligned} \tag{4.69}$$

for all $y_{h,k} \in V_{h,k}$, $k = 1, 2, ..., N$.

To obtain a discrete matrix problem corresponding to (4.69), one can choose $y_k = v^P_{k,\ell}$ and $y_k = v^S_{k,\ell}$ for each k and ℓ. Substituting these into (4.56), the discrete elastic UWVF problem can be written in the form of matrix equation (4.28) where

$$X = (\chi^P_{1,1}, \ldots, \chi^P_{1,N^P_1}, \chi^S_{1,1} \ldots, \chi^S_{1,N^S_1}, \ldots)^{\top}.$$

The matrix D is again a block-diagonal matrix. Now each block D^k consists of four subblocks

$$D_k = \begin{pmatrix} D^1_k & D^2_k \\ D^3_k & D^4_k \end{pmatrix}$$

with the elements

$$D_k^{1,\ell,m} = \int_{\partial K_k} \sigma^{-1}\big(-T^{(n_k)}(v_{k,m}^P) - i\sigma v_{k,m}^P\big)\cdot\overline{\big(-\overline{T^{(n_k)}}(v_{k,\ell}^P) - i\sigma v_{k,\ell}^P\big)}$$

$$D_k^{2,\ell,m} = \int_{\partial K_k} \sigma^{-1}\big(-\overline{T^{(n_k)}}(v_{k,m}^S) - i\sigma v_{k,m}^S\big)\cdot\overline{\big(-\overline{T^{(n_k)}}(v_{k,\ell}^P) - i\sigma v_{k,\ell}^P\big)}$$

$$D_k^{3,\ell,m} = \int_{\partial K_k} \sigma^{-1}\big(-\overline{T^{(n_k)}}(v_{k,m}^P) - i\sigma v_{k,m}^P\big)\cdot\overline{\big(-\overline{T^{(n_k)}}(v_{k,\ell}^S) - i\sigma v_{k,\ell}^S\big)}$$

$$D_k^{4,\ell,m} = \int_{\partial K_k} \sigma^{-1}\big(-T^{(n_k)}(v_{k,m}^S) - i\sigma v_{k,m}^S\big)\cdot\overline{\big(-\overline{T^{(n_k)}}(v_{k,\ell}^S) - i\sigma v_{k,\ell}^S\big)}.$$

The matrix C is also a block matrix with the blocks on diagonal

$$C_k = \begin{pmatrix} C_k^1 & C_k^2 \\ C_k^3 & C_k^4 \end{pmatrix},$$

and off diagonal

$$C_{k,j} = \begin{pmatrix} C_{k,j}^1 & C_{k,j}^2 \\ C_{k,j}^3 & C_{k,j}^4 \end{pmatrix}.$$

The elements of the blocks are

$$C_k^{1,\ell,m} = \int_{\Gamma_k} Q\sigma^{-1}\big(-T^{(n_k)}(v_{k,m}^P) - i\sigma v_{k,m}^P\big)\cdot\overline{\big(\overline{T^{(n_k)}}(v_{k,\ell}^P) - i\sigma v_{k,\ell}^P\big)}$$

$$C_k^{2,\ell,m} = \int_{\Gamma_k} Q\sigma^{-1}\big(-T^{(n_k)}(v_{k,m}^S) - i\sigma v_{k,m}^S\big)\cdot\overline{\big(\overline{T^{(n_k)}}(v_{k,\ell}^P) - i\sigma v_{k,\ell}^P\big)}$$

$$C_k^{3,\ell,m} = \int_{\Gamma_k} Q\sigma^{-1}\big(-T^{(n_k)}(v_{k,m}^P) - i\sigma v_{k,m}^P\big)\cdot\overline{\big(\overline{T^{(n_k)}}(v_{k,\ell}^S) - i\sigma v_{k,\ell}^S\big)}$$

$$C_k^{4,\ell,m} = \int_{\Gamma_k} Q\sigma^{-1}\big(-T^{(n_k)}(v_{k,m}^S) - i\sigma v_{k,m}^S\big)\cdot\overline{\big(\overline{T^{(n_k)}}(v_{k,\ell}^S) - i\sigma v_{k,\ell}^S\big)}$$

and

$$C_{k,j}^{1,\ell,m} = \int_{\Sigma_{k,j}} \sigma^{-1}\big(T^{(n_k)}(v_{j,m}^P) - i\sigma v_{j,m}^P\big)\cdot\overline{\big(\overline{T^{(n_k)}}(v_{k,\ell}^P) - i\sigma v_{k,\ell}^P\big)}$$

$$C_{k,j}^{2,\ell,m} = \int_{\Sigma_{k,j}} \sigma^{-1}\big(T^{(n_k)}(v_{j,m}^S) - i\sigma v_{j,m}^S\big)\cdot\overline{\big(\overline{T^{(n_k)}}(v_{k,\ell}^P) - i\sigma v_{k,\ell}^P\big)}$$

$$C_{k,j}^{3,\ell,m} = \int_{\Sigma_{k,j}} \sigma^{-1}\big(T^{(n_k)}(v_{j,m}^P) - i\sigma v_{j,m}^P\big)\cdot\overline{\big(\overline{T^{(n_k)}}(v_{k,\ell}^S) - i\sigma v_{k,\ell}^S\big)}$$

$$C_{k,j}^{4,\ell,m} = \int_{\Sigma_{k,j}} \sigma^{-1}\big(T^{(n_k)}(v_{j,m}^S) - i\sigma v_{j,m}^S\big)\cdot\overline{\big(\overline{T^{(n_k)}}(v_{k,\ell}^S) - i\sigma v_{k,\ell}^S\big)}.$$

The entries of the matrices C and D can be computed exactly since they only involve integrals of complex exponentials along lines in 2D and over triangular faces in 3D.

After the vector X is computed, the solution χ_k on ∂K_k can be approximated using (4.64) and the traction and displacement approximated by using (4.59).

Chapter V

Computational issues

Earlier studies of the UWVF have reported ill-conditioning of the resulting matrix system as a major drawback of the method [29, 30]. It can be shown that the conditioning of the UWVF matrices is dependent on the element size of the finite element mesh, material properties of the medium and the choice of basis functions used to approximate the solution. In particular, varying the wave number within the computational domain, an uneven element size of the mesh or a homogeneous collection of plane wave basis functions in all elements can lead to severe instability. Since the material properties are defined by the problem at hand, the stability can be improved by adjusting the mesh and the UWVF basis functions properly.

This chapter deals with practical aspects of the numerical procedures for the UWVF of the Helmholtz and Navier problems. In the first section a method to stabilize the UWVF is introduced and two iterative solvers for solving the matrix equation (4.28) are presented. The conditioning of the UWVF on a fixed mesh can be improved by element wise control of the basis functions. Namely, the basis functions can be chosen dynamically during the building of the system matrices. Since the types of the basis functions used in this study are limited to equispaced plane waves, the adjustable parameter is the number of plane waves per element.

The Richardson iterative method has been used in previous UWVF studies to solve (4.28). However, the stabilized bi-conjugate gradient (Bi-CGStab) method is also considered here. These two methods are compared for the UWVF problem.

To test the proposed techniques in practice, two dimensional numerical experiments for the Helmholtz and Navier problems are presented. In particular, the conditioning of the problem and the performance of the iterative solvers are studied. The new method for choosing the basis functions is first tested for the Helmholtz problem and then applied to the Navier problem. The latter requires additional modifications since the solution in each element is approximated using two independent sets of basis functions. The UWVF scheme for the Navier problem is also compared with the piecewise linear FEM discussed in Section 3.2.2.

5.1 Computational procedure

After the finite element mesh for the problem geometry is generated, the solution of the UWVF problem can be carried out in three steps. First, the matrix D is computed. Although it is possible to fix the number of functions in the basis on each element beforehand, changes in the number of basis functions per element are allowed during the building of the matrix. The correct choice of the number of basis functions on each element reduces the severity of the stability problems that were reported in [30]. When the matrix D is computed, it can be Cholesky or LU factorized for later use in solving the matrix equation (4.28).

In the second step, after the number of functions in the basis on each element is chosen, the matrix C can be computed. In the third step, the matrix system (4.28) is solved using an appropriate direct or iterative matrix solver. The last step is rather time consuming. Therefore, the choice of the solver is an important issue.

5.1.1 Stability of the UWVF problem

The block diagonal structure of the matrix D allows the separate factorization the blocks D_k. The conditioning of the matrix block D_k depends on a variety of factors, for example on the element size h_k and the number of basis functions N_k in that element. It was shown in [30] that the condition number of D_k for $N_k \geq 4$ is bounded from below by $Ch_k^{-2\text{int}(N_k/2)+2}$ where C is a positive constant and $\text{int}(a)$ refers to the integer part of a. Numerical simulations show that the conditioning of the matrix block D_k also depends on the wave number κ_k.

Obviously, the condition number of the matrix D can be affected by controlling the element size h_k and the number of basis functions N_k in each element K_k, $k = 1, ..., N$. These parameters should be chosen so that stable inversion for all blocks D_k is possible. Although one could vary the element size during mesh generation, the focus in this thesis is given on controlling the number of bases for a fixed mesh. This approach is justified because in many applications it is desirable to solve the problem with many wave numbers using the same mesh. On the other hand, it is known from the least-squares method that the easiest way to improve the accuracy is to use more basis functions rather than a finer mesh, provided that the solution to be computed is smooth [152]. Motivated by those considerations, the maximum allowed element size in the UWVF that leads to a tolerable accuracy is investigated. The main difficulty in the use of large elements is the need for a high dimensional local basis which causes ill-conditioning of the blocks D_k for other elements if the high number of basis functions per element is used uniformly regardless of element size.

5.1.2 Choosing the basis

The simplest possibility is to use a fixed number of basis functions (i.e. a fixed number of directions for the plane waves) in all elements. However, due to the variability in the wave number and element size within the computation domain, this may result in severely ill-conditioned blocks leading to a poor approximation.

Therefore, a scheme in which the number of basis functions per element is chosen dynamically during computation of the matrix D is proposed.

An appropriate criterion to characterize the stability of the inversion is the L_1-condition number

$$\mathrm{Cond}(D_k) = \|D_k\|_1 \|D_k^{-1}\|_1. \tag{5.1}$$

The method used here is based on the sequential computation of the blocks D_k and the estimation of the condition number. The procedure starts by fixing the highest allowed condition number and setting the initial number of functions in the basis on each element. Then, it proceeds element by element building the block and estimating the condition number for the current basis. Depending on the condition number, one can reduce or increase the number of functions in the local basis, recompute the block and estimate again the condition number. When the appropriate number of functions in the basis for the element is found, the Cholesky factorized block is saved and the same procedure is repeated for the next element. As the outcome the Cholesky factorized matrix D and the number of basis functions for each element are obtained.

Different criteria can be used to choose the admissible number of basis functions. For example, one can choose the highest dimensional basis for which the condition number is below a predetermined limit. Alternatively, an initial guess can be made of the number of directions giving a relatively large dimensional uniform basis which is known to generate ill-conditioned blocks. The dimension can be reduced only for the elements with the worst conditioning. Computation time is naturally dependent on the method and the initial guess for the basis. However, the basis is independent of the boundary data and therefore for a single frequency and mesh, it must be computed only once.

5.1.3 Iterative algorithms

The solution of problem (4.28) can be done using a variety of techniques. Due to the large size of the problem, the use of an iterative solver is preferred. In [30] the Richardson algorithm was used. The following is a pseudo code for the method.

Set $\epsilon > 0$
$\beta_0 = \mathrm{rand}(0.5; 1-\epsilon)$
$\hat{b} = D^{-1}b$
$X_0 = \beta_0 \hat{b}$
for $j = 1, 2, 3, \ldots$
    $X_j = \beta_{j-1}\hat{b} + [(1-\beta_{j-1})I + \beta_{j-1}D^{-1}C]X_{j-1}$
    if X_j accurate enough; quit;
    $\beta_j = \mathrm{rand}(0.5; 1-\epsilon)$
end

Here rand(a,b) denotes a uniformly distributed random number between a and b. The behavior of the method for the UWVF problem is analyzed in detail in

[29, 30].

In this thesis the Richardson scheme is compared with another iterative solver, namely the stabilized Bi-Conjugate Gradient (Bi-CGStab) [193]. This variant of the conjugate gradient has been shown to be an efficient and smoothly convergent method for solving high dimensional linear systems, see e.g. [182, 193, 195]. It is applicable to non-Hermitian matrices as encountered here (although the reduction of the residual will not necessarily be monotone). The algorithm below describes steps in the Bi-CGStab for the system (4.28).

X_0 is an initial guess; $r_0 = D^{-1}b - (I - D^{-1}C)X_0$
$\hat{r}_0 = r_0$;
$\rho_0 = \alpha = \omega_0 = 1$;
$v_0 = p_0 = 0$;
for $j = 1, 2, 3, \ldots$
    $\rho_j = (\hat{r}_0, r_{j-1})$; $\beta = (\rho_j/\rho_{j-1})(\alpha/\omega_{j-1})$;
    $p_j = r_{j-1} + \beta(p_{j-1} - \omega_{j-1}v_{j-1})$;
    $v_j = (I - D^{-1}C)p_j$;
    $\alpha = \rho_j/(\hat{r}_0, v_j)$;
    $s = r_{j-1} - \alpha v_j$;
    $t = (I - D^{-1}C)s$;
    $\omega_j = (t, s)/(t, t)$;
    $X_j = X_{j-1} + \alpha p_j + \omega_j s$;
    $r_j = s - \omega_j t$;
    if X_j accurate enough; quit;
end

From the computational point of view it must be noted that the Bi-CGStab requires two multiplications by $I - D^{-1}C$ and four vector inner products on each iteration. Only one corresponding matrix-vector multiplication is needed in the Richardson algorithm.

5.2 Numerical examples for 2D Helmholtz problem

In this section the accuracy of the UWVF method for an acoustic transmission problem is analyzed. As an example of the Helmholtz problem in an inhomogeneous medium consider acoustic scattering from the obstacle Ω_1 with different properties than those in the surrounding medium Ω_2. The concentric circular domains Ω_1 and Ω_2 have radii $a = 5.0$ cm and $R = 10$ cm, respectively, see Fig. 5.1. The aim is to assess the behavior of the error of the UWVF approximation rather than to simulate any particular physical problem. The simple geometry allows the computation of an accurate approximation for the problem (4.1) and (4.2) using truncated Fourier series.

The acoustic pressure in $\Omega_1 \cup \Omega_2$ is now denoted by p. Let the speed of sound be $c_1 = 3000$ m/s and $c_2 = 1500$ m/s in Ω_1 and in Ω_2, respectively. The corresponding densities are $\rho_1 = 2000$ kg/m^3 and $\rho_2 = 1000$ kg/m^3. The wave numbers are now

Table 5.1: The comparison of uniform and non-uniform basis for $f = 250$ kHz.

	N_k	Relative Error	Max(Cond(D_k))	DOF
Uniform basis	21	0.1349	$5.3 \cdot 10^{11}$	7014
Non-uniform basis	11...29	0.1260	$1.0 \cdot 10^{4}$	6956

$\kappa_1 = 2\pi f/c_1$ and $\kappa_2 = 2\pi f/c_2$ where f is the frequency of the sound field. The values for the physical parameters c and ρ are typical for biological tissues.

On the exterior boundary Γ the boundary condition is written as

$$\frac{1}{\rho_2}\frac{\partial p_2}{\partial n} - i\kappa_2 p_2 \quad = \quad \frac{1}{\rho_2}\frac{\partial p^{\text{in}}}{\partial n} - i\kappa_2 p^{\text{in}}, \tag{5.2}$$

where p^{in} is the incident wave. The boundary condition (5.2) is obtained from the general form (4.2) by choosing $Q = 0$, $\sigma = \kappa_2$, and

$$g = \frac{1}{\rho_2}\frac{\partial p^{\text{in}}}{\partial n} - i\kappa_2 p^{\text{in}} \quad \text{on } \Gamma. \tag{5.3}$$

As the incident field we use a point source

$$p^{\text{in}} = \frac{i}{4} H_0^{(1)}(\kappa_2 |r - r_0|) \tag{5.4}$$

located at r_0 which is 1.0 cm outside the exterior boundary. The function $H_0^{(1)}$ is the zeroth order Hankel function of the first kind. In many physical problems the sound source can be constructed as a sum of point sources.

The boundary condition (5.2) is the low order absorbing boundary condition (3.2) for the scattered part of the pressure field p. Although there are more accurate absorbing boundary conditions, this is chosen due to simplicity of derivation of the exact solution for the problem which enables comparison with numerical results, see Appendix I. The error analysis compares the UWVF approximation to the exact series solution of (4.1)- (4.2) with the above choice of data.

To increase accuracy of the solution, the elements are allowed to have curved edges on the boundaries $\Omega_1 \cap \Omega_2$ and Γ. The integrals (4.25)-(4.27) on those boundaries were computed with the 21 point Gauss-Legendre quadrature [171].

The analytical solution and two UWVF approximations of the problem for the frequency $f = 250$ kHz are shown in Fig. 5.2. The UWVF approximations are computed in the mesh of Fig. 5.1.

The effect of variability of the element size and the wave number on the conditioning of the matrix blocks D_k is shown in Fig. 5.3. The uniform basis leads to severe conditioning problems in the domain Ω_1 in which the wave number is low. The highest values are in the smallest elements. However, for the non-uniform number of functions in the basis per element, the condition numbers stays low and still the method reaches the same accuracy with an almost equal number of degrees

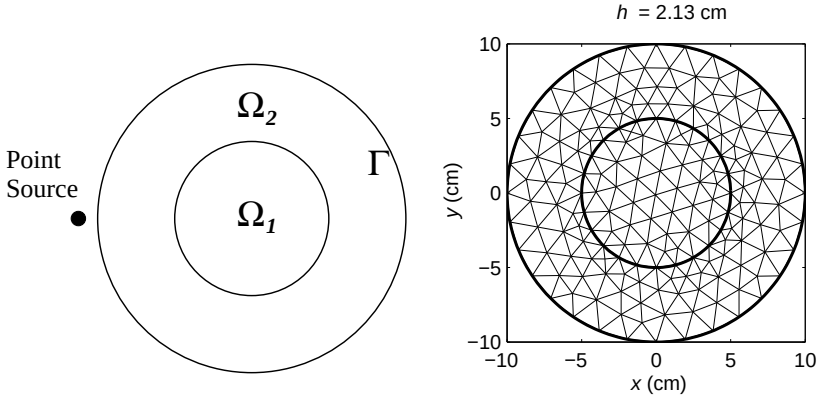

Figure 5.1: The geometry of the model problem (left).One of the meshes used in the computations consisting of 334 elements and 184 vertices (right).

of freedom. The condition number of the blocks D_k in this example is limited to 10^4. In Table 5.1, the accuracy and the condition numbers for the problem are compared with uniform and non-uniform basis.

Preconditioning and performance of the iterative solvers

The simulations in the previous section show that the appropriate choice of the basis can improve the stability of the inversion of the blocks D_k. To determine stability of the full matrix equation (4.28) one needs to study the conditioning of the operator $I - D^{-1}C$. The L_1-condition numbers for D_k, $D - C$ and $I - D^{-1}C$ for the frequency $f = 100$ kHz are presented in Fig. 5.4.

The results suggest that the maximum condition number of D_k characterizes the conditioning of the operator $I - D^{-1}C$. Also, note the superiority of the form $I - D^{-1}C$ compared to the non-preconditioned equation $D - C$.

The convergence of the iterative solvers is studied by observing the norms

$$\text{Residual} = \frac{\|D^{-1}b - (I - D^{-1}C)X\|_2}{\|D^{-1}b\|_2}, \tag{5.5}$$

$$\text{Change in } X_j = \frac{\|X_j - X_{j-1}\|_2}{\|X_j\|_2}. \tag{5.6}$$

The residual is computed in the Bi-CGStab as $\|r_j\|_2/\|D^{-1}b\|_2$. The iterations are terminated when the residual get below 10^{-6}.

The iterative solvers are compared by counting the matrix-vector multiplications $y = (I - D^{-1}C)x = x - D^{-1}Cx$ needed to achieve the termination criterion. Note that in addition to the matrix-vector operations four vector inner products

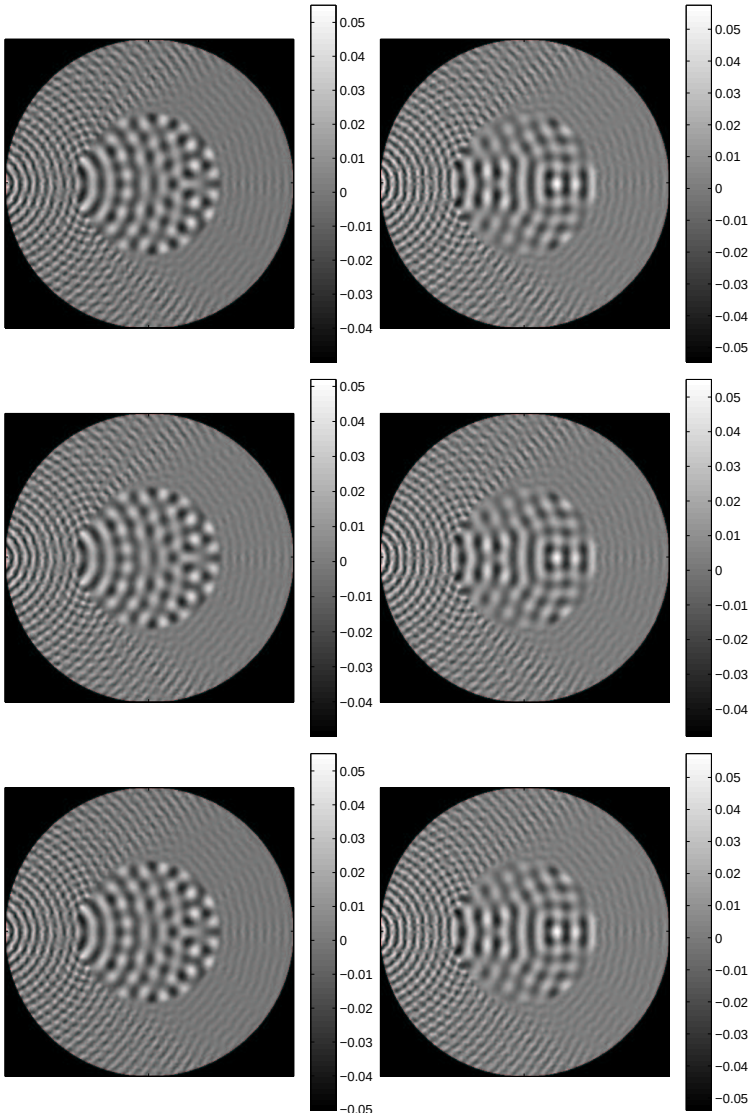

Figure 5.2: Top: The analytical solution of the problem with $f = 250$ kHz. Middle: The UWVF approximation using the uniform basis with $N_k = 21$. Bottom: The UWVF approximation using the non-uniform basis with $N_k = 11, \ldots, 29$. The real parts are shown in the left column and the imaginary parts are in the right column. The UWVF approximations are computed using the mesh with $h_{\max} = 2.13$ cm, see Fig. 5.1.

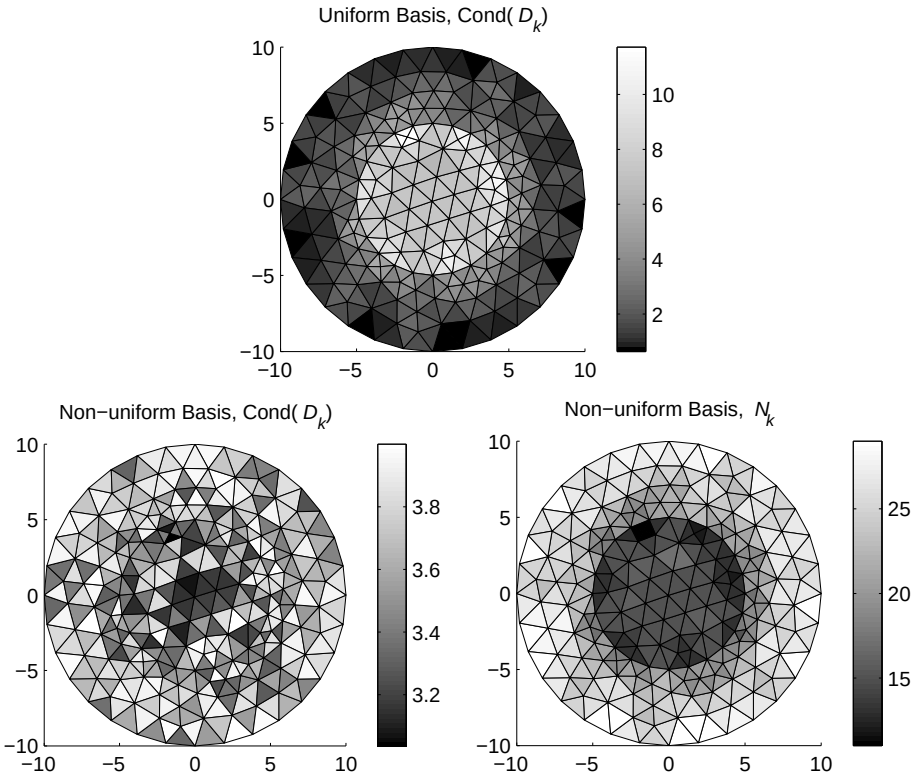

Figure 5.3: Top: Color of an element represents the base 10 logarithm of the condition number of the matrix block D_k corresponding to the case of the uniform basis with $N_k = 21$ and $f = 250$ kHz. The condition number is high in the domain of the lower wave number and especially in the small elements. To improve the stability of the problem the number of plane wave directions is chosen so that the condition number of the blocks D_k are limited below 10^4. Bottom left: Base 10 logarithms of the condition numbers are shown for the non-uniform basis. Bottom right: The highest number of bases for each element K_k for which the condition number of D_k is below 10^4. The condition numbers for the elements are now between 10^3 and 10^4 while the number of basis functions per element varies from 11 to 29.

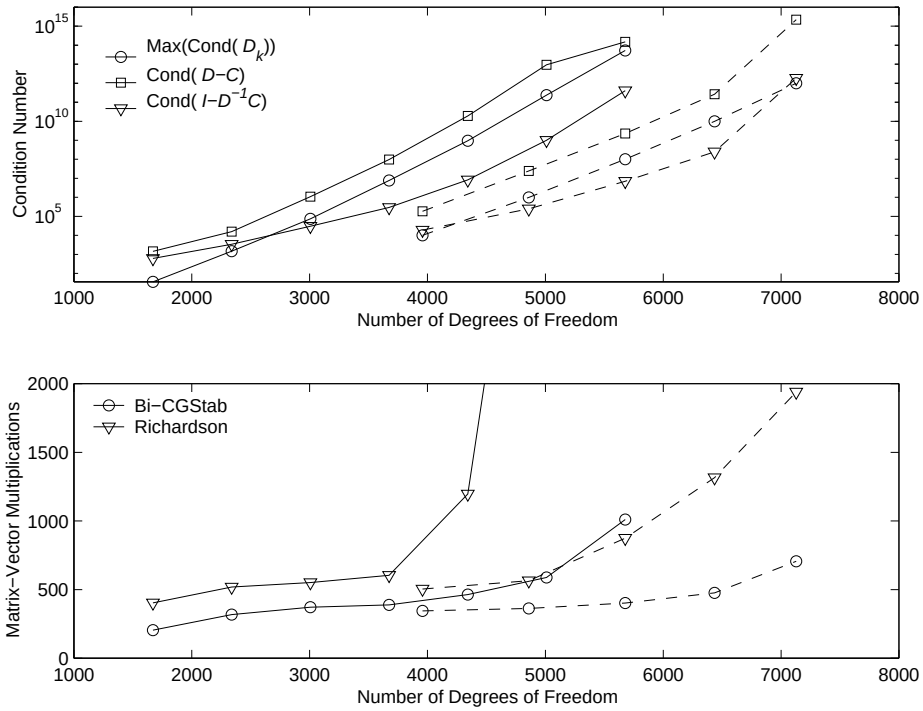

Figure 5.4: Top: The conditioning of the UWVF matrices in the case of uniform basis (solid lines) and non-uniform basis (dashed line) plotted against the number of degrees of freedom for $f = 100$kHz and $h = 2.13$ cm. Bottom: The number of matrix-vector multiplications required to reach the termination criterion.

Table 5.2: A summary of the simulations of Fig. 5.5

	Uniform basis		Non-uniform basis	
N_k	11	15	9..19	15...27
DOF	3674	5010	4859	7128
Max(Cond(D_k))	$7.7 \cdot 10^6$	$2.3 \cdot 10^{11}$	$9.9 \cdot 10^5$	$9.9 \cdot 10^{11}$
Cond($D - C$)	$9.7 \cdot 10^7$	$9.3 \cdot 10^{12}$	$2.4 \cdot 10^7$	$2.2 \cdot 10^{15}$
Cond($I - D^{-1}C$)	$2.9 \cdot 10^5$	$9.9 \cdot 10^8$	$2.5 \cdot 10^5$	$1.8 \cdot 10^{12}$
Mat.- Vec. op., Bi-CGStab	388	588	362	706
Mat.- Vec. op., Richardson	604	Stagnation	565	1939
Relative error	$4.63 \cdot 10^{-2}$	$2.07 \cdot 10^{-3}$	$3.13 \cdot 10^{-3}$	$4.05 \cdot 10^{-5}$

are needed in the Bi-CGStab. However, the computational effort required for the inner products is only a fraction compared to the matrix-vector operation.

The Bi-CGStab converges faster than the Richardson algorithm, see Fig. 5.4. The Bi-CGStab also reached the stopping criterion in all cases whereas the Richardson stagnated in the case of the largest dimensional uniform basis.

The residuals as a function of the iteration number for some simulations are presented in Fig. 5.5. In the same problem the Richardson algorithm failed to reach the termination criterion. Table 5.2 summarizes the simulations of Fig. 5.5. In all examples the convergence of the Richardson algorithm was smoother than that of the Bi-CGStab.

5.3 Navier problem in 2D

In comparison to the Helmholtz problem, the solution of the Navier equation has several additional challenges. Most importantly, the displacement field in each subdomain with a homogeneous medium consists of the linearly independent components, i.e. the P- and S-waves, both of which need to be taken into account in discretization. In the finite element method this causes a particularly fine mesh density since the rule of thumb ($\lambda/h \approx 10$) must hold for the shorter wavelength of the two waves. The UWVF offers a possible advantage over the FEM due to the separate discretization of the P- and S-waves. However, as in the case of the Helmholtz problem, conditioning of the linear system can be a limiting factor in the UWVF simulations. In the following sections, the idea of using the condition number of D_k as an indicator for the overall stability of the problem is extended to the Navier problem. First, the method is examined for two wave propagation problems. This includes a comparison with a low order finite element method of Section 3.2.2. Then the UWVF is applied to an elastic wave problem in an inhomogeneous medium.

5.3.1 Plane and Rayleigh wave propagation

As the first example, elastic wave propagation in a rectangular domain $\Omega = [0, 1] \times [0, 1]$ is investigated. Elastic properties of medium occupying the domain Ω are

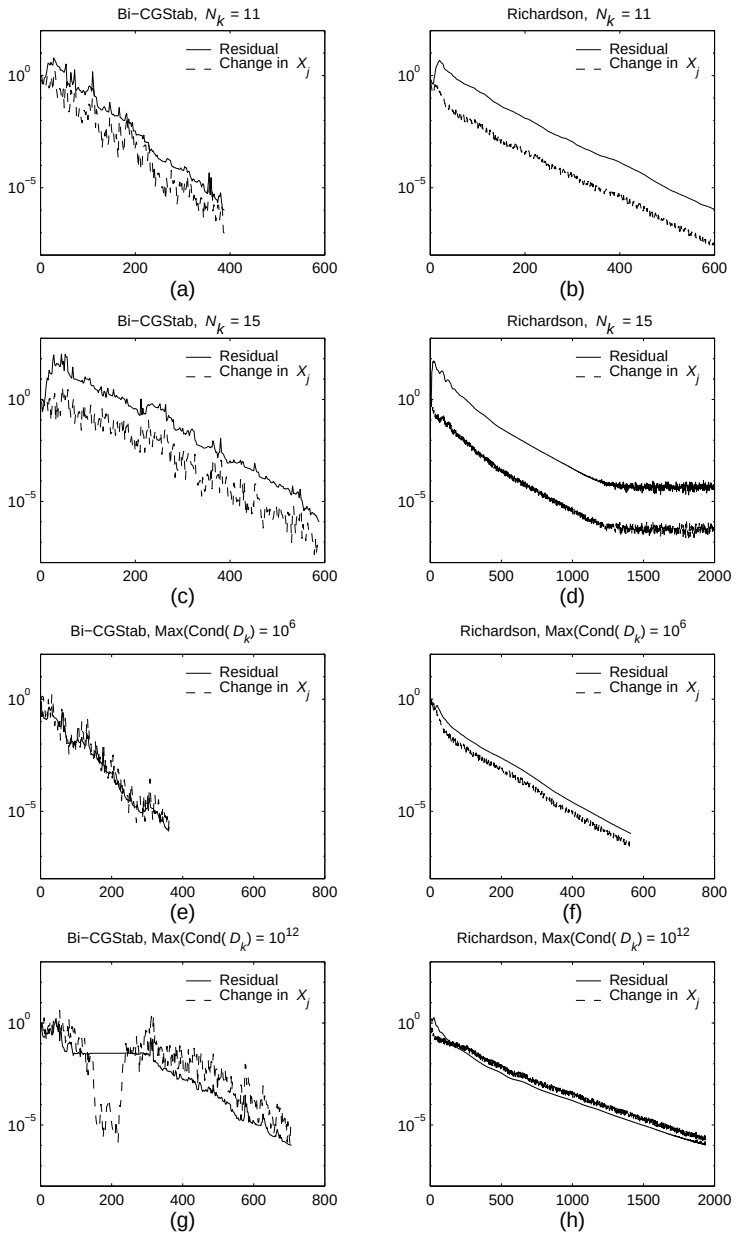

Figure 5.5: Convergence of the iterative solvers for $f = 100$ kHz and $h = 2.13$ cm. The norms for the Bi-CGStab are in the left column and for the Richardson in the right column. We present the residuals for the uniform basis with $N_k = 11$ (a)-(b) and with $N_k = 15$ (c)-(d). Convergence with the non-uniform basis is shown when the condition number of D_k is limited to 10^6 (e)-(f) and 10^{12} (g)-(h).

$E = 200 \cdot 10^9$, $\nu = 0.3$ and $\rho = 7800$. Hence P-, S- and Rayleigh wave speeds are $c_P = 5875$, $c_S = 3140$ and $c_R = 2913$, respectively. This gives ratios $c_P/c_S = \kappa_S/\kappa_P = 1.87$ and $c_P/c_R = \kappa_R/\kappa_P = 2.02$. Single frequency examples for this first model problem are computed with $f = 2.0 \cdot 10^4$ which corresponds to $\kappa_P = 21.4$. The material parameters are similar as those of steel but the examples are not motivated by any particular application. However, the ratio c_P/c_S is typical for a wide range of solid materials.

Two clearly distinct incident fields are analysed. In the first case, the exact solution is a plane wave consisting of both P- and S-waves

$$u^{\text{in}} = \alpha d \exp(i\kappa_P d \cdot r) + \beta d^{\perp} \exp(i\kappa_S d \cdot r). \tag{5.7}$$

The directions d and $d^{\perp}$ are chosen so that $\alpha, \beta \in \mathbb{R}$ and $d \cdot d^{\perp} = 0$. This example is chosen because it provides the simplest test problem to test the accuracy of the elastic UWVF for wave propagation. The direction of propagation of the plane wave in all cases is $d = (\cos(\pi/\tilde{q}), \sin(\pi/\tilde{q}))^{\top}$ where $\tilde{q} = \max(N_k^P, N_k^S)$. This choice does not coincide with any of the directions of the plane wave basis functions $d_{k,\ell}$. Furthermore, the amplitudes of the incident waves in all examples are $\alpha = 1$ and $\beta = 1$.

In the second case, the incident field is the Rayleigh wave of the form (2.36). The waves propagate along the $y = 0$ surface in the direction of the positive x-axis. This example is important since the discrete UWVF method uses only P- and S-plane waves. It is therefore vital to investigate whether the method can resolve surface waves for which the decomposition into P- and S- waves is not immediate. The Rayleigh wave solution near the free-surface is shown in Fig. 5.6.

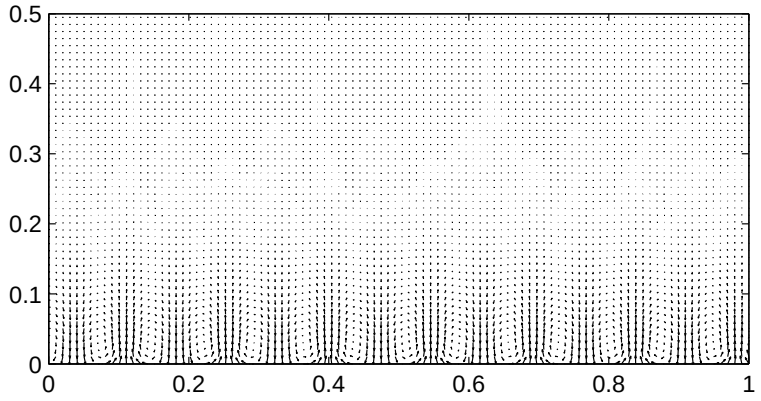

Figure 5.6: The exact solution of the Rayleigh wave problem in the neighborhood of the free surface.

The source term for both, plane and Rayleigh waves, is given in the form

$$g = (1 + Q)T^{(n)}(u^{\text{in}}) - i\sigma(1 - Q)u^{\text{in}} \quad \text{on } \Gamma.$$

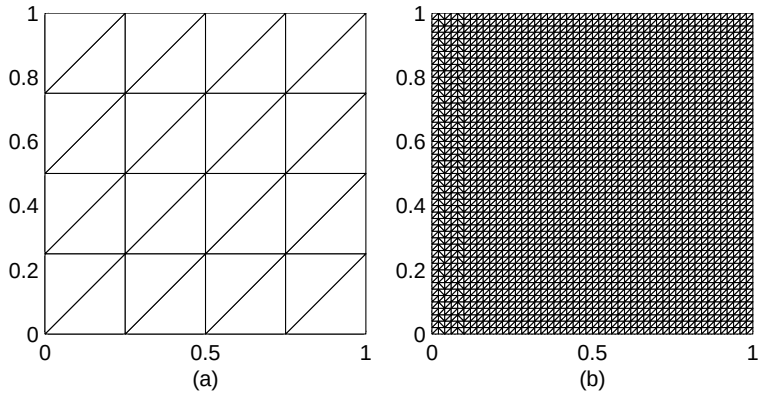

Figure 5.7: Left: A typical uniform mesh used in UWVF simulations. Right: A mesh for the FEM simulations. For the material properties and frequency used in the wave propagation study, the ratio of P-wavelength and mesh parameter λ_P/h is 0.83 for the mesh (a) and 10.38 for the mesh (b).

where $Q = 0.1$ is used in all cases, except that for Rayleigh waves $Q = 1$ on the boundary $y = 0$. The coupling parameter σ is given by (3.13).

Typical meshes used in simulations are shown in Fig. 5.7. In this example, uniform meshes are used so the number of P- and S-wave basis functions per element (N_k^P and N_k^S) can be chosen independent of the element number k. However, due to the difference in the P- and S-wave numbers, there may be an advantage in choosing different values for N_k^P and N_k^S. Thus the computational simulations begin by studying how the choice of basis affects the accuracy and the stability of the elastic UWVF approximation. In this and later studies the error is computed using a discrete relative least squares norm as follows. First the UWVF results are averaged at the nodes to obtain nodal values of the displacement (this is motivated by the desire to compare the results to FEM results later). The discrete least squares norm error is simply the unweighted sum of the squares of the nodal error.

In the top panel of Fig. 5.8 the error in the computed solution is shown using various ratios N_k^S/N_k^P and increasing the number of directions per element to give more degrees of freedom. The exact solution in this study is the plane wave (5.7). The results suggest that the ratio of the number of S- and P-wave basis functions (N_k^S/N_k^P) should be approximately κ_S/κ_P in order to obtain the best accuracy. In addition, the bottom panel of Fig. 5.8 shows the conditioning of the $I - D^{-1}C$ corresponding to the computations shown in the top panel. The choice that N_k^S/N_k^P should be of the order of κ_S/κ_P also improves the conditioning of the linear system in most cases (except for very large numbers of degrees of freedom). Thus, both from the point of view of the accuracy and from the point of view of

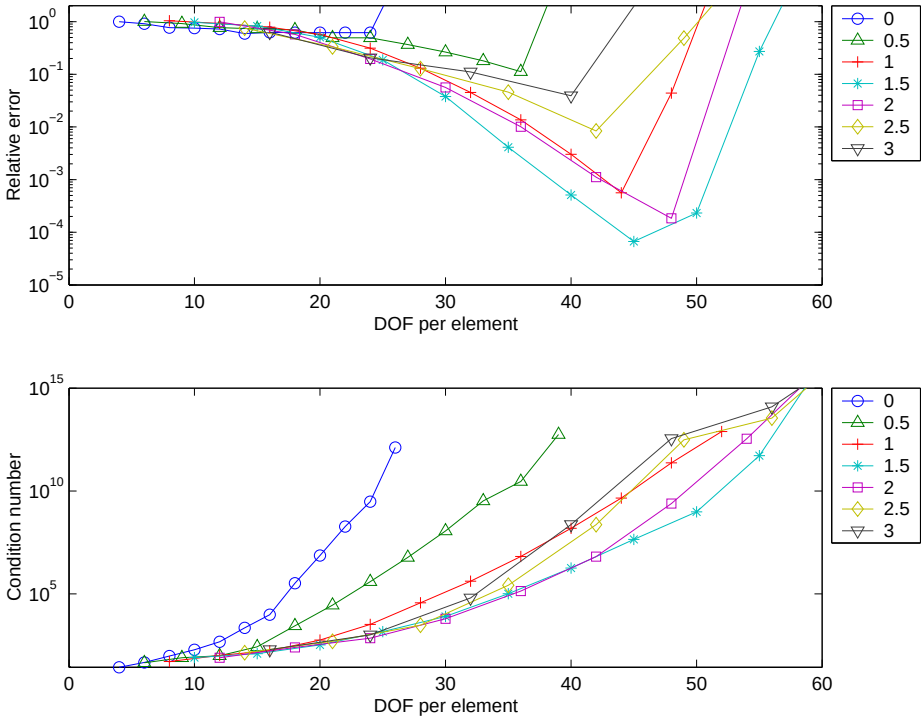

Figure 5.8: Relative error and condition number of $I - D^{-1}C$ as a function of the number of degrees of freedom (DOF) per element for different ratios N_k^S/N_k^P. The exact solution is the plane wave (5.7). Results are computed in the mesh of Fig. 5.7 (a). The frequency is $f = 2.0 \cdot 10^4$ and $\kappa_S/\kappa_P = 1.87$. The eventual blowup of the relative error in the top figure is due to the increase in condition number with the number of degrees of freedom.

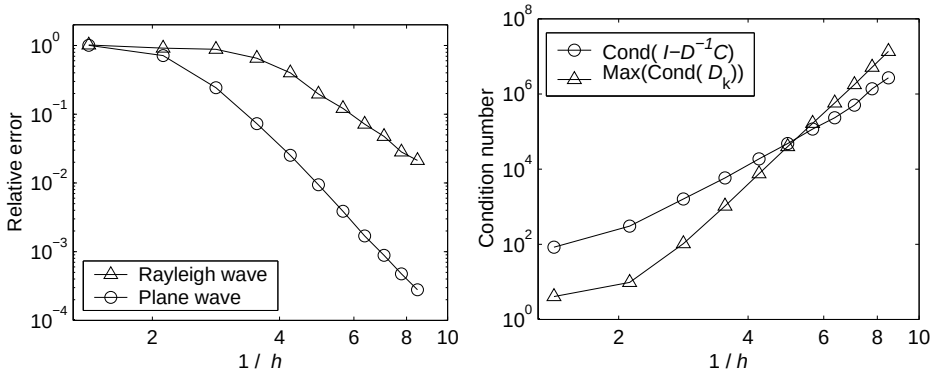

Figure 5.9: Relative error (left) and condition number (right) as a function of the mesh parameter $1/h$. Results are computed with $\kappa_P = 21.4$, $N_k^P = 10$ and $N_k^S/N_k^P = 1.5$.

the stability of the method, the ratio N_k^S/N_k^P should be chosen in the manner just described.

The behavior of the error and conditioning as a function of $1/h$ for a fixed number of basis functions per element (i.e. fixed N_k^P and N_k^S) and variable mesh size is presented in Fig. 5.9. In the figure the error is given for the plane wave and Rayleigh wave problems. From the left panel it can seen that the error for plane wave decreases $O(h^\alpha)$ for $\alpha \approx 6.4$ provided h is small enough. From the right hand panel of Fig. 5.9 one can see that the maximum condition number of the matrix blocks D_k gives a good indication of the condition number of the system matrix $I - D^{-1}C$ and hence, can be used as a predictor of the conditioning of the system matrix as was done in the Helmholtz problem. Then, in practice, it is possible to use a similar approach for the elastic UWVF. The condition numbers of $I - D^{-1}C$ in Figs. 5.9 and 5.10 are computed with $Q = 0.1$ on all boundaries.

Next, in Fig. 5.10 the behavior of the elastic UWVF method is examined on a fixed mesh with a fixed basis, but varying ω so that κ_P and κ_S both vary while keeping κ_S/κ_P fixed. For low κ_P the conditioning of the UWVF matrix $I - D^{-1}C$ is very poor since all plane waves are almost constant on each element. As κ_P increases, the conditioning improves and an accurate solution is obtained. As κ_P increases further, the error then increases as can be expected from analyzing how the solution is approximated by a sum of plane waves. It is again useful to note (from the right hand panel of this figure) that the maximum condition number of the blocks of D is a good estimate of the condition number of the overall system matrix. On the other hand, the condition number $\mathrm{Max}(\mathrm{Cond}(D_k))$ can be used for predicting whether a certain combination of a fixed mesh and a fixed number of basis functions can lead to a good approximation. More precisely, a high

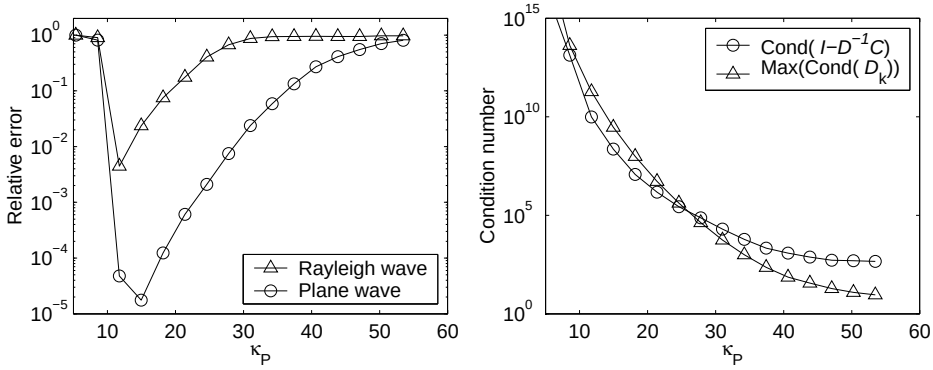

Figure 5.10: Relative error and condition number as a function of the wavenumber κ_P when $N_k^P = 16$ and $N_k^S/N_k^P = 1.5$. Results are computed in the mesh of Fig. 5.7 (a)

condition number indicates instability of the problem, whereas at low condition numbers (below 10^6 in this problem), the mesh may need to be refined or more basis functions may need to be used.

Comparison with piecewise linear FEM

Finally, the piecewise linear finite element method is compared with the UWVF for the plane wave propagation problem (i.e. the exact solution is the plane wave (5.7)). The discrete relative least squares error in the FEM solution against the reciprocal of the element size $1/h$, for a fixed frequency and wavenumber, are shown in the left hand panel of Fig. 5.11. The solution converges with an error that is $O(h^2)$ as is to be expected for the piecewise linear FEM. Comparing the left panel of this figure with the left hand panel of Fig. 5.9, it is obvious that much finer meshes are needed in the finite elements scheme than in the UWVF to obtain equal accuracy. In the right hand panel we examine the dependence of the error of the FEM solution on the wavenumber κ_P (keeping the ratio κ_S/κ_P fixed). As is to be expected, the error increases with κ_P (due to accumulating phase error). Compared to the right hand panel of Fig. 5.10 one sees that the finite element method is free from the low frequency conditioning problem that afflicts the UWVF.

Even though the FEM requires a much finer grid than the UWVF to obtain similar accuracy, one must be careful in comparing the efficiency of the two schemes because the UWVF has a large number degrees of freedom per element. To try to compare the methods more directly, the error in the FEM and UWVF schemes are plotted in Fig. 5.12 as a function of the number of non-zero entries in the resulting matrices. The h-UWVF is computed with the fixed basis on each element

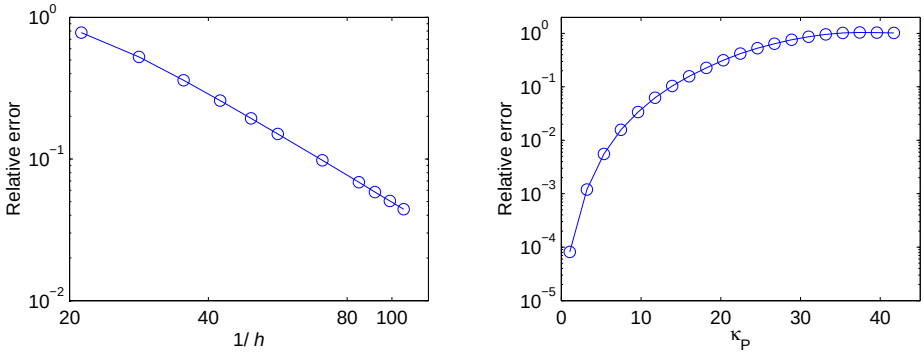

Figure 5.11: Left: A log-log plot of the relative error as a function of the mesh parameter $1/h$ in the finite element scheme. Results are shown for $f = 2.0 \cdot 10^4$ corresponding to $\kappa_P = 21.4$. Right: Relative error against the wavenumber κ_P in the mesh of Fig. 5.7 (b).

and decreasing the mesh size h to obtain an accurate solution, and the p-UWVF is obtained by increasing the number of directions per element on a fixed mesh. Using either strategy the resulting matrix system is more dense in the UWVF than in the FEM. However, the overall storage needed to reach a desired accuracy is lower for the UWVF than for the FEM (see Fig. 5.12). Perhaps this not surprising since the solution is smooth and hence a higher order method (like UWVF) should be more efficient than a low order method like the piecewise linear FEM.

5.3.2 Transmission

As a second model problem, the transmission of elastic plane waves through a circular inhomogeneity is analyzed. The radius of the circle is $r = 0.5$ and it is embedded in an infinite homogeneous background material. Similar problem has been studied for example in [158]. Since the problem is physically unbounded, the computational domain is truncated by another circle with radius $r = 1$ where the absorbing boundary condition developed in Section 3.1.2 is used. The transmission is analyzed in two examples for which material properties of the inhomogeneities and backgrounds are shown in Table 5.3. Essentially, the geometry of the problem is similar as in Fig. 5.1. However, radii of the circular domains are different and incident fields are plane waves instead of point sources used in Section 5.2. In all simulations the frequency is $f = 1.0 \cdot 10^4$.

The incoming wave is of the form (5.7). In some examples, however, cases with incident P- and S-waves are studied separately. The direction of propagation of the incident wave in both cases is $d = (1, 0)$.

The problem is approximated in the ultra weak scheme by using (3.13) as the

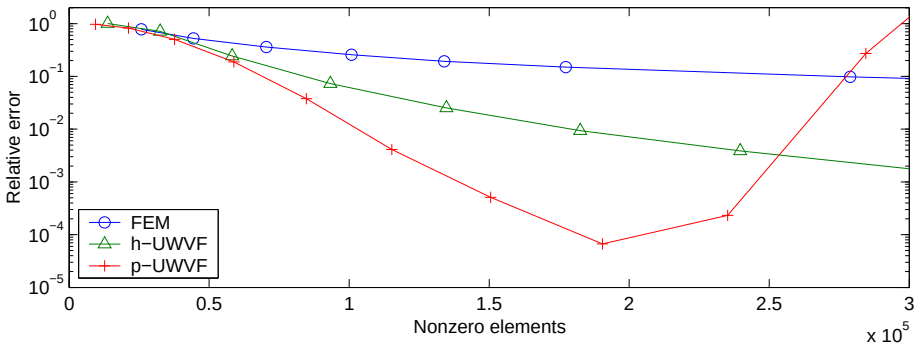

Figure 5.12: Relative error as a function of storage, i.e. the number of non-zero elements in the resulting matrix system. The abbreviation FEM refers to the piecewise linear finite element method; h-UWVF to the elastic UWVF with constant number of basis functions ($N_k^P = 10$ and $N_k^S/N_k^P = 1.5$) and varying element size h; and p-UWVF to the elastic UWVF with fixed mesh (the mesh of Fig. 5.7 (a) and $N_k^S/N_k^P = 1.5$) and varying number of basis functions N_k^P. The results are for $f = 2 \cdot 10^4$.

Table 5.3: Material properties

Ex.	Figs.	Domain	E	ν	ρ	c_P	c_S	c_P/c_S
1	5.13-5.14	Ω_1	$200 \cdot 10^9$	0.30	7800	5875	3140	1.87
		Ω_2	$200 \cdot 10^9$	0.47	7800	12413	2953	4.20
2	5.15-5.17	Ω_1	$200 \cdot 10^9$	0.30	7800	5875	3140	1.87
		Ω_2	$14 \cdot 10^9$	0.25	1800	3055	1763	1.73

coupling parameter, setting $Q = 0$ and

$$g = T^{(n)}(u^{\text{in}}) - i\sigma u^{\text{in}} \quad \text{on } \Gamma.$$

Assuming that the solution of the problem in Ω_2 now consists of the incoming and scattered fields $u = u^{\text{in}} + u^{\text{sc}}$, these particular choices correspond to the first order absorbing boundary condition (3.12) for the scattered part u^{sc}.

For comparison, an accurate approximation to the physical transmission problem is computed using a truncated Fourier-Bessel series. This method is described in full detail in [158]. The infinite Fourier series is truncated when the relative change of solution due to an additional Fourier mode is less than 10^{-5}.

There are three sources of error in the UWVF calculation. First, the unbounded problem is computed in a bounded domain with an absorbing boundary condition. This is probably the main source of error in the simulations of this section. Second, the interior circle is approximated using a polyhedral approximation (in the work on the Helmholtz equation, the UWVF with curved boundaries was implemented). Finally, of course, there is the approximation error due to discretizing the problem on the bounded domain by the UWVF. Due to the first two approximations a discrepancy of the order $5-15\%$ can be expected between the UWVF and Fourier series approximations even for very fine grids or large numbers of directions per element. In fact, the numerical experiments show that the asymptotic error of the method is around 10%. The error due to the ABC could be reduced by increasing the distance between the scatterer and the absorbing boundary.

Because the mesh, shown in Fig 5.13, is unstructured and the elastic properties depend on position it is helpful to vary the total number of basis functions, and the ratio of number of S- and P-wave basis functions element by element. Since the accuracy of the UWVF approximation depends on both of these factors, they are analyzed separately. In the first part of the study, a fixed ratio of the S- and P-wave basis functions are chosen, and a feasible method to choose the total number of basis functions in each element is sought. This part is similar to the method used to choose the number of basis function for the Helmholtz problem. In the second part of the study, the effect of the S- and P-wave composition of the basis functions on the UWVF approximation is shown.

The results of the wave propagation example (Section 5.3.1) suggest that the ratio of S- and P-wave basis functions N_k^S/N_k^P should be about the local ratio of the wave numbers κ_S/κ_P. By setting $N_k^S/N_k^P = \kappa_S/\kappa_P$, one can compare two approaches for choosing the total element by element number of basis functions. The first, and the most obvious method, is to use equal number of P-wave basis functions in all elements. Naturally, the total number of basis functions is then defined by the local ratio $N_k^S/N_k^P = \kappa_S/\kappa_P$. The second method is to choose the total number of basis functions for each element K_k so that the condition number of the corresponding matrix block D_k is below a user supplied allowed limit. More precisely, the highest number of P-wave basis functions which results in the condition number below this limit has been used. This approach is similar to that used in [108] for the ultra weak approximation of the Helmholtz problem. By varying the desired condition number it is possible to vary the number of

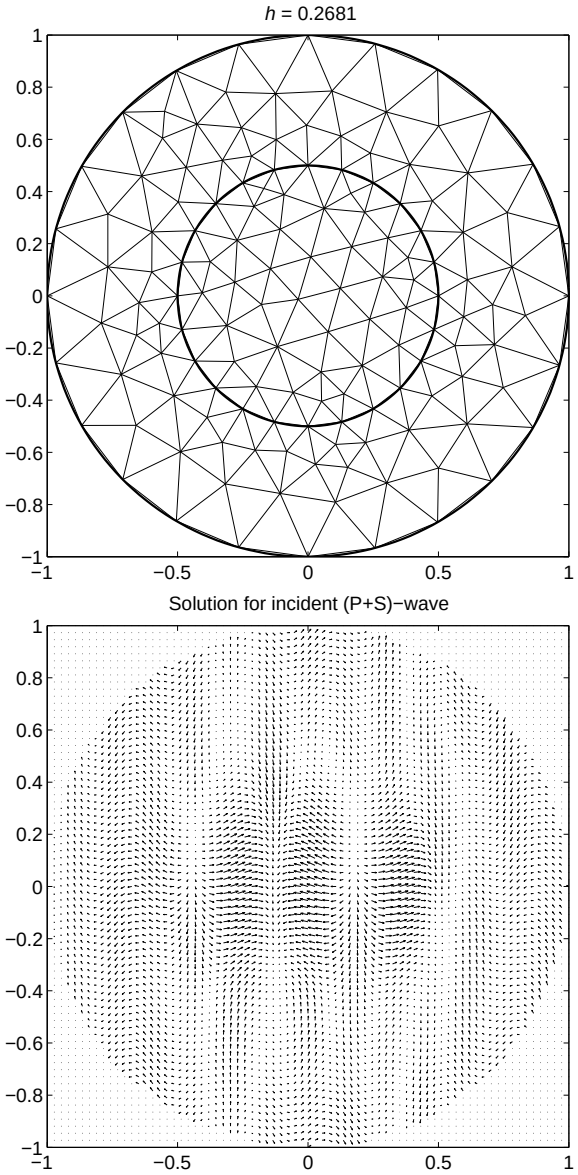

Figure 5.13: Top: The mesh used for the transmission problem. Bottom: The real part of the solution of the transmission problem with the incident wave consisting of both P- and S-components.

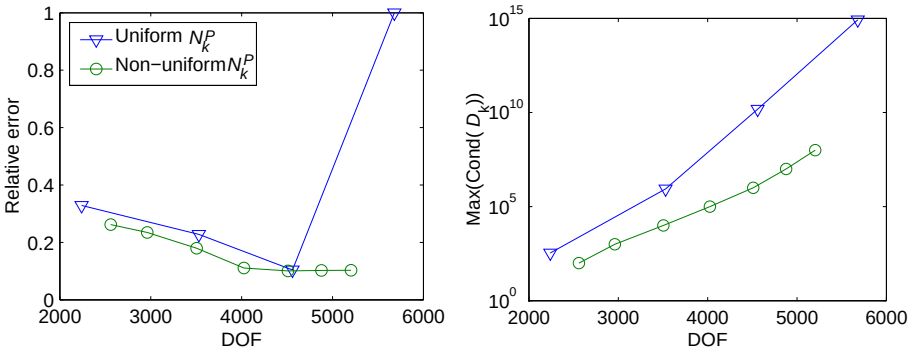

Figure 5.14: Comparison of two approaches for choosing the total number of basis functions. The non-uniform number of P-wave basis functions N_k^P for the element K_k is chosen based on the condition number of the matrix block D_k. In both cases the number of S-wave basis functions is defined by the local ratio of wave numbers as $N_k^S/N_k^P = \kappa_S/\kappa_P$.

directions per element. The mesh is fixed (Fig. 5.13) so the method is essentially the p-UWVF studied in Fig. 5.12 (in particular the polygonal approximation of the circular scatterer does not improve with more degrees of freedom).

In this part of the study, the material parameters listed for Ex. 1. in Table 5.3 are used. Note that the inhomogeneity and the background materials have a remarkably different ratios c_P/c_S. Accordingly, the ratio N_k^S/N_k^P has the same variation between the two domains. The solution of the problem for (P+S)-wave incident field (i.e. $\alpha = 1$, $\beta = 1$ in (5.7)) and for $f = 1.0 \cdot 10^4$ is shown in Fig. 5.13.

The error and the maximum condition number of D_k as a function of the number of degrees of freedom (DOF) for the uniform and non-uniform number of P-wave basis functions are shown in Fig. 5.14. The relative error refers to relative difference between UWVF and Fourier series solutions. Note that using a uniform number of P-wave basis functions causes the conditioning of the problem to deteriorate rapidly which in turn causes the error to blow up. Therefore, in the following examples, the number of basis functions is chosen according to the conditioning of D_k.

Although the wave propagation example indicates that the ratio of S- and P-wave basis functions should be about the ratio of the S- and P-wave numbers, it is worthwhile to confirm this hypothesis also for a more complex problem. As in the previous section, the effect of the choice of the ratio N_k^S/N_k^P of the basis functions on the accuracy of the elastic UWVF approximation is studied next. To obtain almost homogeneous ratio of the wave numbers in the whole computation domain, the material parameters of Ex. 2. from Table 5.3 have been chosen. The

wave numbers for the two subdomains are different, causing significant scattering of waves from the interface, but the ratio c_P/c_S is approximately equal for both materials. This allows a straightforward comparison between the ratios N_k^S/N_k^P and κ_S/κ_P; and performance of the UWVF.

Since the number of basis functions for each element is chosen now according to the condition number of D_k, the relative error as a function of the maximum allowed condition number is shown in Fig. 5.16. The composition of the basis is varied by changing the ratio of S- and P-wave basis functions N_k^S/N_k^P. The results are computed for both P- and S-wave incident fields for which the solutions are shown in Fig. 5.15.

The error for the same set of simulations is shown as a function of the number of degrees of freedom in Fig. 5.17. It is notable that the error in the solution can be controlled by choosing the desired maximum condition number (this in turn affects the convergence rate of the bi-conjugate gradient scheme which may not converge if the condition number is chosen too large). Of course the asymptotic error in the computed solution is different for S- and P-incident waves because of the differences in the scattered wave in each case.

5.4 Discussion and conclusion

In this section a practical method for choosing the number of basis functions per element for the UWVF was introduced. The method is based on the individual conditioning of the matrix blocks D_k. This condition number predicts the stability of the overall matrix system rather well. Keeping the condition number below a predetermined level resulted in a stable solution of the problem. The same approach has proven feasible for both the Helmholtz and the Navier problems. In the elastic case, however, it is necessary to choose the number of S- and P-wave directions depending on the ratio κ_P/κ_S to improve both the accuracy and conditioning of the elastic UWVF.

The results from the elastic UWVF show that the method is capable of resolving surface wave fields for which the decompostion into independent P- and S-components is not readily apparent. However, the accuracy of the method for the surface waves is not as good as for plane waves (this is obvious since the plane wave basis used in this study is perfectly suited to approximate plane waves). To maintain tolerable accuracy for problems in which surface or edge waves are generated, a finer spatial discretization or more basis functions near surfaces may be required.

The comparison with the FEM shows that the UWVF compares well to the piecewise linear FEM. The comparison was limited to the plane wave problem only. However, it is known from previous studies that high-order finite elements are needed to properly simulate Rayleigh waves [168].

The elastic UWVF performed well also in problems with an inhomogeneous medium. The study of the accuracy of the method is possible only to a limited extend due to the discrepancy between the UWVF approximation and the exact Fourier series solution. This resulted from the approximate absorbing boundary

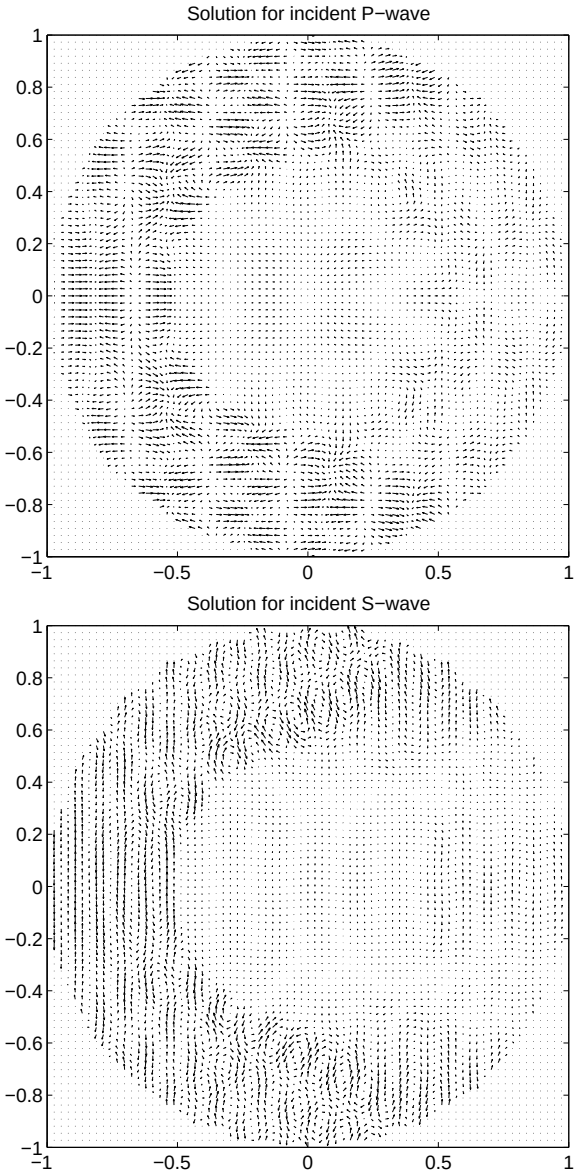

Figure 5.15: Top: The real part of the solution of the transmission problem with the incident P-wave. Bottom: The real part of the solution of the transmission problem with the incident S-wave. Both solutions correspond to $f = 1.0 \cdot 10^4$.

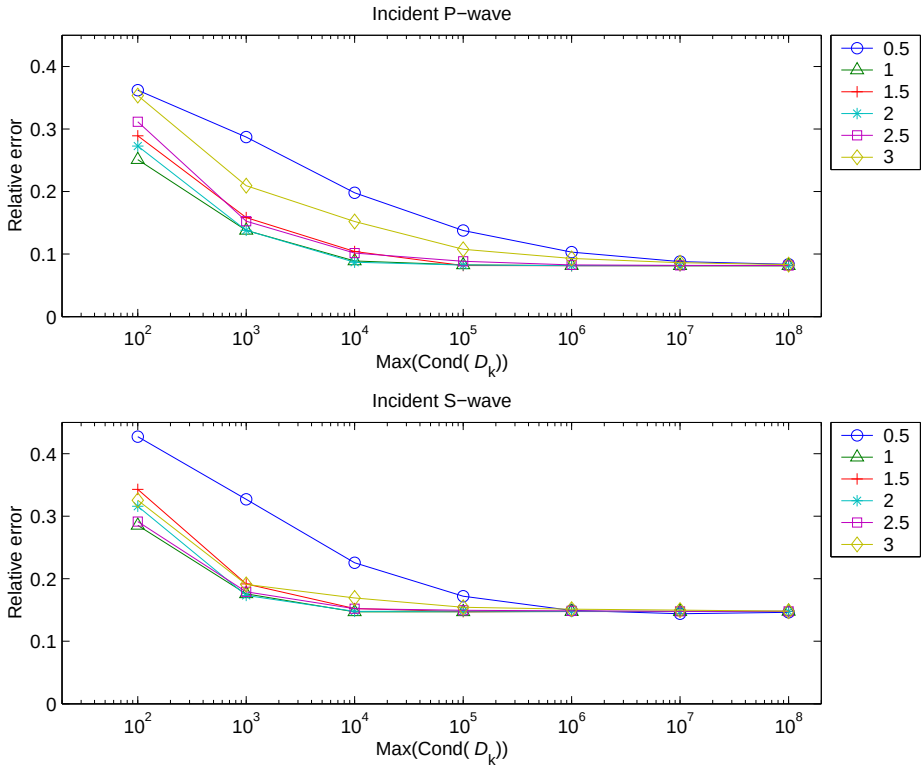

Figure 5.16: Relative error as a function of maximum condition number of the blocks D_k. Each curve shows the error for a fixed ratio of N_k^S/N_k^P. The maximum accuracies for the incident P- and S-waves are 8% and 15%, respectively. The discrepancy of this order between the Fourier series and UWVF approximations are due to the low order absorbing boundary condition and the approximation of the curved boundary by the UWVF.

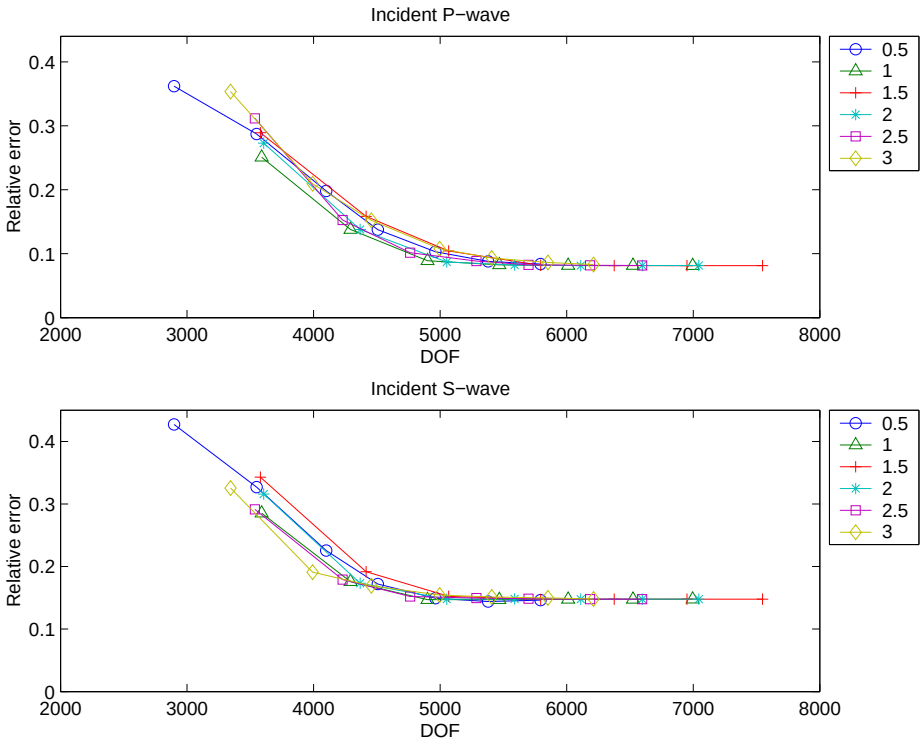

Figure 5.17: Relative error as a function of the number of degrees of freedom for the transmission problem.

condition used in the UWVF scheme and the approximate fitting of the curved boundary by a polygon. Further investigations are needed to see whether the UWVF method is feasible for more complicated problems of elastodynamics in 3D.

The simulations in this chapter were computed in 2D. The extension of the UWVF for the Helmholtz problem in 3D is discussed in the following chapter. The 3D version of the method utilizes the perfectly matched layer absorbing boundary condition that was outlined in Section 3.1.3.

Chapter VI

Parallelized 3D Helmholtz solver using the PML

The numerical studies in the previous section were performed for two dimensional problems. The extension of the UWVF-PML to 3D requires further improvements to the computational procedure. Although in comparison with the low order finite elements, the UWVF reduces the computational burden, the problems, especially in the case of ultrasound fields, are still remarkably large. To be able to utilize modern parallel computers, a parallelized UWVF-technique must be developed.

The UWVF method is derived using the spatial decomposition of the underlying physical problem. Obviously, domain-based parallelism serves a natural framework to develop a parallel UWVF code. A review of domain-based techniques applied to various problems in science and engineering is given in [123]. In this chapter, the parallel version of the UWVF-PML method for the 3D Helmholtz problem is outlined.

Since for spatial discretization the UWVF uses standard finite element meshes, a technique for mesh partitioning is discussed first. However, unlike for a low order FE method, the number of unknowns per element can have substantial variation within the mesh. Therefore, the partitioning to equally sized parts (in terms of the number of elements) does not lead to a balanced load between processors. To improve the load balance, a weighted partitioning scheme is introduced in Section 6.2. Finally, in Section 6.3 numerical experiments for the modeling of ultrasound fields are performed using the parallelized UWVF-PML method. Studies of the previous section did not include the PML, therefore the main emphasis in the numerical examples of this section is given to the performance of the PML.

6.1 Partitioning of the mesh

The idea behind an efficient parallelized UWVF code is that the computational mesh is first partitioned into n parts where n is the number of processors. Then each processor assembles the parts of the matrices D and C along with the right hand side b for the corresponding part of the mesh. The blocks D_k for the matrix D can be constructed using geometric and material property information of the

element K_k only. However, for the blocks in the coupling matrix C, information from the elements adjacent to K_k are needed which necessitates communication between processors. Furthermore, for solving the matrix equation (4.28) with an iterative solver, the matrix-vector multiplication $(I - D^{-1}C)X$ is computed on each iteration which again calls for communication between subprocesses. Since in Chapter 5. the Bi-CGStab was found to converge faster than the Richardson iterative method, only parallelized Bi-CGStab is used in following simulations. The parallel implementation of the Bi-CGStab methods are discussed in more detail in [199].

On one hand, it is known that the bottleneck in parallel iterations is often the amount of communication between processors. On the other hand, it is obvious that the amount of communication can be reduced with the number of faces of tetrahedra shared by different parts of the mesh. The method used in this thesis is based on the multilevel partitioning of the mesh [119] using the single processor version of METIS software package [118].

6.2 Load balancing

Let the element K_k be occupied by N_k basis functions. Furthermore, in the case of a tetrahedral mesh, the element has four faces shared with adjacent elements or at least one of the faces is on the exterior boundary. The number of entries in the matrices D and C of (4.28) for a single element is then

$$M_k = N_k^2 + \sum_{\ell=1}^{4} N_k N_{j_\ell} \tag{6.1}$$

where N_{j_ℓ} is the number of basis functions in the element K_j sharing the face $\Sigma_{k,j}$ or $N_j = N_k$ if the face is on exterior boundary. The storage needed for the right hand side and the vector to be solved in (4.28) together with vectors in the iterative solver can be taken into account with an additional storage of mN_k coefficients. The value of m depends on the type of the iterative solver being used.

As discussed in Section 5.1.2, the method used to choose N_k in 2D examples relied on limiting the conditioning number of matrix blocks D_k below a predetermined limit. The number of basis functions N_k and the building of D_k was then obtained as a sequential procedure. More precisely, after an initial guess for N_k, the matrix block D_k was computed and the condition number of D_k was evaluated. This procedure was continued until the highest N_k which provided the condition number below the user set limit was found.

In the parallelized approach, the previous scheme used to choose N_k faces two drawbacks. First, to use parallel processing efficiently, the mesh must be partitioned to each processor before starting of the dynamic procedure for selecting N_k. The partitioning of the mesh so that each part has approximately equal number of elements may lead to severe imbalance between loads at different processors. Namely, if the element size and material properties vary within the mesh, the number of basis functions that give an equal condition number of D_k varies significantly between elements. Second, in 2D examples the initial guess for N_k was

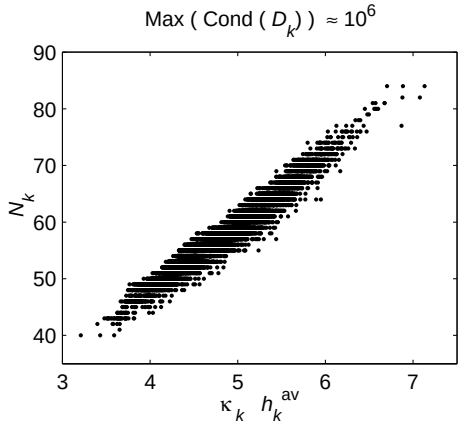

Figure 6.1: The number of basis functions per element N_k as function of product of the wave number κ_k and element size h_k^{av} for a fixed condition number $\text{cond}(D_k) < 10^6$. The data corresponds to the simulation of Fig 6.4 when $\sigma_0 = 0$.

chosen equal for each element. However, in 3D , due to the increased number of elements and number of basis function per an element, this approach becomes intolerably time-consuming. Both these drawbacks call for a method to estimate N_k prior to partitioning based on the element size and material properties in the element.

The numerical experiments in Chapter 5 show that the condition number of D_k depends on the element size h_k and wave number κ_k. Based on the numerical simulations, let the mesh size h_k^{av} be defined as the average distance of element vertices $r_{k,\ell},\ \ell = 1, ..., 4$ from the centroid $r_{k,C}$ of K_k

$$h_k^{\text{av}} = \frac{1}{4} \sum_{\ell=1}^{4} |r_{k,C} - r_{k,\ell}|.$$

Then, the point source example of Section 6.3.1 in the case of $\kappa_k \in \mathbb{R}$ shows almost linear correlation between the number of basis function per element N_k and the dimensionless quantity $\kappa_k h_k^{\text{av}}$, see Fig. 6.1. Therefore, the initial guess can be made in the form

$$N_k = A(\kappa_k h_k^{\text{av}}) + B, \tag{6.2}$$

where the parameters A and B can be found as a linear fit to the experimental data. For example, the data of Fig. 6.1 gives $A = 11.2$ and $B = 3.4$.

The METIS allows weighed partitioning of the mesh. For load balancing, the approximately linear relation between $\kappa_k h_k^{\text{av}}$ and N_k provides means of estimating the number of matrix entries M_k corresponding to each element K_k. Furthermore,

the use of M_k and mN_k to weight K_k in METIS gives a relatively balanced memory storage for all processors.

After the mesh is partitioned, the dynamic procedure of Section 5.1.2 can be used to choose the stable number of basis functions N_k and to build the blocks D_k. A significantly reduced number of trials is needed for finding N_k due to the improved initial guess (6.2). However, the estimate (6.2) can be misleading if the medium in K_k is strongly absorbing since the effect of imaginary part of κ_k is not taken into account.

6.3 Numerical studies

To investigate the feasibility of the UWVF-PML method for large-scale wave field simulations, a series of numerical experiments are performed for the propagation and scattering of time-harmonic acoustic waves. It is known from experience with finite difference and finite element methods that the PML parameters n, $\sigma_{0,\ell}$ and the thickness of the PML must be properly adjusted to reduce numerical reflections to an acceptable level. The effect of the PML parameters to the accuracy of the UWVF-PML approximation will be discussed here.

As noted in Section 4.1.1, the directions for the plane wave basis functions are obtained from optimized spherical coverings [93]. The number of basis functions for each element is chosen based on the condition number of the matrix block D_k [108]. The maximum allowed condition number in all simulations is set to 10^6. The number of basis functions per element is limited to between 1 and 130. The element size is chosen so that the upper limit for the number of basis functions is not exceeded. The discrete problem (4.28) is solved by the stabilized bi-conjugate gradient iteration which is truncated when the relative residual reaches a value below 10^{-6}.

Before proceeding to the analysis of the PML, the scalability of the parallel UWVF method outlined in the beginning of this chapter is tested. The computer code used in the simulations is coded with Fortran90 and parallelized using MPI (Message Passing Interface). The computations are done with a Beowulf PC cluster consisting of 12 1.8 GHz Pentium 4 processors and having 11.5 GB total RAM. The processors are networked using a 1 GB ethernet switch. All simulations of this chapter, not including the scalability study, are computed using 11 processors.

6.3.1 A point source

The first test problem consists of a point source

$$p(r, r_0) = \frac{1}{4\pi} \frac{e^{i\kappa|r-r_0|}}{|r-r_0|} \tag{6.3}$$

in a cubic computational domain centered at the origin. The location of the source is $r_0 = (x_0, y_0, z_0)$ and $r = (x, y, z)$ is an observation point.

In the UWWF, a point source is obtained by having $f_s = \delta(r - r_0)$ in (4.29)-(4.32) where $\delta(r - r_0)$ is the Dirac delta function. The entries for the right hand

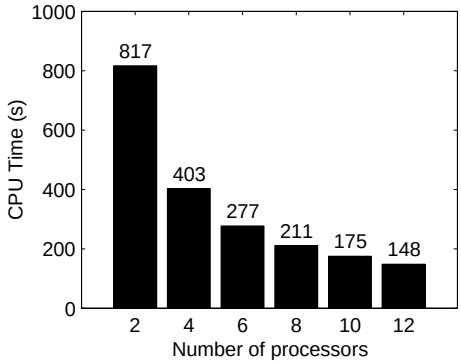

Figure 6.2: Exectution time of the UWVF solver as a function of the number of processors.

side of equation (4.28) are thus

$$b_k^\ell = \frac{2i}{\rho_k} \int_{K_k} f_s \eta_k^2 \overline{\varphi}_{k,\ell} = \frac{2i}{\rho_k} \eta_k^2 e^{-i\overline{\kappa}_k a_{k,\ell} \cdot r_0}. \tag{6.4}$$

Since in all studies of this thesis, the source is located in the non-PML region it follows that $\eta_k^2 = 1$. Furthermore, in all examples for this first model problem, the material parameters are set $c = 1500$ m/s and $\rho = 1000$ kg/m^3.

Scalability of the parallel UWVF solver

An essential property of an efficient parallel code is the reduction of total computation time with increase in the number of processors attending to the computation. In an ideal case, the doubling of the number of processors should halve the computation time. In practice, however, the increase of processors also requires more inter-processor messaging which slows down the computation. The first numerical example investigates the scalability of the parallel UWVF code.

In the scalability study, the point source is located at origin $r_0 = (0, 0, 0)$ mm and the computational domain is a box with the edge length 20 mm. The Sommerfeld type boundary condition (3.2) is used on the exterior boundary. The frequency of the wave field is $f = 100$ kHz corresponding to the wavelength $\lambda = 15$ mm. This test problem with a low wave number problem allows computations using a small number of processors.

Total computation time as a function of the number of processors is shown in Fig. 6.2. The execution time reduces almost ideally with the increase in the number of processors, that is, the time is inversely proportional to the number of processors. However, when the number of processors for this small test problem increases, time needed for communication may become notable. Fortunately in larger problems in which the computation time consist merely of floating point

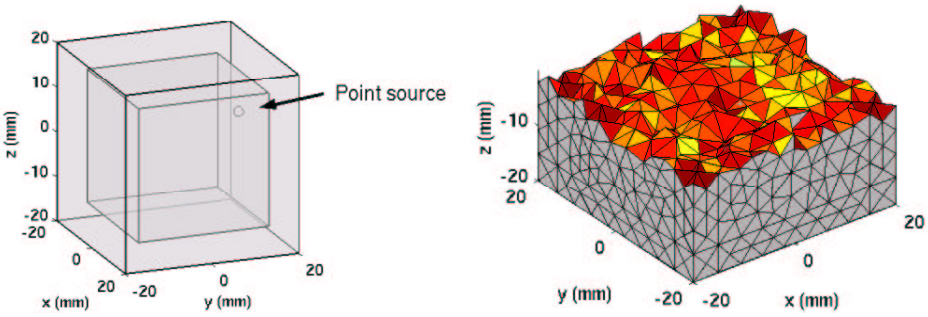

Figure 6.3: Geometry and a cross-section of the mesh for the model problem 1. A point source is located at $r_0 = (10, 10, 10)$ mm.

.

operations rather than messaging, the benefit of increasing number of processors remains longer.

Performance of the PML

In the second part of the point source test problem, the performace of the PML is examined. The domain consist of two concentric cubes with side lengths 30 and 40 mm. The region outside the smaller cube constitutes the PML (see Fig. 6.3). The off-centered point source is located at $r_0 = (10, 10, 10)$ mm. The frequency used in this study is $f = 500$ kHz and the resulting wavelength of the sound field is $\lambda = 3.0$ mm.

Fig. 6.3 also shows a cross-section of a typical mesh used in simulations. The longest edge of a tetrahedron in that mesh is $h = 7.2$ mm which is over twice the wavelength.

The UWVF-PML approximations are computed for the zeroth order damping layer (i.e. $n = 0$) and by varying the damping coefficient $\sigma_{0,\xi} = \sigma_0$. For the exterior boundary condition (4.6), it is set $Q = 0$, $g = 0$ and the parameter σ is given in (4.9). Note that in the case of $\sigma_0 = 0$, the exterior boundary condition corresponds to the zeroth order absorbing boundary condition (4.9). The exact solution and UWVF-PML approximations with different σ_0 are shown in Fig. 6.4. Relative errors in the $x = 0$ mm plane inside the inner cube are listed in Table 6.1. In the table are also listed the variation in the number of basis function per element N_k, the number of degrees of freedom in the problem (DOF) and variation in parameter $\sqrt[3]{6N_k}\lambda h_k^{-1}$ where h_k is the longest edge of the tetrahedron K_k. This parameter can be considered as an indicator to the needed number of degrees of freedom per wavelength. The UWVF uses values $\sqrt[3]{6N_k}\lambda h_k^{-1} < 6.7$ that are below the rule of thumb $\frac{\lambda}{h} \approx 10$ typical for low order finite elements. Despite the relative low value of $\sqrt[3]{6N_k}\lambda h_k^{-1}$, the error of the UWVF-PML approximations is below 1 %.

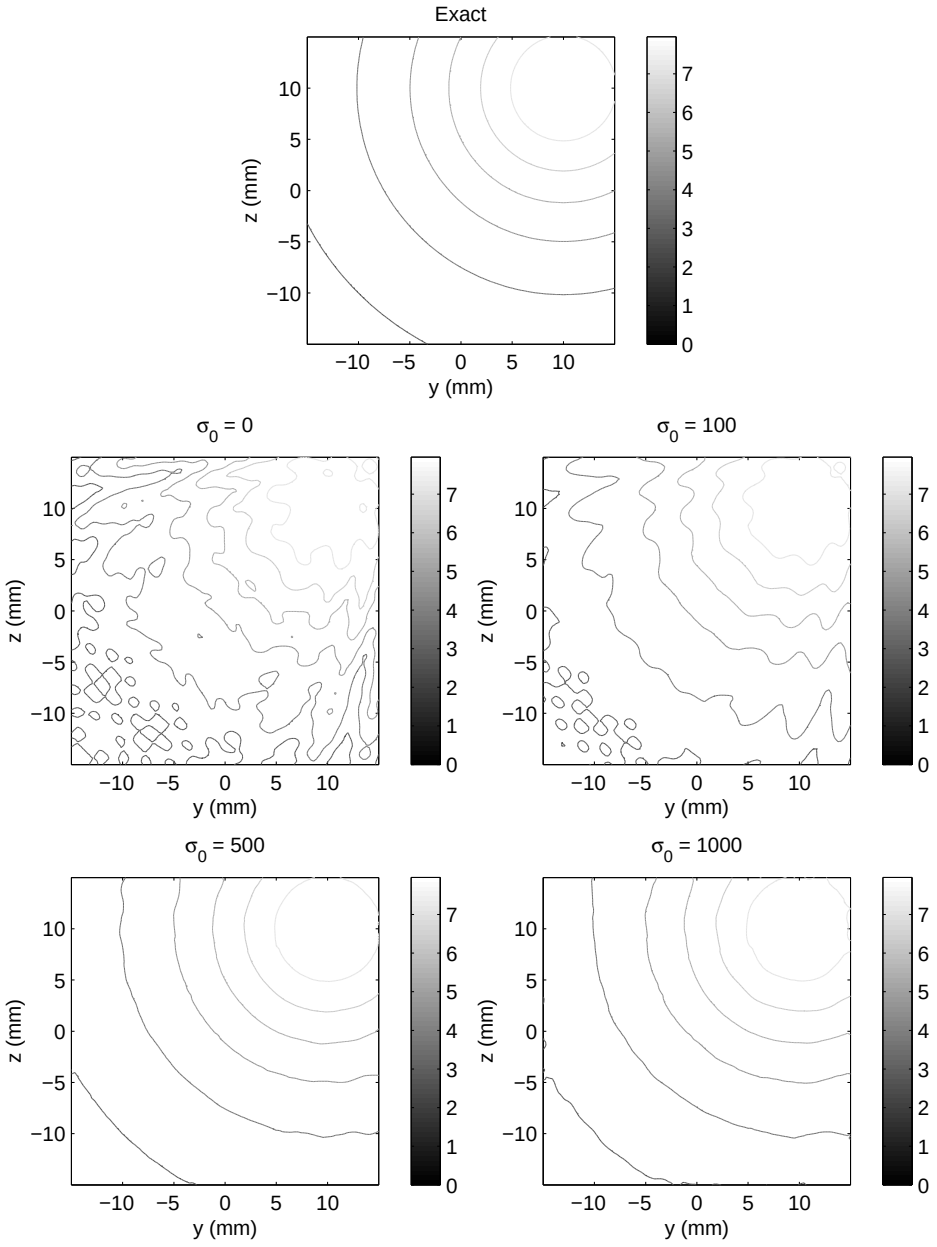

Figure 6.4: The absolute value of the exact field in the plane $x = 0$ (top row). The UWVF approximation with a zeroth order ($n = 0$) PML having different damping coefficients $\sigma_{0,\xi} = \sigma_0$ are shown in the remaining panels. Note that the field is shown in the non-PML region. The boundary condition (4.9) is used on the exterior boundary.

Table 6.1: Summary of the results of point source simulations

σ_0	N_k	DOF	$\sqrt[3]{6N_k}\lambda h_k^{-1}$	Err%
0	40 - 84	707 744	3.22 - 6.62	9.95
100	37 - 84	669 306	3.22 - 6.42	4.55
500	10 - 84	549 029	2.35 - 6.28	0.38
1000	1 - 84	422 666	1.09 - 6.28	0.62

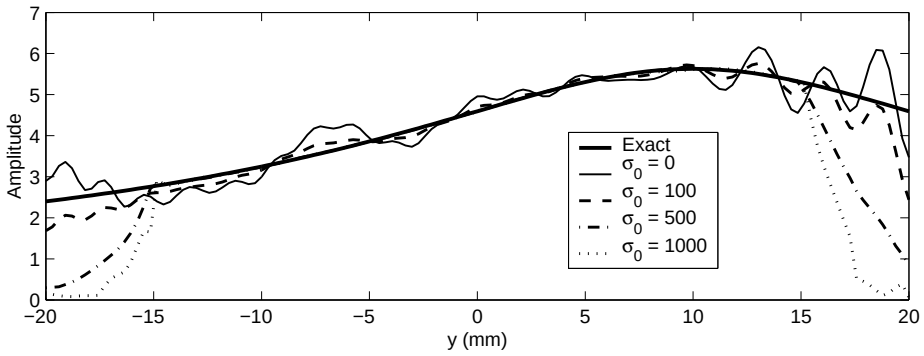

Figure 6.5: The amplitude of the acoustic field as a function of y for various damping parameter values. The fields along the y-axis decay inside the PML damping layer $|y| > 15$ mm. Outside the PML the field computed using $\sigma_0 = 500$ is indistinguishable from the exact solution. For a large damping coefficient, the adaptive choice of the plane wave basis functions in the UWVF allows only a small number directions for the elements in the PML. This is most likely a reason for the slightly reduced accuracy of UWVF approximation in the case of the largest σ_0.

The smallest error occurs with the value $\sigma_0 = 500$. A larger σ_0 results in a slightly poorer accuracy. This is most likely due to the conditioning based method for choosing the number of basis functions for each element. More precisely, increasing σ_0 deteriorates the conditioning of the matrix blocks D_k and thus reduces the number of basis functions per element. Small number of plane wave basis functions weakens the matching of the UWVF impedance functions across elements faces and naturally increases the error. On the other hand, for the lower σ_0 the reduced number of basis functions in the PML decreases the number of degrees of freedom for the problem while σ_0 is large enough that high accuracy still remains. The plot along y-axis shows the rapid decay of the field in the PML (Fig. 6.5).

6.3.2 Inhomogeneous and absorbing medium

For the second example, the computational domain is divided into two parts with the plane $z = 0$. The material properties for the upper ($z > 0$) and lower ($z < 0$) half spaces are (κ_1, ρ_1) and (κ_2, ρ_2), respectively. Complex wave numbers κ_1 and κ_2 are used, i.e. the materials have non-zero absorption coefficients $\alpha_1 = 20$ Np/m and $\alpha_2 = 40$ Np/m. The other material parameters are $c_1 = 1500$ m/s, $c_2 = 2000$ m/s, $\rho_1 = 1000$ kg/m^3 and $\rho_2 = 1200$ kg/m^3. These result in wavelengths $\lambda_1 = 3$ mm and $\lambda_2 = 4$ mm for upper and lower half spaces.

As in the first example, the field is emitted by a point source located at the point $(0, 0, h)$ where $h = 10$ mm. An analytical solution for the field is [49]

$$p(r,h) = \begin{cases} \dfrac{e^{i\kappa_1 R^+}}{4\pi R^+} + \dfrac{e^{i\kappa_1 R^-}}{4\pi R^-} - \dfrac{\beta}{2\pi}\int_0^\infty J_0(\zeta R) e^{-\mu_1(z+h)} \dfrac{\zeta\mu_2 d\zeta}{\mu_1(\beta\mu_2+\mu_1)}, & z > 0, \\ \dfrac{1}{2\pi}\int_0^\infty J_0(\zeta R) e^{\mu_2 z - \mu_1 h} \dfrac{\zeta d\zeta}{\beta\mu_2+\mu_1}, & z < 0, \end{cases} \tag{6.5}$$

where $R = \sqrt{x^2+y^2}$, $R^\pm = \sqrt{R^2 + (z \mp h)^2}$ and $\beta = \rho_2/\rho_1$. The Bessel function of order zero is denoted by J_0 and $\mu_j = \sqrt{\zeta^2 - \kappa_j^2}$, $j = 1, 2$. The integrals of (6.5) can be easily approximated with the trapezoidal rule. Since the integrands of (6.5) decay rapidly, the upper bound of the integral can be chosen so that no significant truncation errors occur from replacing the infinite limit by a finite value.

As discussed in Section 4.1.3, equation (4.43) should not be applicable to approximate the field inside elements where the wave number is complex and an additional post-processing step is required. Since equation (4.43) remains valid on the element interfaces $\partial\Omega_k$, it is useful to estimate the error that follows from the use of (4.43) for the elements in the absorbing media. Therefore, in Table 6.2 the accuracy of the fields computed using (4.43) and (4.49) are compared. The corresponding UWVF approximations and the exact solution for the problem are presented in Fig. 6.6. It is clear that the use of (4.49) improves the accuracy of the scheme.

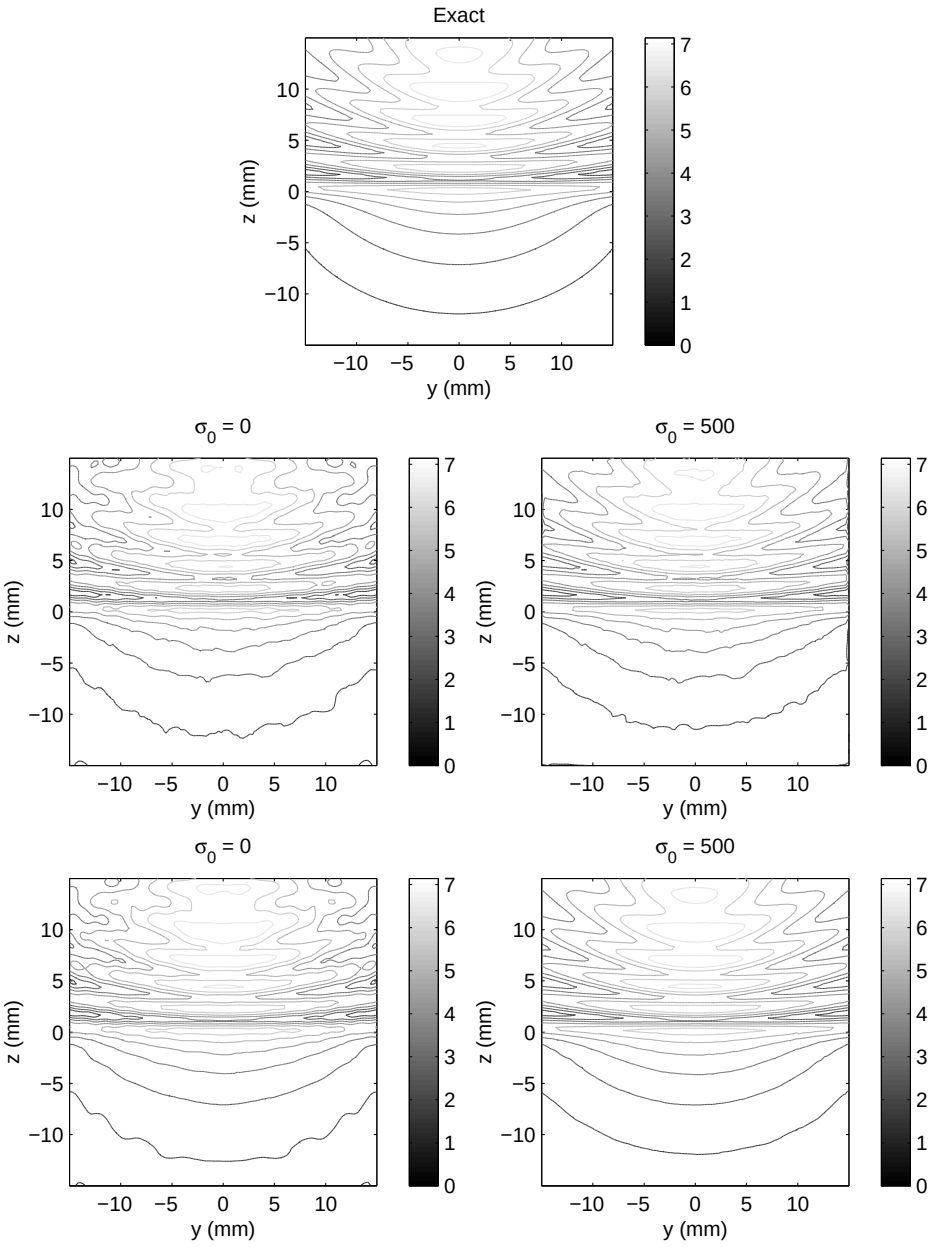

Figure 6.6: The exact solution (top row), the UWVF approximations when computed with equation (4.43) (middle row) and the UWVF approximations using Equation (4.49). Figures show the field inside the non-PML region in the $x = 10$ mm plane.

Table 6.2: Simulations for inhomogeneous absorbing medium

Approximating Eq.	σ_0	Err%
(4.43)	0	5.54
	500	3.37
(4.49)	0	4.51
	500	0.41

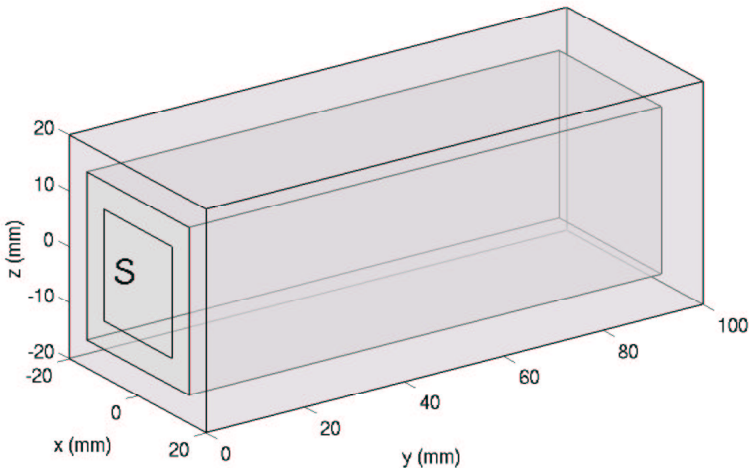

Figure 6.7: Geometry of the third model problem. The field is generated by a uniformly oscillating rigid surface S in the plate $y = 0$. The rest of the $y = 0$ face is modeled as a perfectly rigid surface. The region between the inner and outer cubes constitutes the PML.

6.3.3 Uniformly oscillating surface on a rigid baffle

The third test problem is typical for many applications of acoustics. The study concerns a field generated by a rigid infinite surface of which a finite region S is oscillating with normal velocity amplitude v_n. The reference field generated by such a source in a homogeneous fluid can be computed using the Rayleigh integral

$$p = \frac{i\omega\rho v_n}{2\pi} \int_S \frac{e^{i\kappa|r-r_0|}}{|r-r_0|} dS(r_0), \tag{6.6}$$

where r_0 denotes now a point on the oscillating surface. In addition, it is assumed that the velocity amplitude v_n is uniform throughout the surface S. The region of interest has dimensions $30 \times 95 \times 30$ mm which is surrounded by a 5 mm thick damping layer (see Fig. 6.7). Motivated by the previous example parameters $n = 0$ and $\sigma_0 = 500$ are used. The material parameters for the medium and the frequency $f = 500$ KHz are identical to those for the first test problem.

The oscillating and rigid boundaries are obtained using Neumann type boundary conditions in the UWVF. More precisely, in the $y = 0$ plane, let $Q = 1$, $f_s = 0$ and σ as in (4.9). In addition, the source terms $g = -2i\omega v_n$ and $g = 0$ are used for the oscillating and rigid boundaries, respectively. The rectangular face in the $y = 0$ plane with the side length of 20 mm acts as the source while the rest of the plane is modeled as a rigid surface (see Fig. 6.7).

The fields are presented in Fig. 6.8. Use of the PML reduces the error from 8.18% to 1.54%. The variability in the number of basis functions per element was 42-85 for $\sigma_0 = 0$ and 10-84 when $\sigma_0 = 500$. The benefit of the damping layer can be seen more clearly on the central axis of the source (Fig.6.9).

6.4 Discussion and conclusions

This chapter showed the feasibility of the parallelized 3D ultra weak variational formulation with the perfectly matched layer for the modeling of large-scale acoustic Helmholtz problems. The method was investigated with computational experiments. In comparison with a low order absorbing boundary condition, the zeroth order ($n = 0$) PML showed significant improvement in accuracy. In all problems studied, the accuracy of the UWVF-PML approximation could be adjusted to obtain an error of the order 1 %. This is sufficient accuracy for most engineering applications.

The directions for the plane wave basis functions in the UWVF were uniformly distributed on the unit sphere and the number of directions per element were chosen according to a conditioning based criterion. The maximum allowed condition number for the matrix blocks D_k in all simulations was set to 10^6. Using this scheme, the accuracy of the UWVF approximation in all numerical examples was mainly limited by the absorbing boundary condition. However, when the PML parameter σ_0 was chosen very high, it resulted in an insufficient number of basis functions for PML elements, decreasing the accuracy of the UWVF approximation.

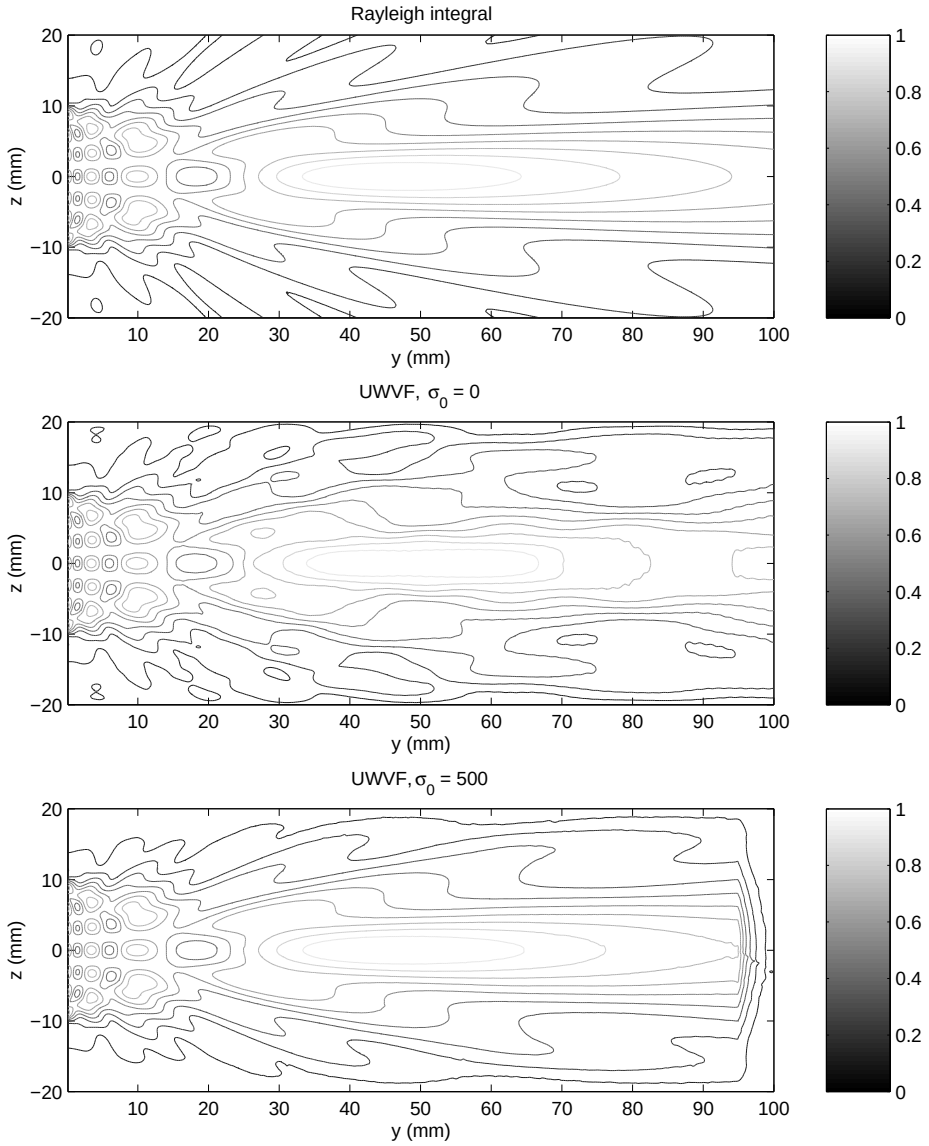

Figure 6.8: Rayleigh integral (top), the UWVF-PML approximation with $\sigma = 0$ (middle) and with $\sigma_0 = 500$ (bottom). The case of $\sigma_0 = 0$ corresponds to the zeroth order absorbing boundary condition (4.9). The PML starts when $|z| = 15$ mm and when $y = 95$ mm.

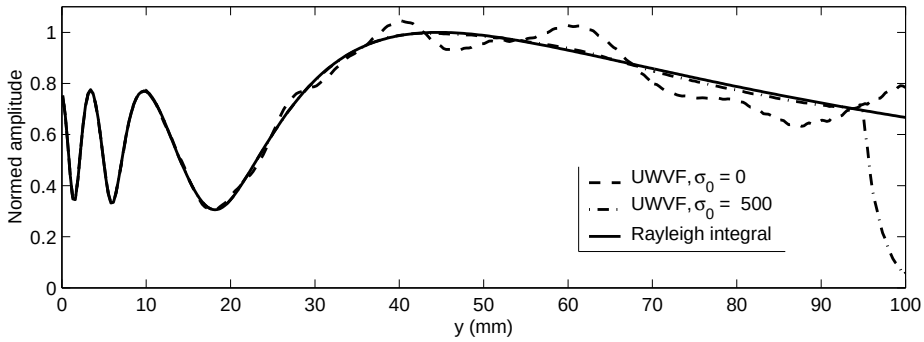

Figure 6.9: Comparison of the Rayleigh integral, the UWVF-PML with $\sigma_0 = 0$ and with $\sigma_0 = 500$ on the central axis of the source. The region $y > 95$ mm constitutes the PML.

Chapter VII

Model for measurement anomalies

A crucial issue in studies of ultrasonic acoustic and elastic wave fields is the reliability of experimental wave measurements. In medical acoustics, a typical measurement setup consists of a water tank into which a sound source, objects to be studied and a hydrophone are immersed. The excitation of the sound source and the positioning of the scanning hydrophone can be controlled by a computer. It is known that especially in the case of time-harmonic (i.e continuous wave (CW)) fields, the measurements are sensitive to measurement errors. In this chapter a method for modeling hydrophone measurements of CW ultrasound fields is introduced.

Hydrophones that utilize the piezo-electricity of polyvinylidene fluoride (PVDF) films are widely used for measuring ultrasound fields. Since the discovery of piezo-electricity of PVDF in the late 1960's, polymer hydrophones have become standards in the characterization of medical ultrasound fields [95]. PVDF has several attractive features over many piezo-materials including, for example, high sensitivity, close acoustic impedance match with water and a relatively flat frequency response. In addition, the availability of PVDF in thin (a few μm thick) sheets makes it an ideal material for hydrophones for detecting sound waves in megahertz frequencies. Various hydrophone models have been developed [95] of which, two commonly used types of hydrophones in biomedical applications are needle(probe) and spot-poled membrane hydrophones [94].

A needle hydrophone consists of a hollow metallic needle and a thin, usually 9-25 μm, PVDF film mounted onto the tip of the needle. The film contains electrodes and is backed with a material suitable for preventing reflection of waves from the inner end of the film. To obtain good spatial resolution, the diameter of the needle and the active area of the film are small, typically between 0.3-1.5 mm and 0.04-1.0 mm, respectively. Advantages and basic constructions of needle hydrophones are discussed further in [140].

A spot-poled membrane hydrophone consists of a PVDF film supported only at the edges by a mounting ring. The typical thickness of the film is 9-100 μm and diameter can be as large as 100 mm. The film may consist of single, or

more recently, two sheets of the PVDF and very thin (e.g 25 nm) layers of a non-piezo-electric material (e.g. gold and chromium). Since the membrane is nearly acoustically transparent, waves are allowed to propagate through the film, and a small, typically 0.2 - 1.0 mm diameter, active area at the middle of the membrane converts the acoustic displacements into measurable electric signal. The development and structures of membrane hydrophones are discussed in detail in [173].

Other hydrophone designs include, for example, the ellipsoidal hydrophones [179] and hydrophone arrays [103]. In the ellipsoidal hydrophones, the PVDF membrane is bonded to and backed by the end of an epoxy ellipsoid. The front end of the device is shielded electrically by a thin layer of gold. A typical size of the active element in the ellipsoidal hydrophones is 85-400 μm. A hydrophone array consists of a PVDF film of which small diameter circular regions (a typical diameter is 0.2 mm) have electrical connections. These active regions can generate individually measurable signals. The size, shape, number and spacing of the active elements can vary between different array configurations.

An assumption in acoustic measurements is that the hydrophone does not alter the acoustic field. In practice, however, it is known that in the case of continuous wave (CW) sources (i.e. time-harmonic wave fields), standing waves can be formed between the hydrophone and surrounding structures and may disturb the measurements (see [57] and [94]). Although this phenomenon has been known for a long time, little effort has been made to study it either experimentally or theoretically. The effect of the PVDF membrane hydrophone positioned at different distances from the transducer source operating in CW mode, to the field behind the membrane was examined experimentally in [167]. The transducer was driven at 2.0 - 2.25 MHz which resulted in 0-10% error to the field behind membrane, depending on the hydrophone-transducer separation. The most notable error was observed when the separation was less than 1.5 times the near-field distance. In [198] the reflection of a wave pulse from a PVDF membrane was studied in two spatial dimensions using a non-linear pseudospectral method and simulation results were compared with experimental measurements.

The aim of the following is twofold. First, to computationally determine the effect of the hydrophone on the acoustics field. Three different needle sizes and one membrane hydrophone are used in the simulations. The frequency of the wave field used in this study, varied from 0.5 MHz to 2.0 MHz. Second, simulated measurements are used to examine how the reflected waves alter the signal of the hydrophones. This part of the study is carried out for one needle and one membrane hydrophone.

7.1 Computational model

To model acoustic interaction of the CW acoustic field and a hydrophone, several assumptions have been made. First, the intensity of the acoustic field is assumed to be so low that non-linear effects on the wave field could be ignored. Second, although PVDF is a solid material and hence capable of bearing shear forces,

Table 7.1: Geometric parameters of the computation domain for needle hydrophone simulations.

f (MHz)	R (mm)	L (mm)	R_S (mm)
0.50	25.00	65.00	15.00
1.00	12.50	40.00	7.50

it is assumed that waves other than dilatational ones could be ignored. This assumption is justified since, due to the geometry of our simulation arrangement, the waves hit the PVDF film in an almost normal direction leading to relatively weak mode shear coupling. Additional approximations associated with the sound source and hydrophones are discussed in the following section.

The computational model used in this study is based on the numerical solution of the 3D Helmholtz equation (2.28) by the ultra weak variational formulation. The method is the same as discussed in Chapter 6. However, instead of using the PML, the absorbing boundary condition (4.9) is used to decrease spurious numerical reflections from the exterior boundary.

7.2 Model for the source and the hydrophone

The computational domain used in the simulations is a cylinder, the size of which varied with the frequency used in the simulations. In the needle hydrophone simulations, the acoustic field is investigated using frequencies 0.5 MHz and 1.0 MHz. These frequencies are typical for ultrasound therapy of the brain [110].

The corresponding radius and length of the cylinder are R and L, respectively, and the radius of the source R_S of the computational domain for different frequencies f are listed in Table 7.1. The radius of the source for each frequency corresponds to 5 wavelengths of the wave field in water. The source of this size is assumed to be sufficient to significantly back-scatter waves hitting the face of the source. To reduce spurious reflections from the absorbing boundary, the size of the computational domain is chosen so that the distance from the source and from the hydrophone to the artificial boundary is always several wavelengths. Although a larger computational domain might improve the accuracy, the size of the domain is limited so that time needed to compute a single wave field remains reasonable.

The source is modeled as a circular domain at the end of the cylinder. In all simulations the source is modeled as an uniformly oscillating surface. The normal derivative of pressure on the surface is

$$\frac{\partial p}{\partial n} = i\omega\rho v_n, \tag{7.1}$$

where $\omega = 2\pi f$ is the angular frequency and v_n is the normal velocity of the surface. In the UWVF method, this boundary condition is obtained by choosing $Q = 1$ and $g = -2i\omega v_n$ in (4.6). Depending on the type of hydrophone, a needle or a membrane is embedded in the domain, see Fig. 7.1. It is assumed that the PVDF

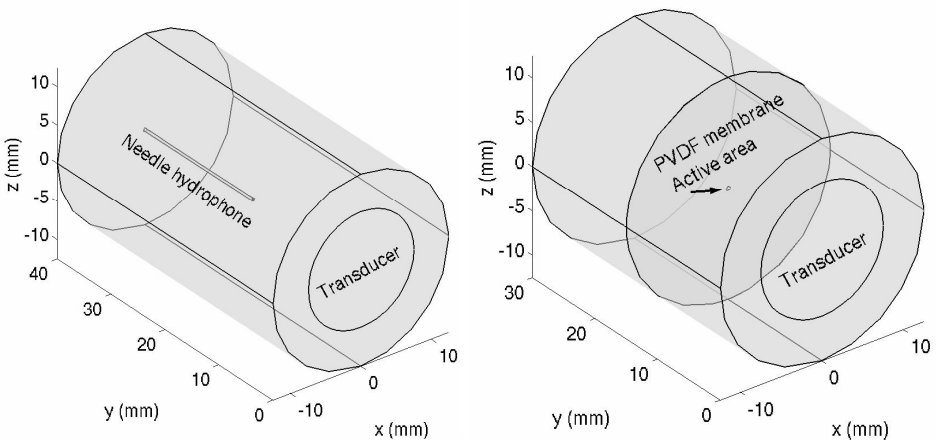

Figure 7.1: Geometries of the needle hydrophone (left) and membrane hydrophone (right) simulations. In the simulations the material surrounding hydrophones is water.

membrane hydrophone passes through the computational domain and only a part of the membrane is included to the simulation geometry. Although the membrane appears as a surface in the right hand figure, the PDVF film is a volume with a finite thickness. Correspondingly, only a thin tip of the needle hydrophone is taken into account in simulations. Other parts of the needle hydrophone system are excluded from the model.

The material properties used in this study for the PVDF are $c = 2200$ m/s, $\rho = 1780$ kg/m^3 and $\alpha = 157$ Np/m/MHz. These are in agreement with the values obtained in experimental measurements and used in other theoretical hydrophone studies (see e.g [23] and [69]). The material surrounding the hydrophone is water with $c = 1500$ m/s, $\rho = 1000$ kg/m^3 and $\alpha = 0$ Np/m.

The needle hydrophone is modeled as a thin cylinder with diameter D_N. On the tip of the needle hydrophone a 9 μm thick cylindrical domain with diameter D_F modeled the PVDF film. Detailed geometry of the tip of the needle is shown in Fig. 7.2. The thin PVDF membrane is taken into account in the model but the field inside the needle is ignored.

Three different needle hydrophones are studied. The needle and the PVDF film diameters for the hydrophones are shown in Table 7.2. The dimensions of needle and film of hydrophones are typical for currently commercially available hydrophones.

The needle, not including the PVDF film, is assumed to be perfectly rigid. Hence, on the surface of the needle the normal derivative of the pressure is zero,

Table 7.2: Needle hydrophones used in simulations.

Hydrophone	D_N (mm)	D_F (mm)
1	0.30	0.075
2	0.46	0.20
3	1.47	1.00

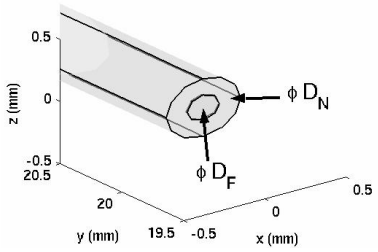

Figure 7.2: Detailed geometry of the tip of the needle hydrophone. The diameter ϕ of the needle and the PVDF film are denoted by D_N and D_F, respectively.

i.e.

$$\frac{\partial p}{\partial n} = 0. \tag{7.2}$$

(Corresponds to $Q = 1$ and $g = 0$ in (4.6)). The assumption about the perfectly rigid needle is valid since the surface of the needle is usually made of steel or brass, which have at least 20 times higher acoustic impedances than water.

The backing material behind the PVDF film is assumed to be absorbing. The absorbing boundary condition (4.9) is used on the inner surface of the film.

Although in this study the impenetrable needle surface (7.2) is assumed and the field inside the backing material is ignored, it is possible, in practice, that elastic waves can be generated in the needle hydrophone. For example, it was shown in [154] that surface elastic waves can be induced on a brass backing behind a PVDF film. However, the piece of brass used in that study was significantly larger ($D_N = 50$ mm) than the needles in the present study. On the other hand, the results in [154] suggested that the leaky waves, originating from the surface waves, had only a minor effect compared to reflected and diffracted waves.

The membrane hydrophone is modeled as a single homogeneous 25 μm thick layer of PVDF. To simplify the simulations (and to enable the generation of the tetrahedral mesh), the non-piezo-material layers are not included in the model. The simulations for the membrane hydrophone are computed for the frequency 2.0 MHz. The geometric parameters for the mesh at 2.0 MHz are $R = 6.25$ mm, $L = 20.0$ mm and $R_S = 3.75$ mm. In [167], experimental measurements using 2.0 MHz sources are done to study errors associated to membrane hydrophone measurements of CW fields. The simulated data of this study can be compared

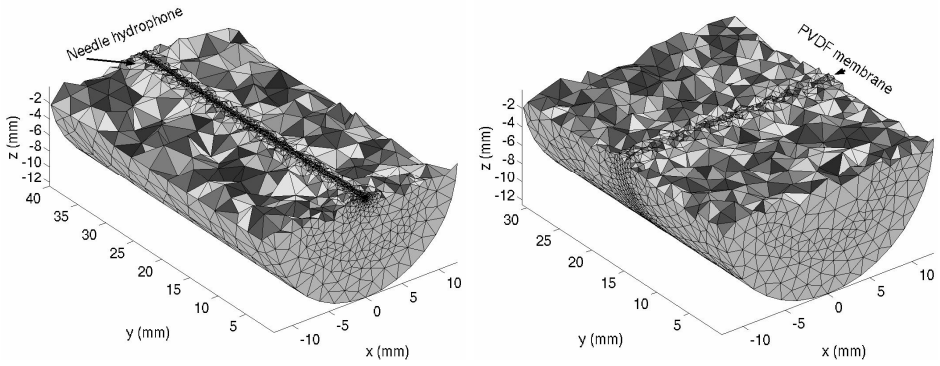

Figure 7.3: Cross-sections of typical meshes used in needle hydrophone (left) and membrane hydrophone (right) simulations. To ensure maximal accuracy of the UWVF approximation between the needle and the source, relatively small tetrahedra are used in the mesh between the tip of the needle and the transducer.

with those measurements. As in the case of the needle hydrophones, the size of the computation domain is limited by reasonable computation time.

To evaluate the signal produced by the hydrophone, an active region with a diameter of 0.50 mm is defined on the surface of the membrane. The signal is obtained by integrating the pressure field over this active area. The electric signal generated by a hydrophone is proportional to the pressure on the front face of the membrane [69].

The simulated hydrophone measurement for both needle and membrane hydrophone is carried out in three steps. First, a mesh with the hydrophone at the desired location is generated. Second, the UWVF approximation of the field is computed. And third, the signal for the hydrophone is obtained by integrating the UWVF approximation over the front face of the PVDF film.

Typical meshes used in the simulations are shown in Fig. 7.3. Depending on the simulation, the number of elements in the mesh is between 35 000 and 80 000. Due to the requirement of detailed geometry of the hydrophones, the element size within a mesh varied considerably. Consequently, the number of basis functions for a single element in the UWVF scheme varied between 1 and 130.

7.3 Simulations

7.3.1 Needle hydrophone

The effect of the needle hydrophone on the field under measurement is studied by comparing simulated pressure fields in the absence and presence of the hydrophone. The overall fields (i.e the fields with and without a hydrophone) are normalized to the maximum value of the field without a hydrophone in the region shown.

In the results section, the fields with and without hydrophone are referred to as p and p_w, respectively. To study the distortion caused by the hydrophone, the difference field $p_w - p$ is also presented. To show what portion of the incident field reflects from the tip, the difference field $p_w - p$ is normalized to the amplitude of the incident field at the location of the tip.

The field scattered by a needle hydrophone is studied as a function of distance from the tip of the needle to the source d. Pressure amplitude distributions are shown for hydrophone 3 with $D_N = 1.47$ mm and the frequency $f = 0.5$ MHz in Fig. 7.4. The distance d varied from 10 to 30 mm. Corresponding difference fields along the acoustic axis of the source are presented in Fig. 7.5. A notable pattern of standing waves can be seen in all three cases, although the amplitude of the waves diminishes with the increasing distance between the hydrophone's effective element and the surface of the radiating source.

The effect of needle diameter on the field distortion for fixed frequency $f = 1.0$ MHz and needle distance $d = 10$ mm are studied as a function of the hydrophone size. The pressure amplitude fields in Fig. 7.6 show that only the thickest hydrophone causes significant distortion. It is noteworthy that the diameter of the hydrophone 3 ($D_N = 1.47$ mm) is almost equal to the wavelength ($\lambda = 1.5$ mm) of the field. The plot along the acoustic axis in Fig. 7.7 confirms that the two thinnest needles have only a negligible effect on the field between the needle and the source.

Simulated hydrophone measurement

The measurement for hydrophone 3 ($D_N = 1.47$ mm) and the frequency $f = 0.5$ MHz is simulated. The hydrophone is scanned along the acoustic axis of the source.

A comparison between simulated measurements with an ideal hydrophone and with a real hydrophone is shown in Fig. 7.8. The ideal hydrophone measurement shows the pointwise value of the pressure field without a hydrophone. The fields are normalized with the mean pressure amplitude in the y-axis.

7.3.2 Membrane hydrophone

The membrane hydrophone simulations in this study are limited to frequency $f = 2.0$ MHz. Similarly to the needle hydrophone studies, all results shown are normalized, however, now with the maximum amplitude in water in the absence of the membrane.

A periodic anomaly is shown in the field (Figs. 7.9 and 7.10). The membrane is located at the distance of $d = 10$ mm.

Simulated hydrophone measurement

Finally, the simulated membrane hydrophone scan along the acoustic axis of the 2.0 MHz source from 10.0 to 15.0 mm with 0.1 mm spacing is shown in Fig. 7.11. Furthermore, Fig. 7.12 shows the relative error in the pressure amplitude at the point 18 mm from the transducer as a function of the location of the scanning membrane hydrophone. The distance from the transducer to the hydrophone is

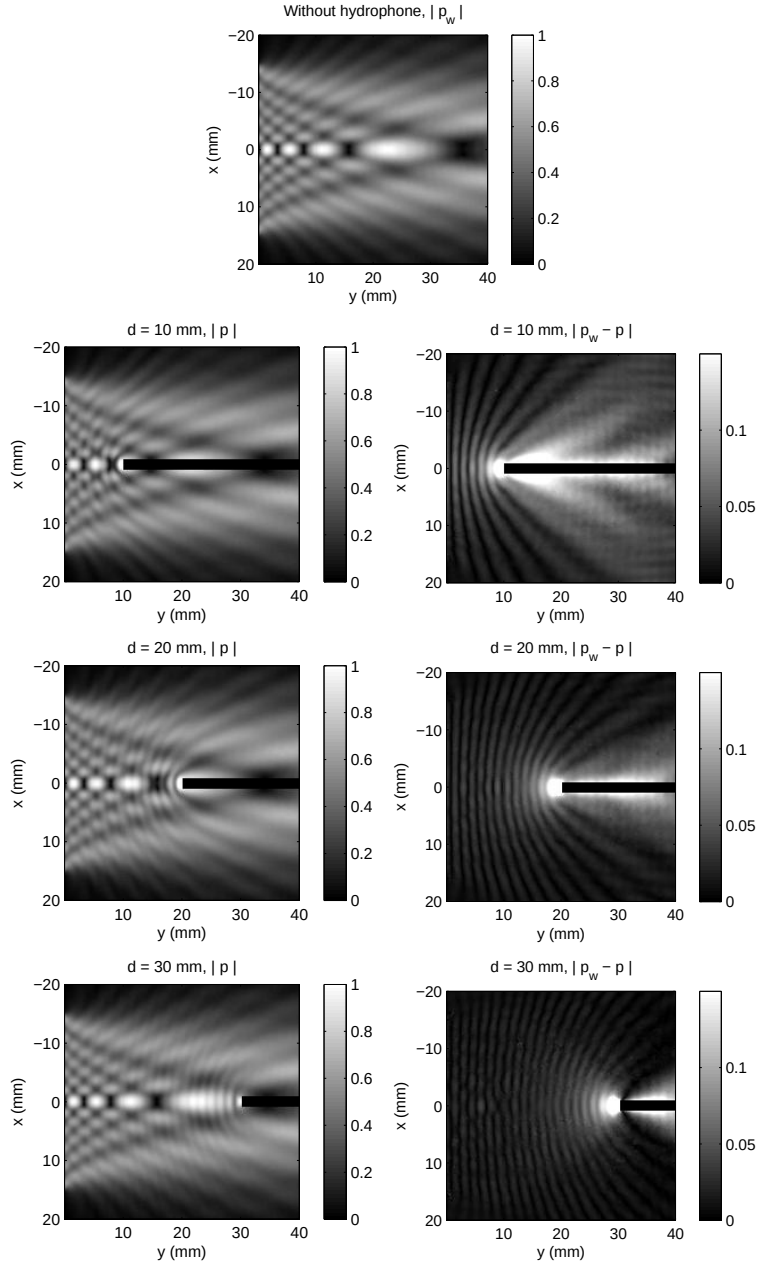

Figure 7.4: Scattering from the needle hydrophone 3 with $D_N = 1.47$ mm for different distances d from the source. Left column shows the fields with the hydrophone. Right column shows the anomalies due to the hydrophone. The results are computed for the frequency $f = 0.5$ MHz.

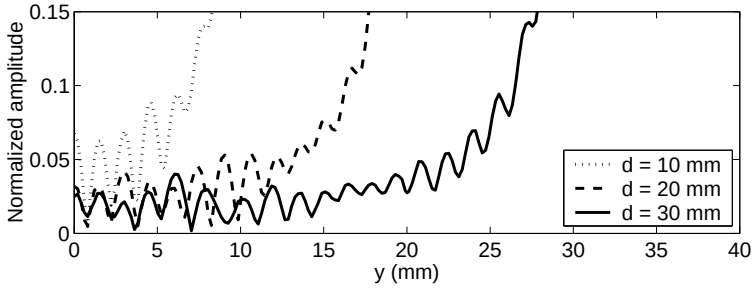

Figure 7.5: The difference pressure amplitude fields $|p_w - p|$ along the acoustic axis of the source for different needle - source distances ($f = 0.5$ MHz, $D_N = 1.47$ mm).

divided by the near-field distance 18.56 mm. The relative error in the pressure amplitude is shown compared to the value of the field at the same point without the hydrophone. The error is shown also in comparison to the mean value of the field at different transducer-hydrophone separations. The measured error presented in the same figure is extracted from Figure 12 of [167].

7.4 Discussion and conclusion

In this chapter, the 3D ultra weak variational formulation (UWVF), developed in the previous sections, was used for analyzing distortions in continuous-wave fields caused by needle- and membrane hydrophones. Furthermore, simulated measurements for the hydrophones were computed. The frequency span of the simulations was 0.5 - 2.0 MHz which is typical for the ultrasound therapy. In many therapeutic applications of ultrasound continuous waves are used and therefore it is essential to understand possible anomalies related to the pressure field measurements.

In addition to the modeling approximations, the numerical procedure used in this study has two main sources of error. First, by limiting the study to the relatively small computation domain and by using the approximate absorbing boundary condition (4.9) on the exterior boundary of the domain, minor spurious numerical reflections of the waves are generated from the boundary into the cylinder. The reflections originate mainly from the incident field of the source. Therefore, they are eliminated from the difference field $p_w - p$, Second, the UWVF method using relatively coarse computational meshes has a limited numerical accuracy which for problems studied here, means an error of the order 0.1-1.0 %. This estimate of the accuracy was obtained by comparing two solutions for the same geometry and frequency, computed in different meshes. In both cases, the method for choosing the number of basis functions was the same as described in Chapter 5.

For needle hydrophones, the major distortion in continuous-wave measure-

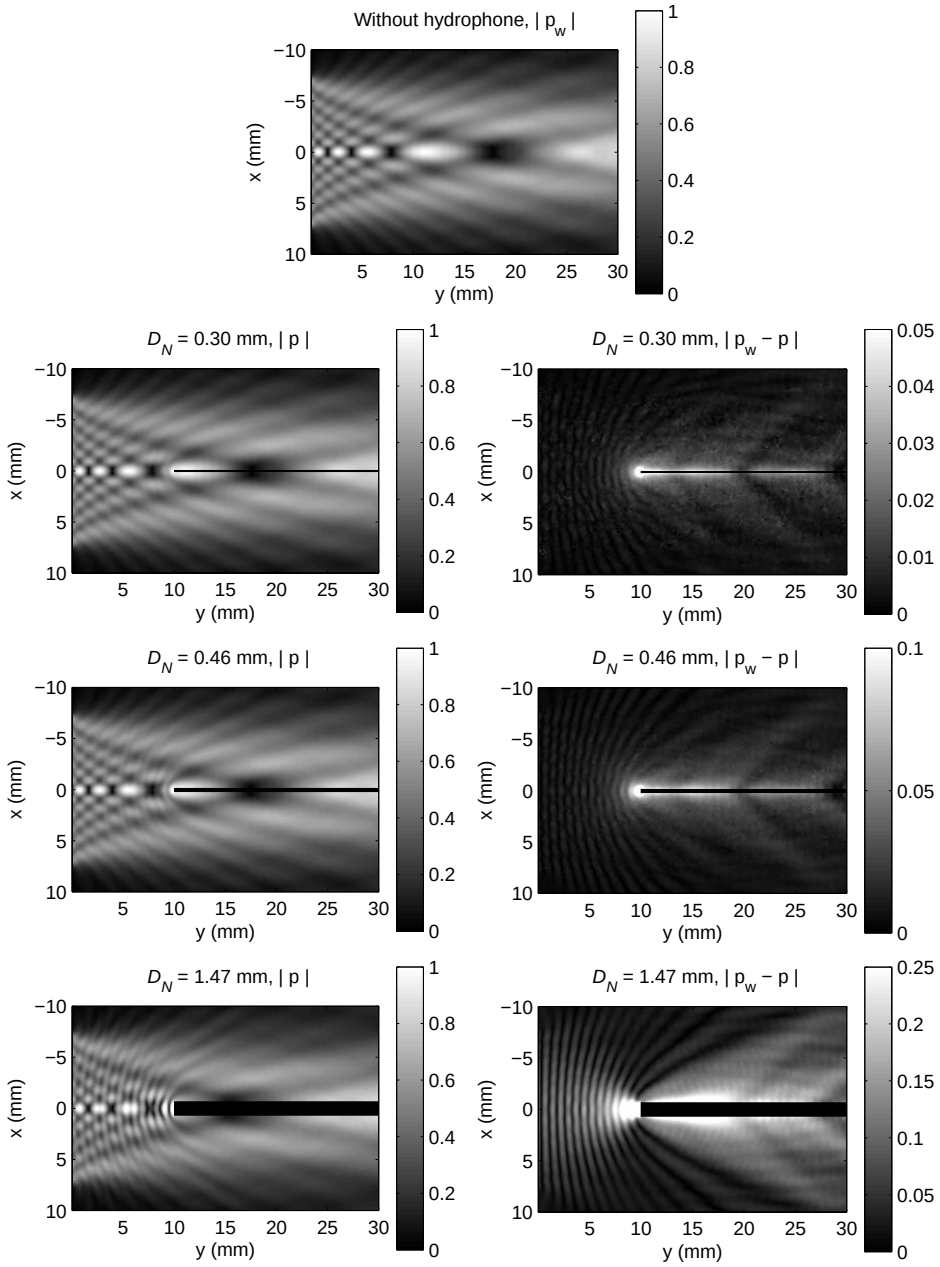

Figure 7.6: Effect of the needle diameter D_N to the scattered field. The frequency is $f = 1.0$ MHz and distance from the source to the tip of the needle $d = 10$ mm. Left column shows the field with the hydrophone and right column presents the anomalies due to the hydrophone.

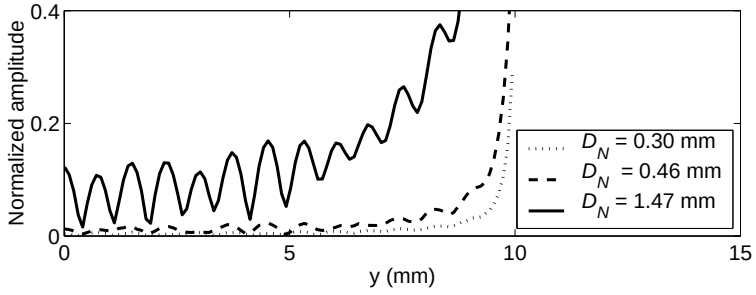

Figure 7.7: The difference fields $|p_w - p|$ along the acoustic axis of the source for different needle sizes ($f = 1.0$ MHz, $d = 10$ mm).

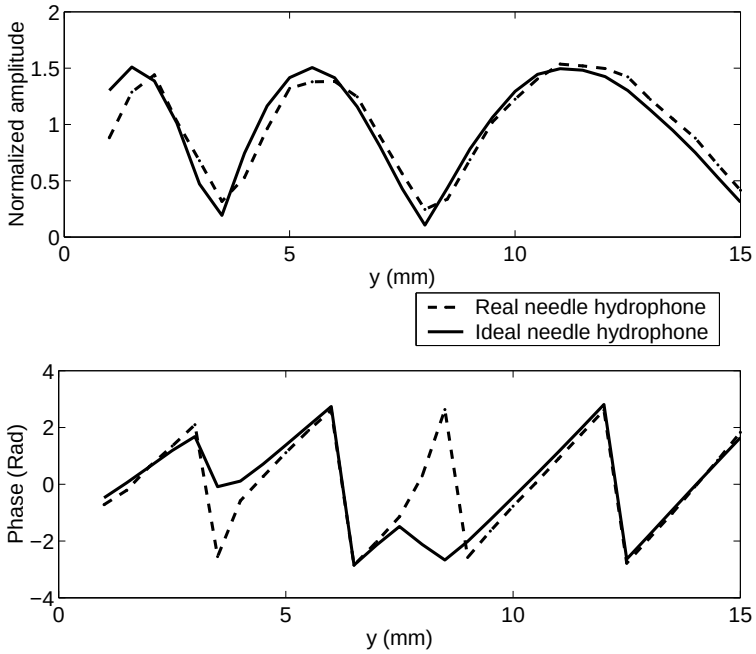

Figure 7.8: Comparison of the ideal and real simulated needle hydrophone measurements on the acoustic axis of the circular source with $f = 0.5$ MHz. The diameter of the needle hydrophone is $D_N = 1.47$ mm.

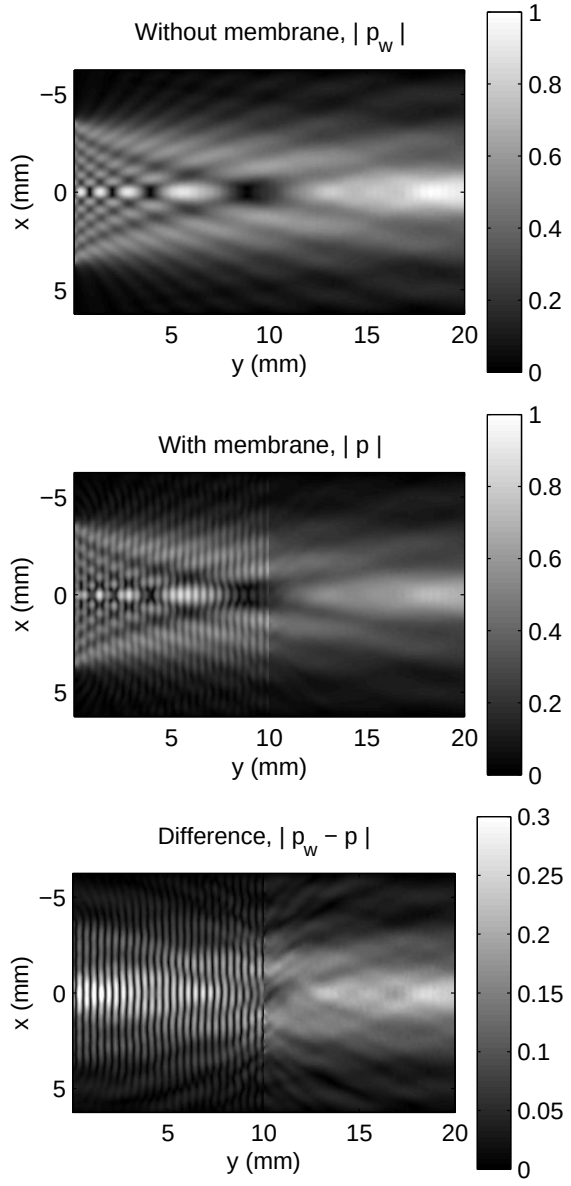

Figure 7.9: The effect of the membrane hydrophone to the pressure amplitude distribution. The distance from source to membrane is $d = 10$ mm and frequency is $f = 2.0$ MHz.

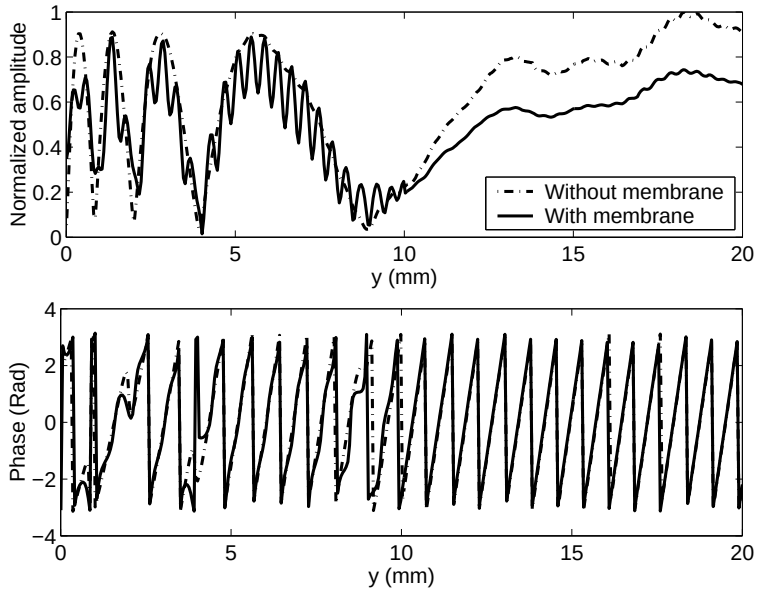

Figure 7.10: Comparison of the fields with and without membrane for the frequency $f = 2.0$ MHz. The membrane is at plane $y = 10$ mm.

ments is most likely due to the back-scattered waves from the tip of the hydrophone. Some of these waves interfere with the incident field. Standing wave patterns are formed between the needle and the source element (or a structure between the needle and the source). Obviously, the amplitude of the field reflected from the tip of the hydrophone is proportional to the amplitude of the incident field at the measurement point (i.e. at the location of the tip).

The results for the needle hydrophones suggested that scattering from the tip of the needle becomes observable when the diameter of the needle is over half of the wavelength. Although a notable standing wave field was observed for the frequency $f = 0.5$ MHz and hydrophone 3 at the distance $d = 10$ mm in Fig. 7.4, the simulated measurement with the same hydrophone in Fig. 7.8 closely follows the profile of the field at the acoustic axis. Therefore, for the needle hydrophones it is not evident that the difference in the field and the measurement was only due to standing waves between the needle and the source, particularly, since the discrepancy did not have the same clear periodic structure as was observed in the simulated measurement for the membrane hydrophone. Other possible sources of error in measurements include, for example, the diffraction effects that are studied in detail in [76]. The diffraction effects emerge since the hydrophone with the finite size active film is used to measure the "point" value of the acoustic field.

In the case of membrane hydrophones, both the field between the transducer and the membrane; and the simulated signal of the hydrophone revealed a half

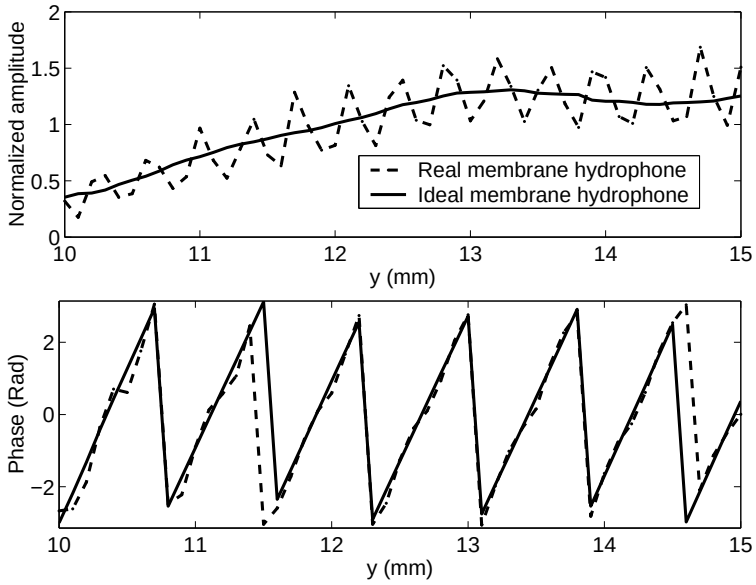

Figure 7.11: Comparison of the measurements with an ideal hydrophone and the real membrane hydrophone on the acoustic axis of the circular source for $f = 2.0$ MHz.

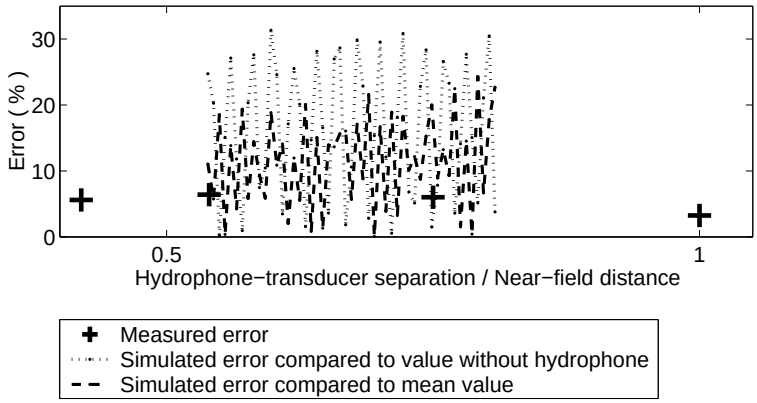

Figure 7.12: The relative error in the pressure amplitude at a fixed distance (18 mm) from the 2.0 MHz transducer as a function of the transducer - membrane hydrophone separation. The membrane hydrophone scanned distances 10-15 mm with 0.1 mm spacing. The measured errors are from [167].

wavelength periodic distortion in comparison to the field without the membrane. The relative amplitude of the disturbance was about 20%. For the 2.0 MHz transducer, the field at a fixed distance from the source behind the membrane hydrophone was simulated. This case imitates the experimental measurements performed in [167]. The relative error of the field in simulations was 0-30 % when compared with the pressure amplitude at the same spot without the hydrophone. The error in comparison to the mean value of the field at the same point at different transducer-hydrophone separations was 0-20 %. In [167], under 10% errors were observed by using a second membrane hydrophone at a fixed distance from the transducer. Hence, the model seems to predict the magnitude of the error reasonably well although the simulated errors were slightly over-estimated in comparison to the experimental measurements.

The difference between the simulations and experimental measurements has several possible reasons. For example, the model used in this study did not include the changes in the output of the source due to the standing waves [15]. And the second membrane used to measure errors in [167], interacts also with the wave field and therefore may cause additional anomalies. A thorough validation of the simulations would require a new set of measurements that would allow more detailed comparison of the measured data with simulated results.

The simulations were computed only for a planar circular source. Since the amplitude of the scattering from the hydrophone is proportional to the amplitude of the field at location of hydrophone, it is obvious that strong distortion may result in, when focused CW fields are measured near the focal spot. In addition, this study was limited only to a region near the hydrophone (i.e only part of the needle or membrane was considered) which naturally eliminates possible standing waves from surrounding structures (e.g. from the walls of the measurement tank or from the holder of the hydrophone).

The study was limited to only a relatively small number of hydrophones and a simplified hydrophone model was used. An improved model could include the elastic properties of the hydrophones, multi-layered structures and electric characteristic of the PDVF film. These have been used in one dimensional modeling of the membrane hydrophones [69]. An aim of this study, however, was to include more detailed characterization of the incident fields and hydrophone geometries. To limit the extend of the study, the simulations were computed only for the needle and membrane hydrophones but a similar simulations should be possible also for the ellipsoidal or array hydrophones.

Chapter VIII

Transmission through layered structures

In the previous chapter, anomalies due to hydrophones in continuous-wave ultrasound fields were analyzed using the 3D Helmholtz-UWVF model. A similar model is used in this chapter to simulate ultrasound transmission through layered structures. The simulations are compared with experimental measurements. The problems analyzed here, are of particular interest in focused ultrasound surgery (FUS) through intact skull. As was discussed in the introduction, the aim in FUS of the brain is to generate a constructive interference of waves at a desired location in the brain.

A main obstacle for FUS of the brain arises from the strong acoustic mismatch between soft tissues (skin and brain) and the skull. Typical values of density for skin and brain are 1200 kg/m^3 and 1030 kg/m^3, respectively [68] . Whereas the speed of sound in the same tissues are 1498 m/s and 1516-1575 m/s. A comparison with the density and speed of sound of the skull (1797 kg/m^3 and 2653 m/s averaged values from [66] used in [185]), indicates strong scattering of sound from interfaces between the skull and soft tissues. Further difficulties in the delivering of acoustic energy through the skull arise from the strong absorption of sound in the bone ($\alpha_{\text{skull}} = 50$ Np/m at 0.5 MHz [66]). These two factors allow only a small portion of the acoustic energy to be transmitted through skull which necessitates the use of large-area phased arrays [39].

Due to the complex geometry of the skull, waves from different elements of the phased array propagate to the focus through parts of skull which may have a large thickness variation. To be able to accurately model the phase shifts caused by the skull, one must take into account the detailed geometry of the skull. In practice, the anatomy of the head can be obtained from computer tomography (CT) or magnetic resonance (MRI) images.

In addition to the shape of the skull, recent studies have shown that the accuracy of the ultrasound simulation can be improved by taking into account the internal structure of the cranium [37]. CT-imaging methods provide a feasible means to reconstruct the internal composition of the bone [7, 38, 50].

A simplified model of the skull consists of three layers which are the outer

and inner ivory tables; and the middle diploe layer of cancellous bone. The measurements in [66] show that the denser surface layers have higher speed of sound (2900 m/s) but significantly lower absorption (6 Np/m at 0.5 MHz) than the inner trabecular bone layer for which the corresponding values are 2500 m/s and 85 Np/m.

A common feature of previous modeling studies for ultrasound transmission through skull has been their limitation to pulsed waves which typically consist of 1-30 sinusoidal cycles. The small number of cycles has allowed the use of time-domain simulation methods, such as the FDTD method which become increasingly time consuming for longer pulses (see Section 3.2.1) or projection and ray methods [38, 185] which also suffer from computational complexity if multiple reflections of the sound are taken into account. However, standing waves, especially between the transducer and skull may have a notable effect on the transmitted field [36].

In this chapter simulations are carried out for continuous waves but instead of using *ex vivo* skull specimens, the propagation medium consists of plastic layers immersed in water. By using plastic plates one avoids the uncertainties in the acoustical properties and detailed geometry of the medium that are associated with biological tissues [192]. The simplified experimental setup is the first step in the validation of the full-wave method for modeling of CW ultrasound fields in complex media.

The simulations of this chapter are computed with the 3D UWVF solver of the Helmholtz equation in an inhomogeneous medium. As an improvement over the simulations of Chapter 7, the computations of this section are conducted utilizing the PML method for reducing spurious numerical reflections. Furthermore, attention is given to a more realistic modeling of the velocity distribution on the transducer.

The chapter is organized in the following way. In the first section an inverse problem theoretic approach for estimating the normal surface velocity of the transducer is introduced. The method uses experimental measurements to determine the oscillation amplitude and phase on the transducer which will be later used for modeling the source for the UWVF scheme. Section 8.2 outlines the experimental setup for measuring the transmitted field. The simulation procedure is summarized in Section 8.3. Measured and simulated fields are compared in Section 8.4 and the chapter is concluded in Section 8.5.

8.1 Inverse problem for the velocity distribution

The simulation studies of Section 6.3.3 and Chapter 7 analyzed fields emitted by an oscillating surface with a uniform normal velocity distribution. Although this kind of ideal model is widely used in acoustic simulations they are rarely sufficient for modeling fields from real ultrasound transducers. In [104], experimentally measured fields from polyvinylidene fluoride (PVDF) and lead zirconate titanate (PZT) transducers were compared with theoretical models. They observed that PVDF sources had a good agreement with the model that assumed a uniform velocity distribution on the transducer. However, in the case of the PZT elements,

marked amplitude variations on the transducer were found. A notable variation in the amplitude and phase of transducers surface velocity pattern of CW sources was also observed in [175].

Since the experimental measurements of this thesis are conducted using PZT elements, the model must take into account the specific velocity pattern of the transducer. Typically, the surface velocity is reconstructed from the measurements that are made in a plane parallel to the transducers surface in the front of the transducer. In the projection methods [35, 175, 183], the measured field is Fourier transformed and the field can be easily projected backward to the source plane. The pressure field in that plane can be resolved using the inverse Fourier transform.

In the equivalent phased array method (EPAM), the transducer is assumed to consist of a "phased array" of small elements [62]. Each element oscillates with its own amplitude and phase. Then, the field in the measurement plane is obtained as a discrete Rayleigh integral over the fictitious elements. As will be shown later, the pressure field in the measurement plane can be written in the form of a matrix equation in which the vector of complex valued velocities for each element is multiplied by a matrix arising from the discrete Rayleigh integral. Obviously, if the pressure field is known, the velocity vector can be obtained as the inverse of the same matrix. In EPAM, the inversion of the system matrix is computed as the pseudo-inverse which produces the minimum norm solution for the source. A similar technique was first introduced to predict driving amplitudes and phases of phased arrays for ultrasound hyperthermia [58, 59].

The surface velocities obtained from the both methods have been shown to lead to a reliable reconstruction of the pressure field if rather strict measurement conditions are fulfilled. Namely, the field must be measured with relatively dense spacing and the measurement plane must be large enough to contain sufficient amount of information of the pressure field.

As was noted in [62], the surface velocity distribution obtained via EPAM is not the same as the real particle velocity. Rather the method gives the excitation source which produces similar acoustic field as the measured one. The EPAM method is also sensitive to the input pressure field, that is, pressure data from different measurement planes may lead to different velocity distribution.

From the methodological point of view, the source reconstruction belongs to the class of *inverse problems*. In the forward problem, the task is to resolve the resulting pressure fields from the known surface velocity distribution. Consequently, the inverse problem can be defined as finding the sound source if the pressure field (or a part of it) is known. Particularly since a small variation in the measured pressure data may result in large changes in the surface velocity, the inverse problem is said to be *ill-posed*. A common property of ill-posed problems is that the system matrix is ill-conditioned. Standard techniques for treating the ill-conditioned inverse problems are discussed for example in [86]. Typically, the ill-conditioned problem is replaced with a nearby well-posed problem, and the problem is said to be regularized.

The inverse problem approach for the acoustic source reconstruction has been used for example in [178]. In that study the aim was to reconstruct the source

of a tire noise. Due to the complex geometry of the tire, the forward modeling was made using the boundary element method (BEM). The inverse problem was solved with *Tikhonov regularization*.

The formulation of the forward problem in this thesis is the same as in the equivalent phased array method. However, to relax the restrictions of the measurement conditions, a similar regularization technique as in [178] is used to invert the matrix equation.

In Section 6.3.3 the field from the uniformly oscillating surface was represented using the Rayleigh integral (6.6). Assuming that the surface S consists of finite sized elements $S = \cup_{j=1}^{N} dS_j$, the discrete Rayleigh integral for the pressure at point $r = (x, y, z)$ can be written as

$$p(r) = \sum_{j=1}^{N} v_{n,j} \left(\frac{i\omega\rho}{2\pi} \frac{e^{i\kappa|r-r_j|}}{|r-r_j|} dS_j \right), \tag{8.1}$$

where r_j is the centroid of the element dS_j and $v_{n,j}$ is the normal velocity at the point r_j.

Let the field be measured at points $r_m, 1 \leq m \leq M$. Then, the pressure field at the measurement points $p(r_m) = p_m$ can be solved from the matrix equation

$$p = Hv_n,$$

where

$$p = \begin{pmatrix} p_1 \\ p_2 \\ \vdots \\ p_M \end{pmatrix}, \quad H = \begin{pmatrix} h_{1,1} & h_{1,2} & \dots & h_{1,N} \\ h_{2,1} & h_{2,2} & \dots & h_{2,N} \\ \vdots & \vdots & \ddots & \vdots \\ h_{M,1} & h_{M,2} & \dots & h_{M,N} \end{pmatrix} \quad \text{and} \quad v_n = \begin{pmatrix} v_{n,1} \\ v_{n,2} \\ \vdots \\ v_{n,N} \end{pmatrix},$$

and where

$$h_{m,j} = \frac{i\omega\rho}{2\pi} \frac{e^{i\kappa|r_m-r_j|}}{|r_m-r_j|} dS_j.$$

The discrete approximation is accurate if the size of the elements dS_j is small compared to the wavelength.

In the equivalent phased array method [62], the velocity distribution on the transducer is obtained using the pseudo-inverse of the matrix H. As noted earlier, this produces the minimum norm solution for the velocity v_n which may differ from the real velocity distribution. Therefore, in this thesis, a Tikhonov regularization [190] is used. Hence, the velocity vector v_n is obtained as the solution of

$$v_n = (H^*H + \gamma^2 I)^{-1} H^* p, \tag{8.2}$$

where H^* refers to conjugated transpose of the matrix H and γ is the so-called regularization parameter.

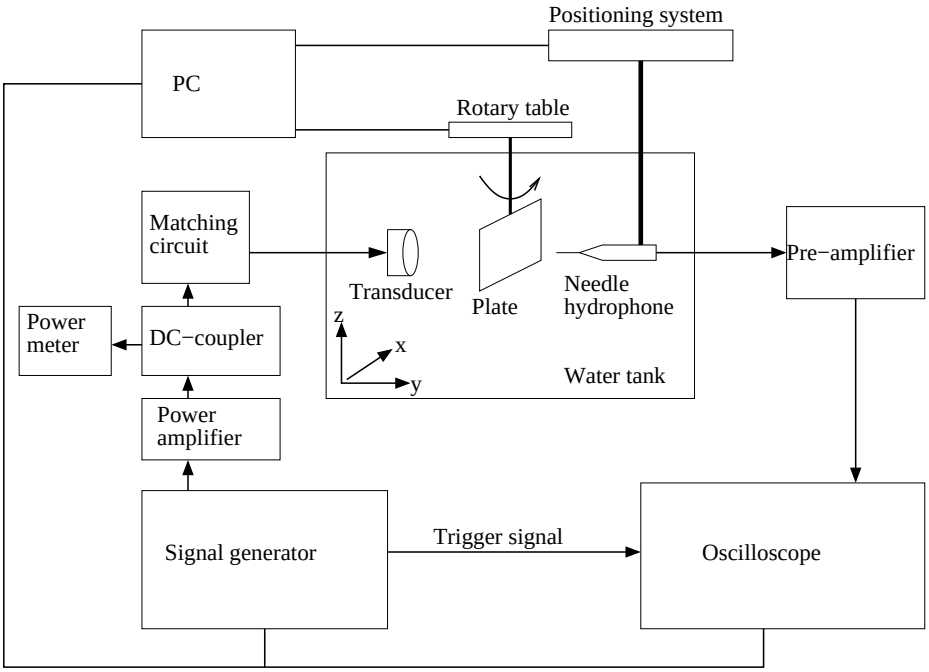

Figure 8.1: The experimental setup.

8.2 Measurement setup

The experimental measurements have two aims. On one hand, the measured data is needed to reconstruct the velocity distribution on the transducer. The estimated velocity is then used for the realistic modeling of the source in transmission simulations. On the other hand, the measurements of the transmitted fields for the plastic targets are required for the forthcoming comparison with the simulated results.

Experimental measurements for this thesis have been made by Jason White at the Focused Ultrasound Laboratory in the Brigham and Women's Hospital in Boston, MA, USA. Experiments are conducted in a tank filled with deionized and degassed water. The dimensions of the tank are $450 \times 910 \times 420$ mm and the walls of the tank are padded with rubber to prevent spurious reflections. A schematic illustration of the experimental setup is presented in Fig. 8.1.

The 30 mm diameter circular planar transducer is made of PZT-4 and it is operated at frequency $f = 531$ kHz. The sinusoidal transducer signal is generated with a waveform generator (Wavetek 395, Ismaning, Germany) and amplified with a power amplifier (ENI A150, Rochester, NY, USA). A power meter (Agilent E4419E, Palo Alto, CA, USA) is used to monitor the input power of the transducer. The angle of the plastic layers in front of the transducer are controlled with a motor

Table 8.1: Acoustic parameters for the plastics at the frequency 531 kHz

	c (m/s)	ρ (kg/m^3)	α (Np/m)
Water	1498	1000	0
Polycarbonate	2185	1187	19.4
Plexiglas	2770	1236	13.7
Rubber	1520	1089	31.7

driven rotary table (Welmex, Bloomfield, NY, USA).

Two types of layered plastic plates are used. Plate 1 is a single layer (thickness 11.8 mm) of polycarbonate and Plate 2 consists of a 6.0 mm thick layer of rubber sandwiched between two 3.1 mm thick plates of plexiglas. Plates are large enough that practically the whole sound beam from the transducer propagates through the plate. The material properties of the plastic used for the plates and water are listed in Table 8.1. All properties were measured in-house, except the absorption coefficients for polycarbonate and plexiglas, which were obtained from [102]. The three layer structure imitates the layered model of the human skull since it consists of a softer and strongly absorbing material between thin layers of a harder material.

The transmitted field is measured using a 0.2 mm diameter PVDF needle hydrophone (Precision Acoustics SN762, Dorchester-Dorset, UK). The simulations of Chapter 7 showed that the diameter of the needle is small enough in order to avoid standing waves between the transducer and the needle. The hydrophone is moved in the tank using a a stepping motor controlled 3D positioning system (Welmex, Bloomfield, NY, USA). The pre-amplified signal of the hydrophone is recorded by a digital oscilloscope (Tektronix, Beaverton, OR, USA). The wave generator, data acquisition and the positioning of the plate and hydrophone are computer controlled by a PC. The recording of the signal is triggered to start after a specific delay from the launch of the transducer signal. Several cycles of hydrophone signal are recorded and the time-domain data is Fourier transformed into the frequency-domain using a PC.

A detailed geometry of plate and measurement planes are shown in Fig. 8.2. The transducer is in the $y = 0$ plane and wave propagate to the direction of the positive y-axis. The front face of a plate is located at 45 mm distance from the transducer. The distance from the transducer to the center of the measurement planes is 85 mm. The plates are rotated in the (x,y)-plane. The measurement planes have the origin at the point (0, 85 ,0) mm. The (x,y)-plane is in $[-15, 15] \times [70, 100]$ mm. The measurements in this plane are used for comparison with the simulated fields.

Another 30 $\times$ 30 mm measurement plane is in the (x,z)-plane spanning over the region $[-15, 15] \times [-15, 15]$ mm. The data from this plane is used for the reconstruction of the transducers surface velocity. In this case the field is measured without the plastic plates. In the both planes, the fields are scanned with 0.5 mm spacing.

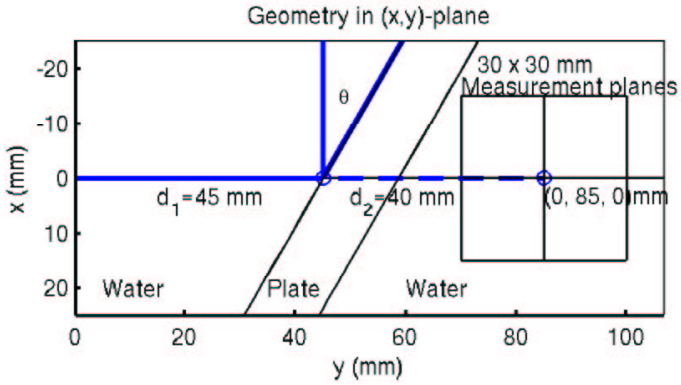

Figure 8.2: Rotation of the plate and measurement geometry. The field is emitted by a planar circular trasducer with the diameter 30 mm. The transducer is located in the $y = 0$ plane so that the center of the transducer is at the origin. The front face of the plate is located at 40 mm distance from the transducer and the center of measurement planes is at 85 mm distance from the transducer. The square region shows the (x, y)-measurement plane. The rotation angle of the plate is denoted by θ.

8.3 Simulation procedure

The 3D Helmholtz-UWVF model used in this Chapter is essentially the same as introduced previously in Chapter 6. However, as an exception to the previous simulations, the BiCGStab iterations are truncated when the relative residual reaches a value below 10^{-4}. The computational region of interest has dimensions $40 \times 102 \times 40$ mm. All faces, except the transducer face $y = 0$, are surrounded by a 5 mm thick PML. The decay parameter in the PML is set to $\sigma_0 = 400$. A cross-section of the simulation geometry is the same as in Fig. 8.2, however, the 5 mm PML surrounding the computational domain is not shown in the figure. Since the plates pass through the computational domain, they continue at the same angle in the PML region. The PML decay parameter in the plate is same as in water $\sigma_0 = 400$.

As in the previous chapter (see Section 7.2 for details), the transducer is modeled as an oscillating surface on which the normal derivative of the pressure is

$$\frac{\partial p}{\partial n} = i\omega\rho v_n. \tag{8.3}$$

However, unlike in the previous chapter where the normal velocity amplitude v_n was constant throughout the transducer surface, it can now be a function of location $v_n = v_n(x, z)$.

The planar circular transducer in Fig. 8.2 is located in the $y = 0$ plane and it is centered at the origin. Hence, the complex normal velocity v_n on the transducer surface S can be written in the form

$$v_n(x, z) = A(x, z)e^{-i\phi(x,z)},$$

where $A(x, y)$ is the amplitude and $\phi(x, z)$ is the phase.

The spatially varying amplitude and phase are computed as the solution of the inverse problem (8.2). The implementation of the velocity is carried out in two steps. First, the complex valued velocity is solved from (8.2) in a relatively dense set of points on the transducer surface. Second, the amplitude and phase of the velocity are representend in a parametrized form which simplifies the implementation of the velocity to the UWVF code.

The measurements of Section 8.4 will show that the amplitude on the circular transducer used in this study can be approximated with a radial Gaussian distribution

$$A = A_0 e^{-\frac{R^2}{2\sigma^2}}, \tag{8.4}$$

where A_0 is a real constant, $R = \sqrt{x^2 + z^2}$ and σ is the standard deviation. The phase is parametrized using a fifth order polynomial

$$\phi(x, z) = \sum_{\ell=0}^{5} \sum_{m=0}^{5-\ell} B_{\ell,m} x^\ell z^m. \tag{8.5}$$

Theoretical analysis of Gaussian sources in [80] showed that they have notably smoother near field behavior than ideal piston oscillators.

The standard deviation σ for the amplitude and the constants $B_{\ell,m}$ for the phase are obtained by a non-linear and linear, respectively, fitting to the reconstructed surface velocity data. Since the aim of the simulations is to compare the relative pressure amplitudes, the amplitude parameter A_0 is set to $A_0 = 1$.

To simplify the integration of the source terms in (4.6), each triangular element face on the transducer surface is divided into four subtriangles. Then, the constant amplitude and phase, determined by the values at the centroid, are used in each subtriangle.

8.4 Comparison between measurements and simulations

In Fig. 8.3 the experimentally measured pressure field in the plane $y = 85$ mm without a plate is shown. This data is used as input data to the inverse problem (8.2) for reconstructing the surface velocity distribution of the transducer. For the discrete Rayleigh integral (8.1), the transducer surface is divided into 2378 elements on which the discrete velocity is sought. On the other hand, the field in the plane $y = 85$ mm is measured in 30×30 region with 0.5 mm spacing which corresponds to 3721 measurement points. The Tikhonov regularized solution of the over-determined matrix system is computed using $\gamma = 2.2 \cdot 10^5$ as the regularization

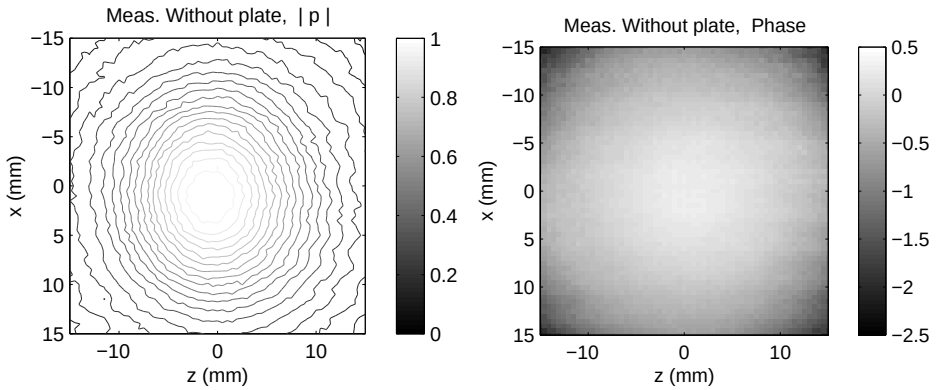

Figure 8.3: The measured field without a plate in the plane $y = 85$ mm.

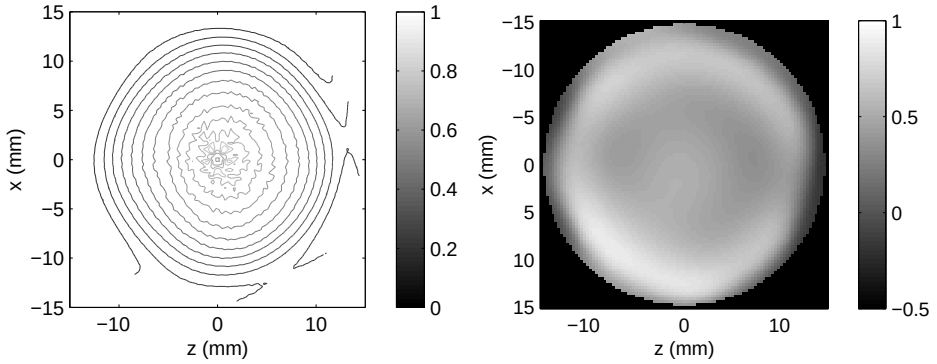

Figure 8.4: Amplitude (left) and phase (right) of the complex valued normal velocity amplitude on the transducer. The velocity is obtained as the solution of the inverse problem (8.2).

parameter. The parameter is chosen by trial and error. Namely, at low values of γ the solution in unstable until the increase in γ over a certain value stabilizes the solution. Further increase in the regularization parameter tends to force the solution toward a constant value of $v_{n,j} = 0$ for all $j = 1, ..., N$ since this minimizes the side constraint $\gamma||v_n||^2$ [86]. The parameter $\gamma = 2.2 \cdot 10^5$ corresponds to the value which gives stable but non-constant solution for the velocity field v_n.

The normalized solution for the velocity distribution is shown in Fig. 8.4. The amplitude and phase are shown at a dense set of points on the transducer plane. In order to use a spatially varying velocity in the UWVF, the amplitude and phase are parametrized as explained earlier in this chapter.

Results indicate that the amplitude has almost a radially Gaussian shape which

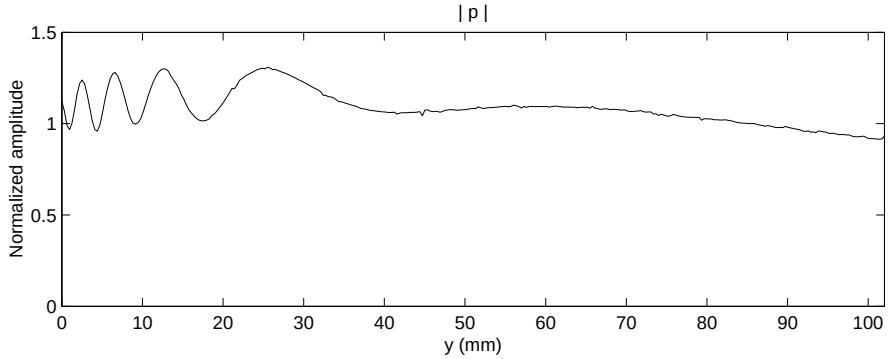

Figure 8.5: The simulated amplitude on the central axis of the transducer in water using the parametrized form of the velocity profile of Fig. 8.4.

justifies the Gaussian parametrization (8.4) for the UWVF method. More precisely, the non-linear fitting gives a value $\sigma = 7.4$ mm for the standard deviation. The behavior of the phase is more complicated and therefore the high-order polynomial representation (8.5) was chosen. Even higher order polynomials could be used but in this case, the LS-fit to the phase data bacame unstable when the order was increased.

The amplitude of the UWVF approximation of the pressure field on the central axis of the transducer is presented in Fig. 8.5. The field is computed using the parametrized surface velocity that is resolved from the measurements in the plane $y = 85$ mm. In comparison to the ideal piston model (see e.g. Fig. 7.10), the near-field behavior of the field is smoother due to the Gaussian velocity distribution.

The simulated and measured fields in the (x, y)-plane without a plate are shown in Fig. 8.6. To simplify the comparison between the amplitudes of the simulated and measured fields, all fields from here on are normalized with the amplitude at the point (0,85,0) mm in the absence of a plate.

The effect of the plastic plate on the transmitted field is analyzed next. In Fig. 8.7 the UWVF solution inside the non-PML region is shown for Plate 1. The fields are presented for different rotation angles of the plate.

A detailed comparison between simulated and measured field is shown in Figs. 8.8-8.11. The amplitudes of the wave field inside the non-PML region for Plate 2 are shown in Fig 8.12. The comparison of the simulated fields with experimental measurements are presented in Figs. 8.13-8.16.

For both plates, the best agreement between simulations and measurements is obtained when the plate is rotated in $\theta = 10$ deg. angle, Figs. 8.9 and 8.14. In the case of Plate 1 with $\theta = 0$ deg., the amplitude of simulated field is over-estimated, see Fig. 8.8. On the other hand, for Plate 2 with $\theta = 0$ deg., there is a minor dicrepancy in phases, see Fig. 8.13. Although, the amplitudes start to deviate in $\theta = 20$ deg., see Figs. 8.10 and 8.15, the phases have a rather good agreement.

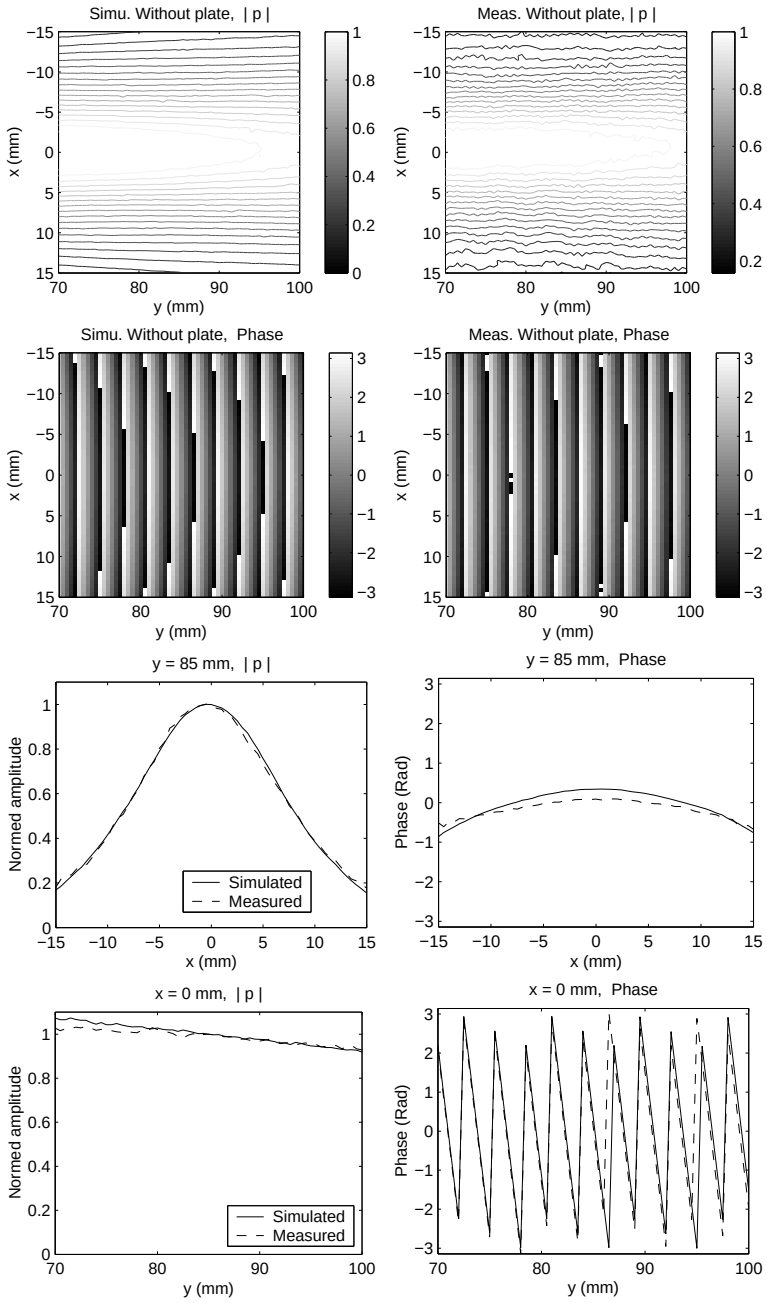

Figure 8.6: Comparison of the measured and simulated fields in the absence of a plate.

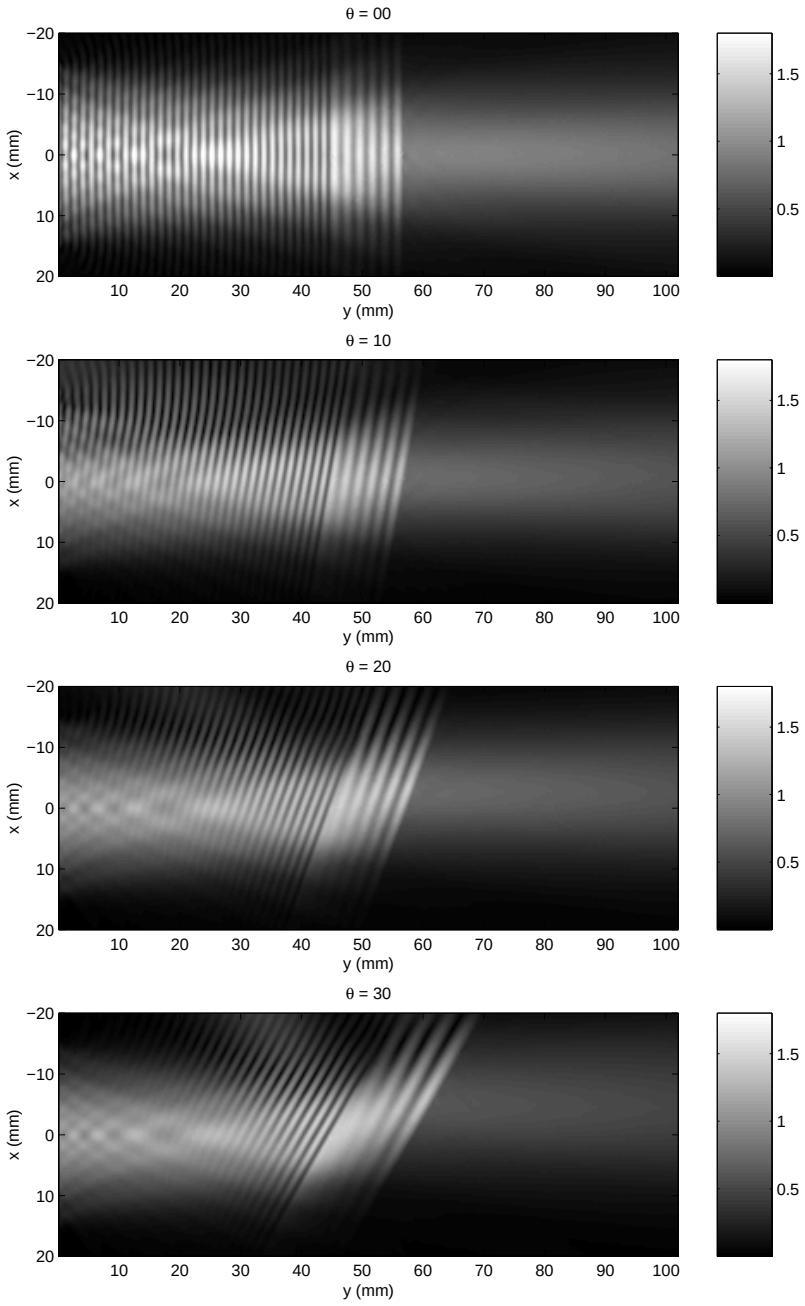

Figure 8.7: Simulated pressure amplitudes in the non-PML region in the (x, y)-plane for the different angles of the single layer plate.

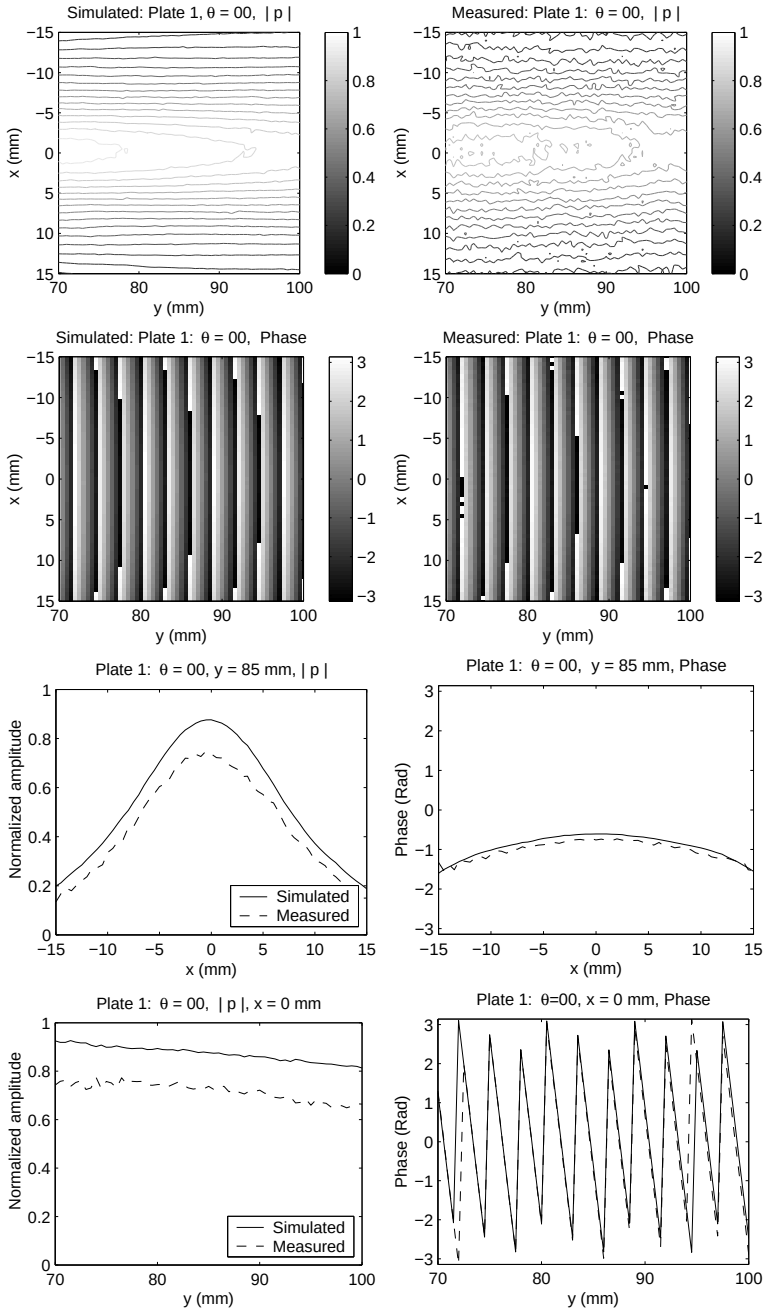

Figure 8.8: Comparison of the measured and simulated fields for the single layer plate in $\theta = 0$ degrees angle.

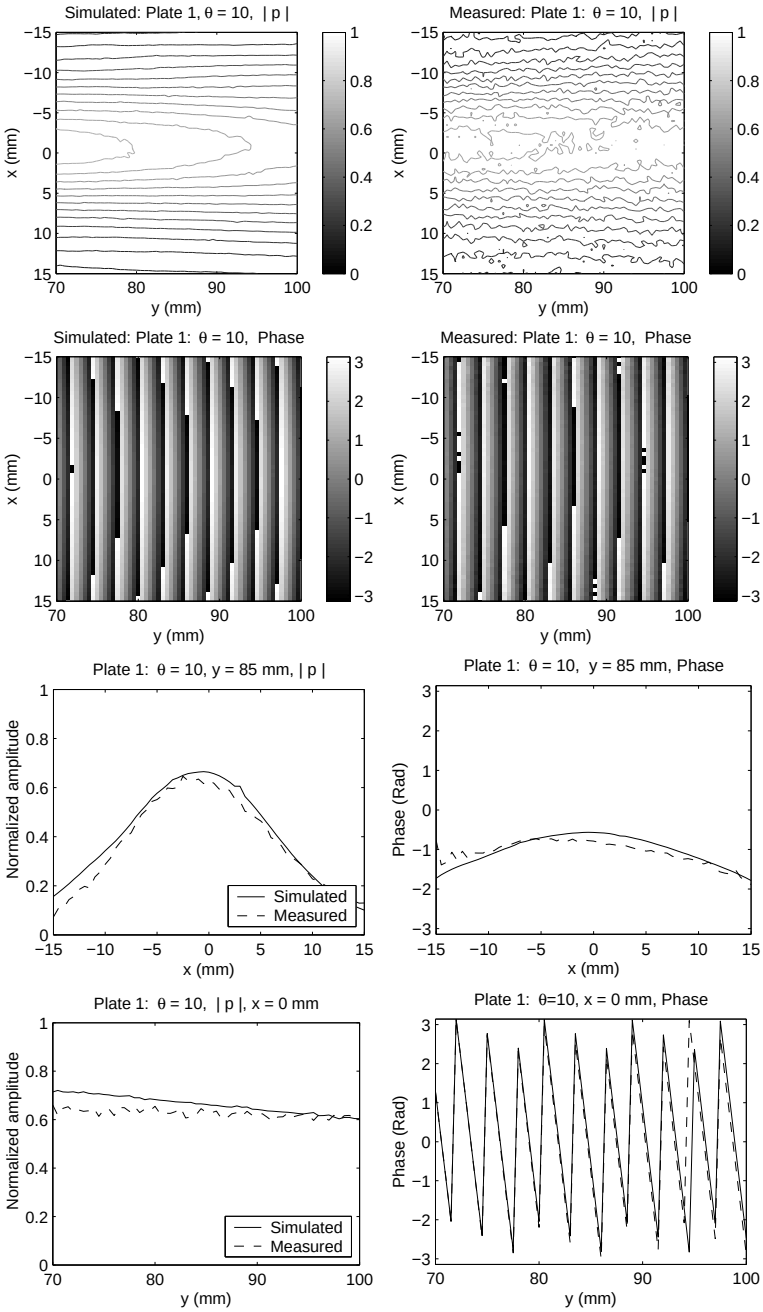

Figure 8.9: Comparison of the measured and simulated fields for the single layer plate in $\theta = 10$ degrees angle.

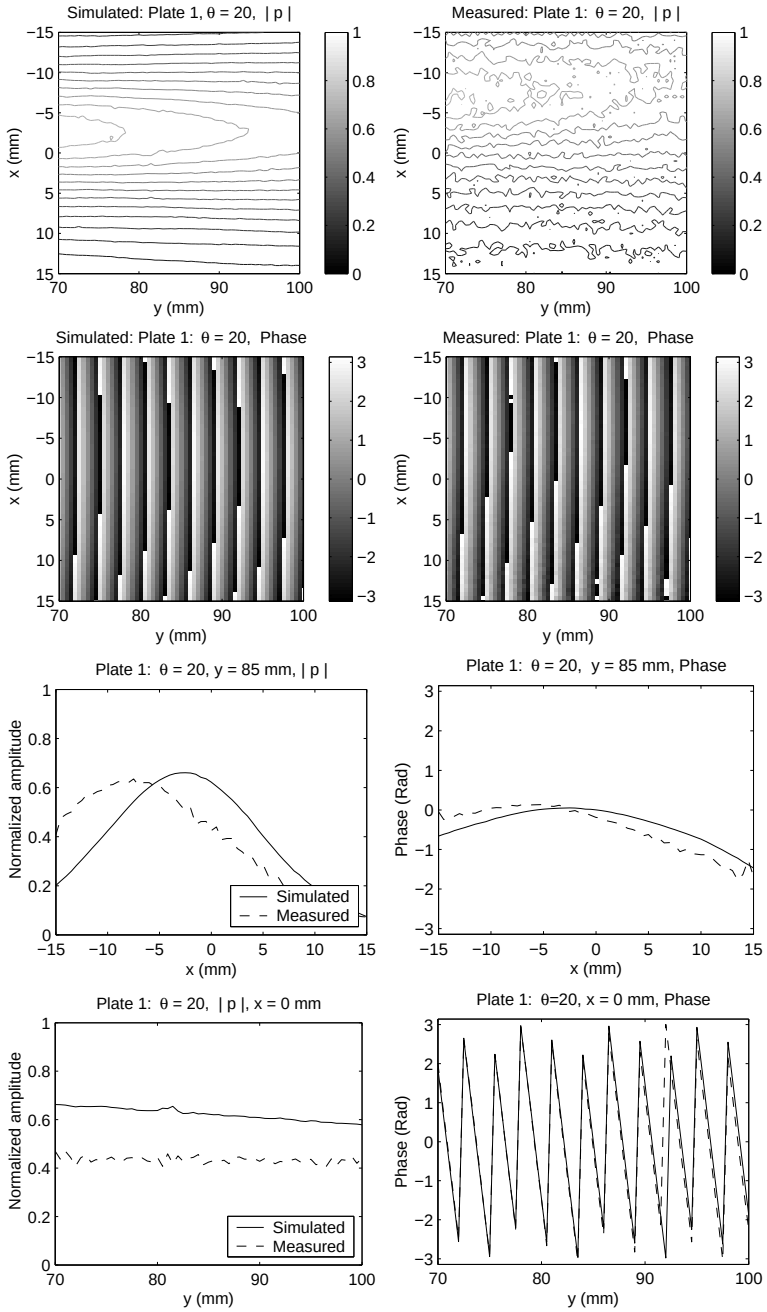

Figure 8.10: Comparison of the measured and simulated fields for the single layer plate in $\theta = 20$ degrees angle.

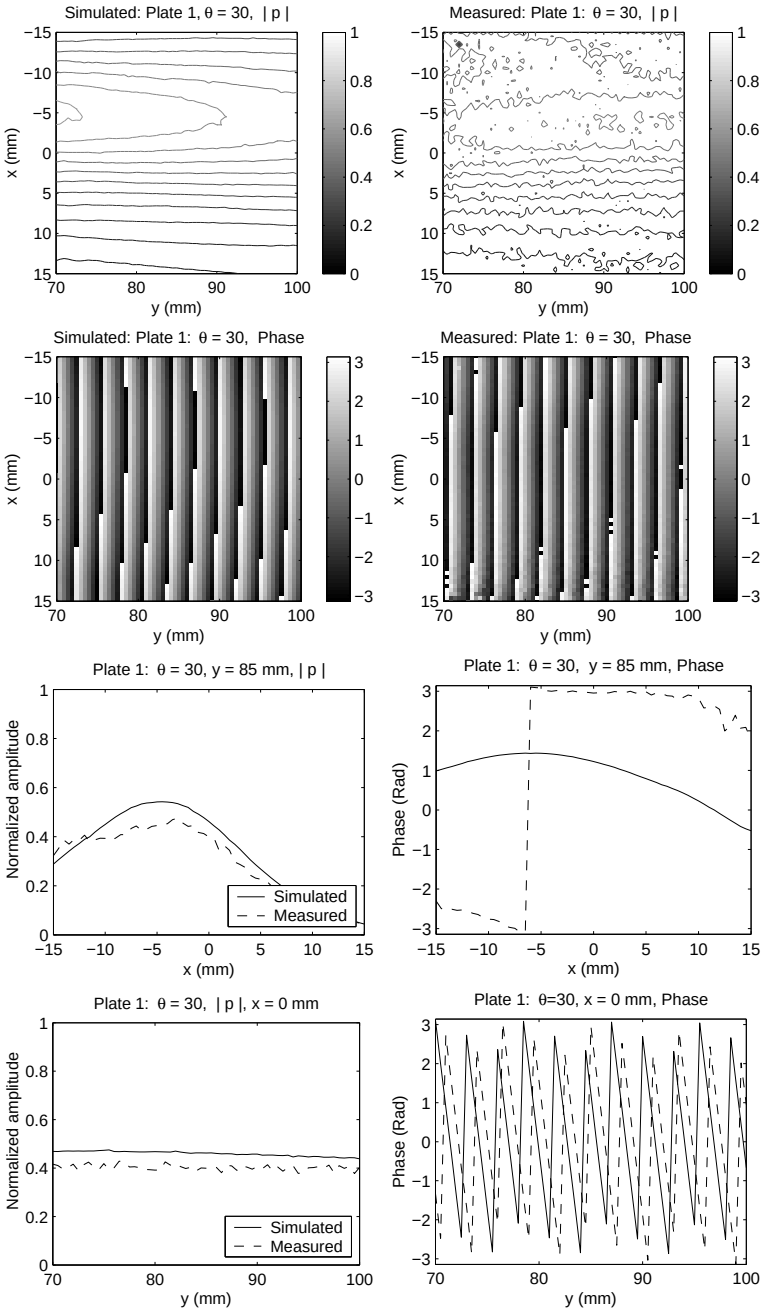

Figure 8.11: Comparison of the measured and simulated fields for the single layer plate in $\theta = 30$ degrees angle.

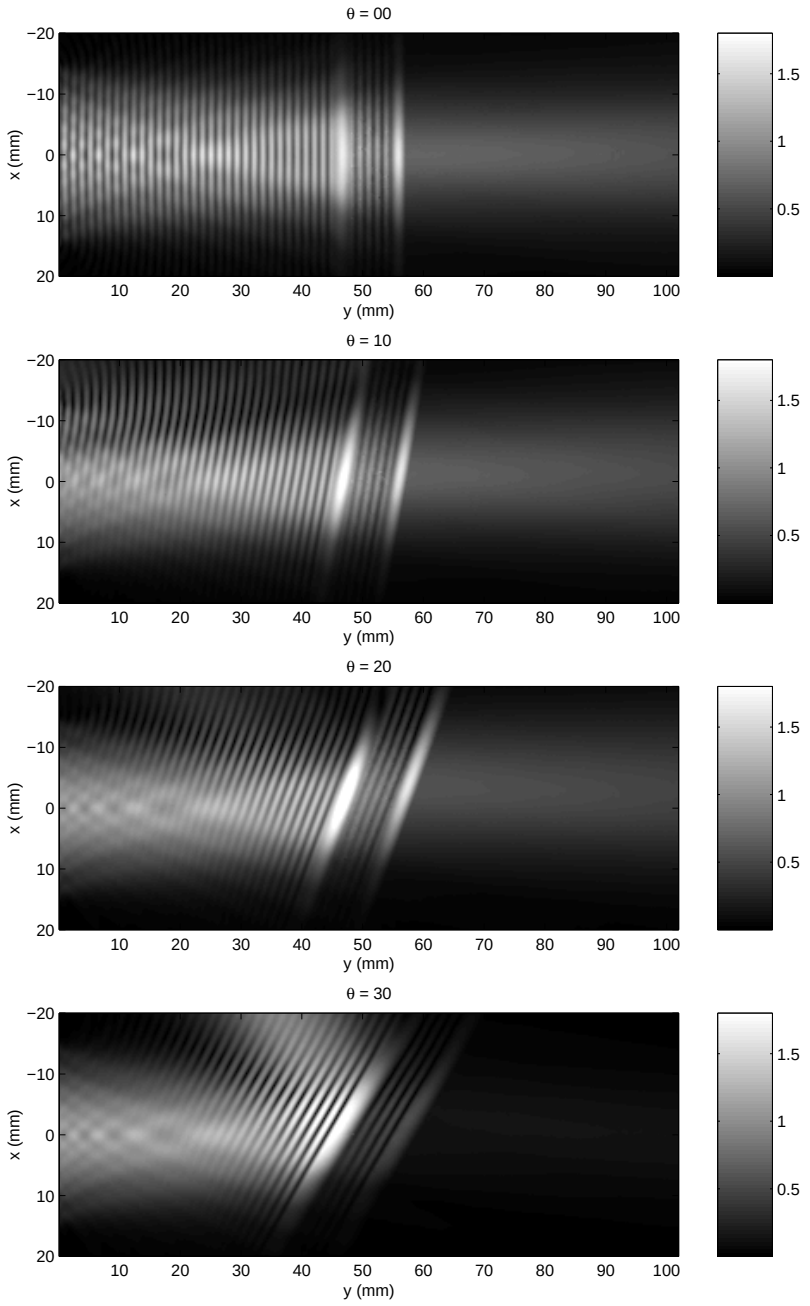

Figure 8.12: Simulated pressure amplitudes in the non-PML region in the (x, y)-plane for the different angles of the three layer plate.

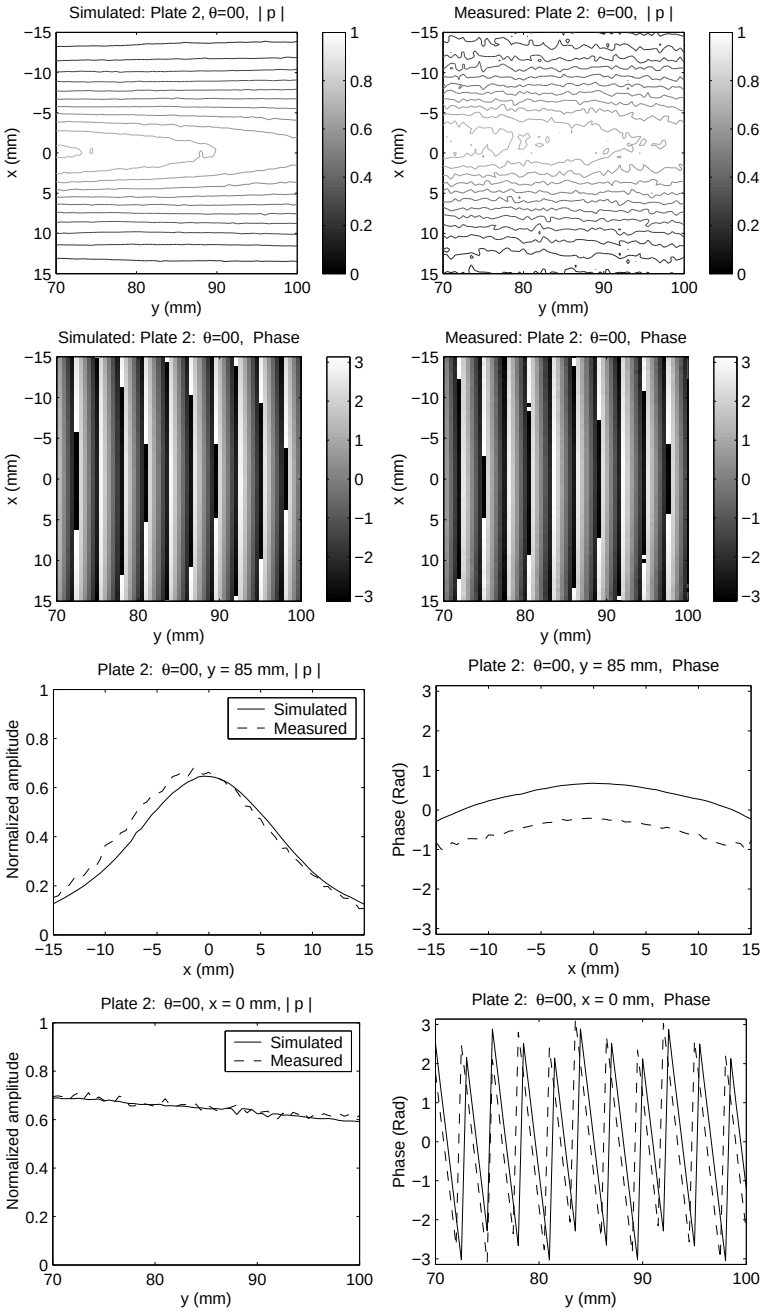

Figure 8.13: Comparison of the measured and simulated fields for the three layer plate in $\theta = 0$ degrees angle.

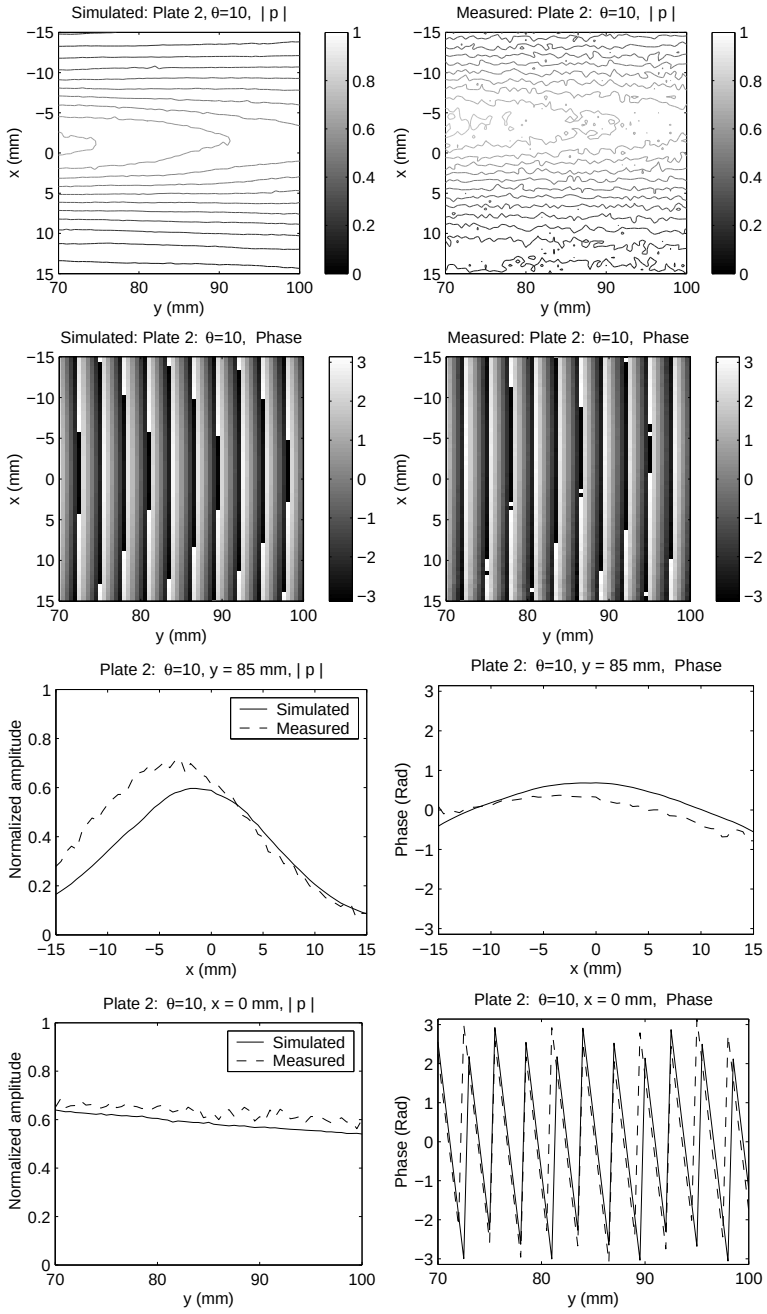

Figure 8.14: Comparison of the measured and simulated fields for the three layer plate in $\theta = 10$ degrees angle.

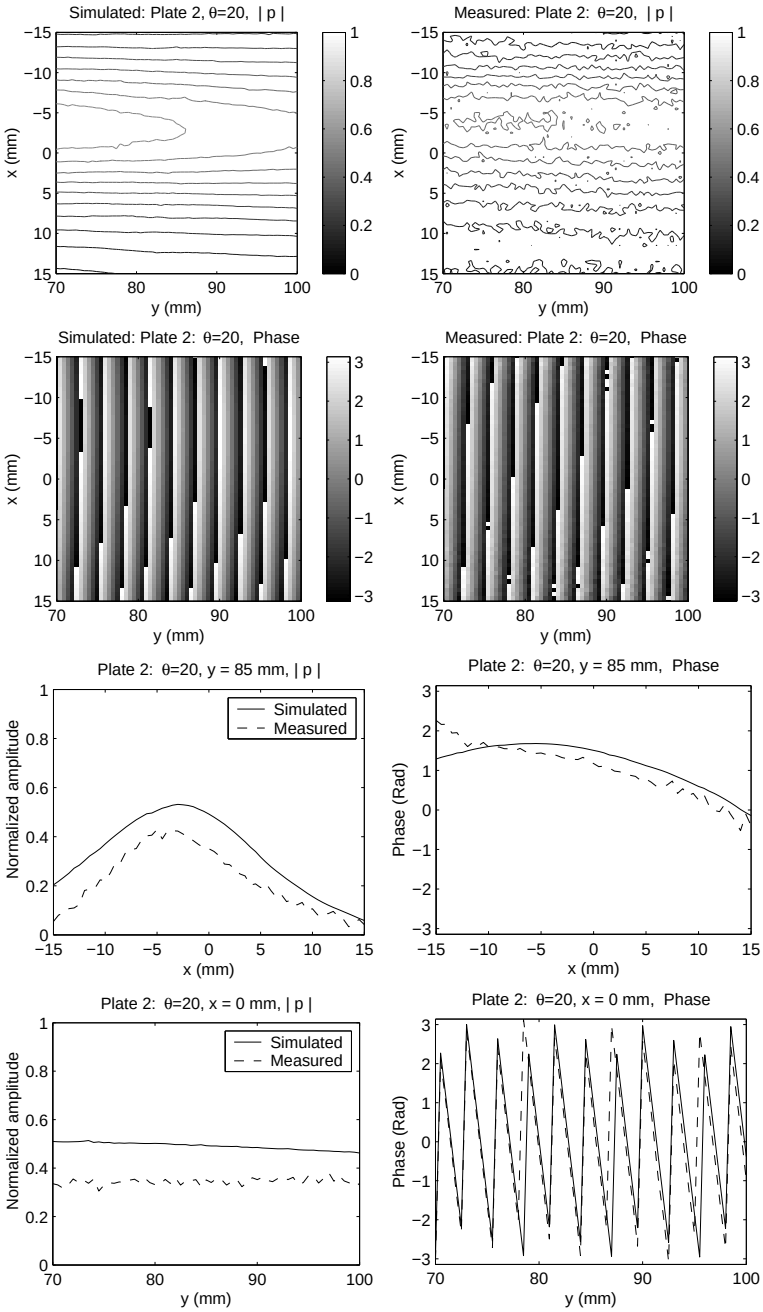

Figure 8.15: Comparison of the measured and simulated fields for the three layer plate in $\theta = 20$ degrees angle.

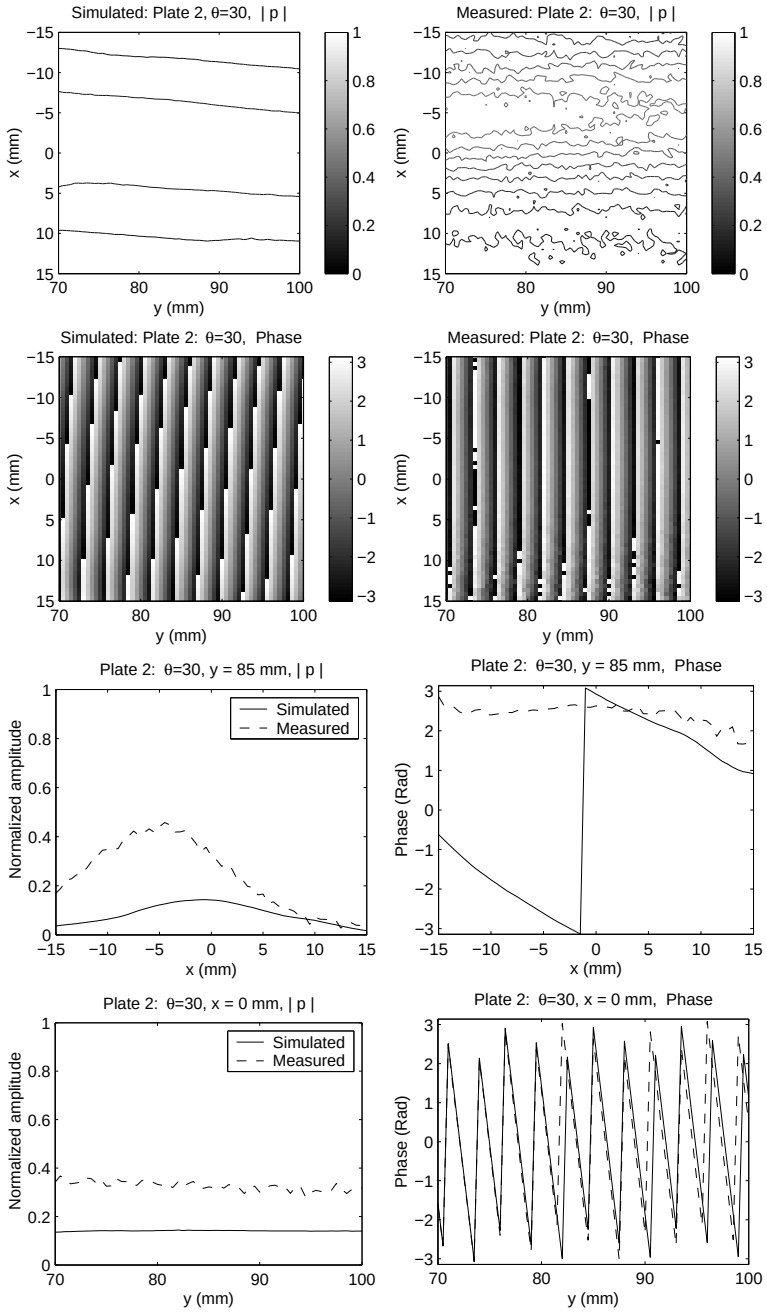

Figure 8.16: Comparison of the measured and simulated fields for the three layer plate in $\theta = 30$ degrees angle.

For the largest angle $\theta = 30$ deg., the error either in the amplitude or in the phase is notable, see Figs. 8.11 and 8.16.

8.5 Discussion and conclusions

In this chapter, the feasibility of using the UWVF model for the Helmholtz equation was investigated for simulating continuous-wave ultrasound fields in inhomogeneous media. The computational simulations were compared with experimental measurements in the case of ultrasound propagation through plastic plates. Two plates were used. Plate 1 was a single layer of polycarbonate. Plate 2 consisted of a layer of rubber sandwiched between layers of plexiglas. The sound field was generated using a planar circular PZT transducer operating at 531 kHz frequency. Transmitted fields behind the plates were measured for different incident angles of the sound beam.

The velocity distribution on the transducer was reconstructed as a solution of the Tikhonov regularized inverse problem. The parametrized form of the velocity was used in computing the source term for the UWVF model.

A relatively good agreement was found between the measurements and the Helmholtz model for both plates at low angles of incidence. However, at larger angles, the accuracy of the simulations deteriorated. An interesting feature is the large discrepancy between simulated and measured fields for Plate 1 at large angles. The transition of the measured transmitted beam toward the negative x-axis for 20 degree angle was much larger than was observed in the simulations (based on the more detailed measurements the simulations fail somewhere between 15-17.5 degrees). Correspondingly, in the case of Plate 2, the simulations become unreliable when the angle of the plate is larger than 20 degrees.

There are several possible candidates for the cause of inaccuracy of the simulations. For example, the Helmholtz model does not take into account the generation of waves other than P-waves. In the plastic plates, however, mode conversion into other types of elastic waves is possible, especially at large incident angles. This is the most probable cause to the failure of the Helmholtz model for the largest incident angle $\theta = 30$ deg. It may be possible to improve the UWVF solver by coupling the Helmholtz model (which can be used to model the field in water) and the Navier model for the plastic.

Another drawback in the simulations of this chapter was that the transducer was modeled as a perfectly rigid surface for back scattered waves. In practice, the performance of the PZT transducer may be altered by standing waves between the plates and the transducer [15]. Particularly, back-scattered waves from the plate hit the transducer and may therefore disturb the generation of the sound from the PZT element. This may lead to the weakening of the output of the transducer and cause the deformation of the generated field. The back-scattered waves are a possible reason for the discrepancies between simulations and measurements at small angles of the plates such as was observed in the case Plate 1 with $\theta = 0$.

Chapter IX

Conclusions

In this thesis, the feasibility of the ultra weak variational formulation (UWVF) for the large-scale modeling of time-harmonic ultrasound problems was studied. The previously proposed UWVF scheme [29] for the Helmholtz problems in inhomogeneous medium was analyzed numerically in 2D and 3D. Furthermore, the perfectly matched layer (PML) method was coupled with the UWVF. This provided an improved means to truncate physically unbounded Helmholtz problems. The UWVF method was also extended to approximate 2D elastic wave problems. Analogously to the previous UWVF studies, the discrete UWVF was obtained using plane wave basis functions. In the case of elastic waves, however, the basis must consists of two wave components that arise from the Helmholtz decomposition of the problem.

It was known from previous studies [29, 30] that when compared with the low order finite element methods, the UWVF method reduces the number of degrees of freedom needed for a tolerable accuracy of the approximation. Moreover, even though the system matrices of the UWVF scheme are less sparse than those of the FEM, the numerical experiments with the UWVF of the Navier equation in Chapter 5 showed that the UWVF also reduces the overall memory storage of the problem.

From the computational point of view, the restriction on the use of plane wave basis functions in the discrete UWVF has been the numerical instability of the approximation. This drawback is not a property of the UWVF method only, but has been observed also with other methods that utilize similar basis functions, see e.g. [5] for the infinite elements or [136] for the finite element method. In this thesis, the conditioning of the UWVF method was improved by allowing the number of plane wave basis functions to vary within the computational mesh. More precisely, the directions for the plane waves were angularly equidistributed. Then, the accuracy of the UWVF approximation can be expected to improve with the increase of the number of basis functions. The increase of the basis functions, however, reduces the conditioning of the resulting matrix equation.

Therefore, it is natural to assume that the best approximation for a fixed mesh and with the angularly equidistributed basis functions is obtained by using the

largest number of basis functions in each element which allows the stable solution of the UWVF problem. The results of Chapter 5 showed that in the UWVF, the overall stability of the problem can be predicted from the conditioning of the elementwise subproblems. This approach was first developed for 2D acoustic and elastic problems and then extended to 3D acoustic problems in Chapter 6. The 3D model also used the perfectly matched layer (PML) to reduce unphysical numerical reflections from the artificial boundary enclosing the computational domain.

As a practical application of the UWVF method, Chapter 7 included a simulation study for analyzing anomalies associated with continuous-wave ultrasound field measurements. Traditionally, pulsed ultrasound has been used in medical applications mainly for imaging purposes. However, developments in medical imaging techniques have given rise to a renewed interest in the therapeutic use of ultrasound using continuous wave fields. This has increased the need for experimental continuous-wave field measurements which are known to be demanding due to distortions caused by standing waves. In particular, the hydrophone is known to alter the measured field.

In addition, the 3D UWVF approximations for the Helmholtz equation were compared with experimental measurements in Chapter 8. The propagation medium consisted of layered plastic plates immersed in water and the field was generated by a circular planar transducer operating at frequency 531 kHz. The agreement of the model with experiment is reasonably good if the sound beam hits the plates with relatively small indicent angles. However, the accuracy deteriorated at larger incident angles. A possible reason is that the Helmholtz model does not take into account mode conversion into elastic waves which is expected to take place especially at larger angles.

Although the results of this thesis have shown that the UWVF method is a promising candidate for the large-scale modeling of acoustic and elastic waves, a lot of further work remains. An obvious improvement in the use of the plane wave basis functions would be the abandonment of equispaced directions. Instead, the directions should be used adaptively as proposed in [133] or based on the a priori information of the solution (this can be obtained, for example, using a ray-method as in [72]).

Another drawback of the UWVF method is its limitation to problems with piecewise constant material properties. Specifically, in the choice of the approximating space for each element, the method utilizes free-space solutions of the problem with the material properties in the given element. A method for constructing plane wave solutions of the Helmholtz problems with linearly varying material properties has been proposed in [19]. However, this idea has not been yet implemented with any numerical scheme.

The future work should also include the coupling of separate acoustic and elastic UWVF methods. In the coupled model, the wave field in parts of the computational domain are modeled with the Helmholtz equation whereas in the other parts the Navier equation can be used. The boundary conditions on the interface of the acoustic and elastic regions can be constructed by using the fluid-solid transmission conditions (2.32). However, to be able to include the coupled

transmission conditions to the UWVF method, they must be reformulated as the impedance boundary conditions. In the fluid-solid extension of the UWVF, this will be a major challenge.

The elastic UWVF model introduced in this thesis was formulated for 2D problems. A natural future improvement will be the extension of the method to 3D elastic wave problems. This requires, however, an additional set of S-wave basis functions, since in 3D the elastic wave consists of the P-wave and two polarizations of S-waves known as horizontal (SH-) and vertical (SV-) waves. In addition, the feasibility of the PML method (used with Helmholtz-UWVF in this thesis) for with the elastic UWVF is worth studying.

The measurements in this thesis were conducted using plastic plates. In order to use the UWVF model for medical ultrasonics, more complicated test problems must be analyzed. These include, for example, ultrasound propagation in ex vivo tissue samples.

Appendix I

Exact solution for the acoustic transmission problem

Let the computational domain consists of two concentric circles centered at the origin, see Fig. 5.1. Moreover, let the interface between subdomains Ω_1 and Ω_2 be denoted by $\Sigma_{1,2}$ and exterior boundary by Γ. The outward normal of Ω_1 on $\Sigma_{1,2}$ is n_1 and outward normal of Ω_2 on Γ is n_2. The radii of the domain Ω_1 and Ω_2 are R_1 and R_2, respectively. In addition, in the polar coordinates (R, θ), the point source is located at $(R_0, 0)$ where $R_0 > R_2$.

The acoustic transmission is formulated as coupled Helmholtz problem. Let p_k, κ_k and ρ_k be acoustic pressure, material density and wave number in the domain Ω_k, $k = 1, 2$. Furthermore, let the field in Ω_2 consist of the scattered and incident parts $p_2 = p_2^{\text{sc}} + p_2^{\text{in}}$. Hence, the problem is

$$\Delta p_k + \kappa_k^2 p_k = 0 \qquad \text{in } \Omega_k, \quad k = 1, 2 \tag{A.1}$$

$$p_1(R_1, \theta) = p_2(R_1, \theta) \qquad \text{on } \Sigma_{1,2} \tag{A.2}$$

$$\frac{1}{\rho_1}\frac{\partial p_1}{\partial n_1}(R_1, \theta) = \frac{1}{\rho_2}\frac{\partial p_2}{\partial n_1}(R_1, \theta) \qquad \text{on } \Sigma_{1,2}, \tag{A.3}$$

$$\frac{\partial p_2^{\text{sc}}}{\partial n_2}(R_2, \theta) - i\kappa_2 p_2^{\text{sc}}(R_2, \theta) = 0 \qquad \text{on } \Gamma. \tag{A.4}$$

A Fourier expansion to the point source can be written in the polar coordinates as [153]

$$\begin{aligned} p_2^{\text{in}}(R, \theta) &= \frac{i}{4} H_0^{(1)}(\kappa_2 |r - r_0|) \\ &= \sum_{n=-\infty}^{\infty} (-1)^n \frac{i}{4} H_n^{(1)}(\kappa_2 R_0) J_n(\kappa_2 R) e^{in\theta} \end{aligned} \tag{A.5}$$

where $H_n^{(1)}$ is the Hankel function of the first kind and nth order. The Bessel function of the nth order is denoted by J_n. A Fourier expansion for the pressure

field in the domain Ω_1 is written in the form

$$p_1(R,\theta) = \sum_{n=-\infty}^{\infty} a_n J_n(\kappa_1 R) e^{in\theta}, \tag{A.6}$$

where a_n a complex valued coefficient which will be determined by the boundary conditions (A.2) and (A.3).

In the domain Ω_2 the scattered pressure field p_2^{sc} is written in the form of the Fourier series by using two terms

$$p_2^{\text{sc}}(R,\theta) = \sum_{n=-\infty}^{\infty} \left[b_n H_n^{(1)}(\kappa_2 R) + c_n H_n^{(2)}(\kappa_2 R) \right] e^{in\theta}, \tag{A.7}$$

where coefficient b_n and c_n are to be determined. The first term $b_n H_n^{(1)}$ satisfies the Sommerfeld radiation condition and hence corresponds to the radiating part of the solution. The second term $c_n H_n^{(2)}$ gives spurious reflections arising from the approximate absorbing boundary condition (A.4).

By substituting the Fourier expansions (A.5), (A.6) and (A.7) to the boundary conditions (A.2)-(A.4), one obtains three equations from which the unknown Fourier coefficients a_n, b_n and c_n are resolved.

Bibliography

[1] J.D. Achenbach. *Wave Propagation in Elastic Solids*. North-Holland, 1973.

[2] M. Ainsworth. Dispersive properties of high order finite elements. In G.C. Cohen, E. Heikkola, P. Joly, and P. Neittaanmäki, editors, *Mathematical and Numerical Aspects of Wave Propagation - Waves 2003*, pages 3–9. Springer, 2003.

[3] R.J. Astley. Wave envelope and infinite elements for acoustical radiation. *International Journal for Numerical Methods in Fluids*, 3:507–526, 1983.

[4] R.J. Astley. Infinite elements for wave problems: a review of current formulations and an assessment of accuracy. *International Journal for Numerical Methods in Engineering*, 49(7):951–976, 2000.

[5] R.J. Astley and J.-P. Coyette. Conditioning of infinite element schemes for wave problems. *Communications in Numerical Methods in Engineering*, 17(1):31–41, 2001.

[6] R.J. Astley and W. Eversman. Finite element formulations for acoustical radiation. *Journal of Sound and Vibration*, 88(1):47–64, 1983.

[7] J.-F. Aubry, M. Tanter, M. Pernot, J.-L. Thomas, and M. Fink. Experimental demonstration of noninvasive transskull adaptive focusing based on prior computed tomography scans. *The Journal of the Acoustical Society of America*, 113(1):84–93, 2003.

[8] B.A. Auld. *Acoustic Fields and Waves in Solids vols. I-II*. John Wiley and Sons, 1973.

[9] K.A. Aziz. and R.B. Kellogg. Finite element analysis of a scattering problem. *Mathematics of Computation*, 37(156):261–271, 1981.

[10] I. Babuška and J.M. Melenk. The partition of unity method. *International Journal for Numerical Methods in Engineering*, 40:727–758, 1997.

[11] I. Babuška and S. Sauter. Is the pollution effect on the FEM avoidable for the Helmholtz equation considering high wave numbers? *SIAM Journal of Numerical Analysis*, 34(6):2392–2432, 1997.

[12] J.W. Barnard, W.J. Fry, F.J. Fry, and J.F. Brennan. Small localized ultrasonic lesions in the white and gray matter of the cat brain. *Archives of Neurology and Psychiatry*, 75:15–35, 1956.

[13] G.K. Batchelor. *An Introduction to Fluid Dynamics*. Cambridge University Press, 1967.

[14] A. Bayliss, M. Gunzburger, and E. Turkel. Boundary conditions for the numerical solution of elliptic equations in exterior regions. *SIAM Journal of Applied Mathematics*, 42(2):430–451, 1982.

[15] K. Beissner. The influence of membrane reflections on ultrasonic power measurements. *Acustica*, 50:194–200, 1982.

[16] J.D. Benamou and B. Després. A domain decomposition method for the Helmholtz equation and related optimal control problems. *Journal of Computational Physics*, 136:68–82, 1997.

[17] J. Bérenger. A perfectly matched layer for the absorption of electromagnetic waves. *Journal of Computational Physics*, 114:185–200, 1994.

[18] P. Bettess. *Infinite Elements*. Penshaw Press, 1992.

[19] P. Bettess. Special wave basis finite elements for very short wave refraction and scattering problems. Preprint, 2003.

[20] P. Bettess, J. Shirron, O. Laghrouche, B. Peseux, R. Sugimoto, and J. Trevelyan. A numerical integration scheme for special finite elements for the Helmholtz equation. *International Journal for Numerical Methods in Enineering*, 56:531–552, 2003.

[21] P. Bettess and O.C. Zienkiewicz. Diffraction and refraction of surface waves using finite and infinite elements. *International Journal for Numerical Methods in Engineering*, 11:1271–1290, 1977.

[22] A.B. Bhatia. *Ultrasonic Absorption*. Dover Publications, 1967.

[23] P.E. Bloomfield, W.-J. Lo, and P.A. Lewin. Experimental study of the acoustic properties of polymers utilized to construct PVDF ultrasonic transducers and the acousto-electric properties of PVDF and P(VDF/TrFE) films. *IEEE Transactions on Ultrasonics, Ferroelectrics, and Frequency Control*, 47(6):1397–1405, 2000.

[24] Y.Y. Botros, E.S. Ebbini, and J.L. Volakis. Two-step hybrid virtual array-ray (VAR) technique for focusing through the rib cage. *IEEE Transactions on Ultrasonics, Ferroelectrics, and Frequency Control*, 45(4):989–1000, 1998.

[25] Y.Y. Botros, J.L. Volakis, P. VanBaren, and E.S. Ebbini. A hybrid computational model for ultrasound phased-array heating in the presence of strongly scattering obstacles. *IEEE Transactions on Biomedical Engineering*, 44(11):1039–1050, 1997.

[26] S.C. Brenner and L.R. Scott. *The Mathematical Theory of Finite Element Methods*. Springer, 1994.

[27] M.O. Bristeau, R. Glowinski, and J. Périaux. Controllability methods for the computation of time-periodic solutions; application to scattering. *Journal of Computational Physics*, 147(2):239–646, 1998.

[28] D.S. Burnett. A three-dimensional acoustic infinite element based on a prolate spheroidal multipole expansion. *The Journal of the Acoustical Society of America*, 96(5):2798–2816, 1994.

[29] O. Cessenat. *Application d'une nouvelle formulation variationelle des equations d'ondes harmonigues, Problemes de Helmholtz 2D et de Maxwell 3D*. PhD thesis, Paris IX Dauphine, 1996.

[30] O. Cessenat and B. Després. Application of an ultra weak variational formulation of elliptic PDEs to the two-dimensional Helmholtz problem. *SIAM Journal of Numerical Analysis*, 35(1):255–299, 1998.

[31] O. Cessenat and B. Després. Using plane waves as base functions for solving time harmonic equations with the ultra weak variational formulation. *Journal of Computational Acoustics*, 11(2):227–238, 2003.

[32] S.N. Chandler-Wilde, S. Langdon, and L. Ritte. A high wavenumber boundary element method for an acoustic scattering problem. Technical Report TR/02/03, Brunel University, Department of Mathematical Sciences, March 2003.

[33] Y.C. Chang and L. Demkowicz. Solution of viscoelastic scattering problems in linear acoustics using *hp* boundary/finite element method. *International Journal for Numerical Methods in Engineering*, 44:1888–1907, 1999.

[34] W.C. Chew and W.H. Weedon. A 3D perfectly matched medium from modified Maxwell's equations with stretched coordinates. *Microwave and Optical Technology Letters*, 7(13):599–604, 1994.

[35] G.T. Clement and K. Hynynen. Field characterization of therapeutic ultrasound phased arrays through forward and backward planar projection. *The Journal of the Acoustical Society of America*, 108(1):441–446, 2000.

[36] G.T. Clement and K. Hynynen. The role of internal reflection in transkull phase distortion. *Ultrasonics*, 39:109–113, 2001.

[37] G.T. Clement and K. Hynynen. Correlation of the ultrasound phase with physical skull properies. *Ultrasound in Medicine and Biology*, 28(5):617–624, 2002.

[38] G.T. Clement and K. Hynynen. A non-invasive method for focusing ultrasound through the human skull. *Physics in Medicine and Biology*, 47(8):1219–1236, 2002.

[39] G.T. Clement, J. Sun, T. Giesecke, and K. Hynynen. A hemisphere array for non-invasive ultrasound brain therapy and surgery. *Physics in Medicine and Biology*, 45:3707–3719, 2000.

[40] G.T. Clement, J. White, and K. Hynynen. Investigation of a large-area phased array for focused ultrasound surgery through the skull. *Physics in Medicine and Biology*, 45:1071–1083, 2000.

[41] H.E. Cline, K. Hynynen, C.J. Hardy, R.D. Watkins, J.F. Schenck, and F.J. Jolesz. MR temperature mapping of focused ultrasound surgery. *Magnetic Resonance in Medicine*, 31:628–636, 1994.

[42] G.C. Cohen. *Higher-Order Numerical Methods for Transient Wave Equations*. Springer-Verlag, 2002.

[43] R. Coifman, V. Rokhlin, and S. Wandzura. The fast multiple method for the wave equation: a pedestrian prescription. *IEEE Antennas and Propagation Magazine*, 35(3):7–12, 1993.

[44] F. Collino, S. Ghanemi, and P. Joly. Domain decomposition method for harmonic wave propagation: a general presentation. *Computer Methods in Applied Mechanics and Engineering*, 184:171–211, 2000.

[45] F. Collino and P. Monk. Optimizing the perfectly matched layer. *Computer Methods in Applied Mechanics and Engineering*, 164:157–171, 1998.

[46] F. Collino and P. Monk. The perfectly matched layers in curvilinear coordinates. *SIAM Journal of Scientific Computing*, 19(6):2061–2090, 1998.

[47] D. Colton and R. Kress. *Integral Equation Methods in Scattering Theory*. Springer-Verlag, 1983.

[48] D. Colton and R. Kress. *Inverse Acoustic and Electromagnetic Scattering Theory*. Springer-Verlag, 1992.

[49] D. Colton and P. Monk. Mathematical and numerical methods in inverse acoustic scattering theory. *Zeitschrift für Angewandte Mathematik und Physic*, 81:723–731, 2001.

[50] C.W. Connor, G.T. Clement, and K. Hynynen. A unified model for the speed of sound in cranial bone based on genetic algorithm optimization. *Physics in Medicine and Biology*, 47(22):3925–3944, 2002.

[51] C.W. Connor and K. Hynynen. Bio-acoustic thermal lensing and nonlinear propagation in focused ultrasound surgery using large focal spots: a parametric study. *Physics in Medicine and Biology*, 47:1911–1928, 2002.

[52] E. Darve. The fast multipole method: numerical implementation. *Journal of Computational Physics*, 160:195–240, 2000.

[53] A. de La Bourdonnaye. Convergence of the approximation of wave functions by oscillatory functions in the high frequency limit. *Comptes Rendus de l'Academie des Science. Serie I*, 318:765–768, 1994.

[54] A. de La Bourdonnaye. High frequency approximations of integral equations modeling of scattering phenomena. *Mathematical Modelling and Numerical Analysis*, 28:223–241, 1994.

[55] L. Demkowicz and J.T. Oden. Application of *hp*-adaptive BE/FE methods to elastic scattering. *Computer Methods in Applied Mechanics and Engineering*, 133:287–317, 1996.

[56] B. Després. Sur une formulation variationnelle de type ultra-faible. *Comptes Rendus de l'Academie des Sciences - Series I*, 318:939–944, 1994.

[57] F.A. Duck, H.C. Starritt, and S.P. Anderson. A survey of the acoustic output of ultrasonic Doppler equipment. *Clinical Physics and Physiological Measurement*, 8(1):39–49, 1987.

[58] E.S. Ebbini and C.A. Cain. Multiple-focus ultrasound phased-array pattern synthesis: optimal driving-signal distributions for hyperthermia. *IEEE Transactions on Ultrasonics, Ferroelectrics, and Frequency Control*, 36(5):540–548, 1989.

[59] E.S. Ebbini and C.A. Cain. A spherical-section ultrasound phased array applicator for deep localized hyperthermia. *IEEE Transactions on Biomedical Engineering*, 38(7):634–643, 1991.

[60] B. Engquist and A. Majda. Absorbing boundary conditions for the numerical simulation of waves. *Mathematics of Computation*, 31(139):629–651, 1977.

[61] X. Fan and K. Hynynen. The effect of wave reflection and refraction at soft tissue interfaces during ultrasound hyperthermia treatments. *The Journal of the Acoustical Society of America*, 91(3):1727–1736, 1992.

[62] X. Fan, E.G. Moros, and W.L. Straube. Acoustic field prediction for a single planar continuous-wave source using an equivalent phased array method. *The Journal of the Acoustical Society of America*, 102(5):2734–2741, 1997.

[63] C. Farhat, I. Harari, and L. Franca. The discontinuous enrichment method. *Computer Methods in Applied Mechanics and Engineering*, 190:6455–6479, 2001.

[64] C. Farhat, I. Harari, and U. Hetmaniuk. A discontinuous Galerkin method with Lagrange multipliers for the solution of Helmholtz problems in the mid-frequency regime. *Computer Methods in Applied Mechanics and Engineering*, 192:1389–1419, 2003.

[65] P. Filippi, D. Habault, J.P. Lefebvre, and A. Bergassoli. *Acoustics*. Academic Press, 1999.

[66] J.F. Fry and J.E. Barger. Acoustical properties of human skull. *The Journal of the Acoustical Society of America*, 63(5):1576–1590, 1978.

[67] W.J. Fry, J.W. Barnard, F.J Fry, R.F. Krumins, and J.F. Brennan. Ultrasonic lesions in the mammalian central nervous system. *Science*, 122:517–518, 1955.

[68] M. Gautherie, editor. *Methods for External Hyperthermic Heating*. Springer-Verlag, 1990.

[69] P. Gélat, R. Preston, and A. Hurrell. Development, validation and publication of a complete theoretical model for hydrophone/amplifier transfer characteristics. Technical Report CMAM 61, National Physical Laboratory, 2001.

[70] K. Gerdes. A summary of infinite element formulations for exterior Helmholtz problems. *Computer Methods in Applied Mechanics and Engineering*, 164:95–105, 1998.

[71] K. Gerdes and F. Ihlenburg. On the pollution effect in FE solutions of the 3D-Helmholtz equation. *Computer Methods in Applied Mechanics and Engineering*, 170:155–172, 1999.

[72] E. Giladi and J. B. Keller. A hybrid numerical asymptotic method for scattering problems. *Journal of Computational Physics*, 174(1):226–247, 2001.

[73] D. Givoli. Non-reflecting boundary conditions. *Journal of Computational Physics*, 94:1–29, 1991.

[74] D. Givoli. High-order nonreflecting boundary conditions without high-order derivatives. *Journal of Computational Physics*, 170(2):849–870, 2001.

[75] D. Givoli and J.B. Keller. Non-reflecting boundary conditions for elastic waves. *Wave motion*, 12:261–279, 1990.

[76] A. Goldstein, D.R. Gandhi, and W.D. O'Brien Jr. Diffraction effects in hydrophone measurements. *IEEE Transactions on Ultrasonics, Ferroelectrics, and Frequency Control*, 45(4):972–979, 1998.

[77] C.I. Goldstein. Numerical methods for Helmholtz type equations in unbounded region. In J.A. DeSanto, A.W. Saenz, and W.W. Zachary, editors, *Mathematical Methods and Applications of Scattering Theory*, volume 130 of *Lecture Notes in Physics*, pages 26–33. Springer, 1980.

[78] C.I. Goldstein. The finite-element method with non-uniform mesh sizes applied to the exterior Helmholtz problem. *Numerische Mathematik*, 38:61–82, 1981.

[79] K.F. Graff. *Wave Motion in Elastic Solids*. Dover Publications, 1991.

[80] M. Greenspan. Piston radiator: some extensions of the theory. *The Journal of the Acoustical Society of America*, 65(3):608–621, 1979.

[81] M.J. Grote and J.B. Keller. On nonreflecting boundary conditions. *Journal of Computational Physics*, 122:231–243, 1995.

[82] M.J. Grote and J.B Keller. Exact nonreflecting boundary condition for elastic waves. *SIAM Journal on Applied Mathematics*, 60(3):803–819, 2000.

[83] I. M. Hallaj, R. O. Cleveland, and K. Hynynen. Simulations of the thermoacoustic lens effect during focused ultrasound surgery. *The Journal of the Acoustical Society of America*, 109(5):2245–2253, 2001.

[84] L. Halpern. *Etude de conditions aux limites absorbantes pour des schemas numeriques relatifs a des equations hyperboliques lineaires*. PhD thesis, Universite Paris VI, Place Jussieu, Paris, 1980.

[85] M.F. Hamilton and D.T. Blackstock. *Nonlinear Acoustics*. Academic Press, 1998.

[86] P.C. Hansen. *Rank-Deficient and Discrete Ill-Posed Problems: Numerical Aspects of Linear Inversion*. SIAM, 1998.

[87] I. Harari and S. Haham. Improved finite element methods for elastic waves. *Computer Methods in Applied Mechanics and Engineering*, 166:143–164, 1998.

[88] I. Harari and T.J.R. Hughes. Analysis of continuous formulations underlying the computation of time-harmonic acoustics in exterior domains. *Computer Methods in Applied Mechanics and Engineering*, 97(1):103–124, 1992.

[89] I. Harari and T.J.R. Hughes. A cost comparison of boundary element and finite element methods for problems of time-harmonic acoustics. *Computer Methods in Applied Mechanics and Engineering*, 97:77–102, 1992.

[90] I. Harari and T.J.R. Hughes. Galerkin/least-squares finite element methods for the reduced wave equation with non-reflecting boundary conditions in unbounded domains. *Computer Methods in Applied Mechanics and Engineering*, 98:411–454, 1992.

[91] I. Harari, M. Slavutin, and E. Turkel. Analytical and numerical studies of a finite element PML for the Helmholtz equation. *Journal of Computational Acoustics*, 8(1):121–137, 2000.

[92] I. Harari and E Turkel. Accurate finite difference methods for time-harmonic wave propagation. *Journal of Computational Physics*, 119:252–270, 1995.

[93] R.H. Hardin, N.J.A. Sloane, and W. D. Smith. Spherical coverings, May 1997. Available on: http://www.research.att.com/ njas/coverings/index.html.

[94] G.R. Harris. Hydrophone measurements in diagnostic ultrasound fields. *IEEE Transactions on Ultrasonics, Ferroelectrics, and Frequency Control*, 35(2):87–101, 1988.

[95] G.R. Harris, R.C. Preston, and A.S. DeReggi. The impact of piezoelectric PVDF on medical ultrasound exposure measurements, standards, and requlations. *IEEE Transactions on Ultrasonics, Ferroelectrics, and Frequency Control*, 47(6):1321–1335, 2000.

[96] M. Hayner and K. Hynynen. Numerical analysis of ultrasonic transmission and absorption of oblique plane waves trough the human skull. *The Journal of the Acoustical Society of America*, 110:3320–3330, 2001.

[97] E. Heikkola, T. Rossi, and J. Toivanen. A parallel fictitious domain method for the three-dimensional Helmholtz equation. *SIAM Journal on Scientific Computing*, 24(5):1567–1588, 2003.

[98] R.L. Higdon. Absorbing boundary conditions for difference approximations to the multi-dimensional wave equation. *Mathematics of Computation*, 47(176):437–459, 1986.

[99] R.L. Higdon. Radiation boundary conditions for elastic wave propagation. *SIAM Journal on Numerical Analysis*, 27:831–869, 1990.

[100] G.C. Hsiao. The coupling of boundary element and finite element methods. *Zeitschrift für Angewandte Mathematik und Mechanik*, 70(6):T493–T503, 1990.

[101] G.C. Hsiao, R.E. Kleinman, and F.R. Roach. Weak solutions of fluid-solid interaction problems. *Mathematische Nachrichten*, 218:139–163, 2000.

[102] B.-N. Hung and A. Goldstein. Acoustic parameters of commercial plastics. *IEEE Transactions on Sonics and Ultrasonics*, SU-30(4):249–254, 1983.

[103] A. Hurrell and F. Duck. A two-dimensional hydrophone array using piezoelectric PVDF. *IEEE Transactions on Ultrasonics, Ferroelectrics, and Frequency Control*, 47(6):1345–1353, 2000.

[104] D.A. Hutchins, H.D. Mair, P.A. Puhach, and A.J. Osei. Continuous-wave pressure fields of ultrasonic transducer. *The Journal of the Acoustical Society of America*, 80(1):1–12, 1986.

[105] T. Huttunen, J.P. Kaipio, and K. Hynynen. Modeling of anomalies due to hydrophones in continuous-wave ultrasound fields. *IEEE Transactions on Ultrasonics, Ferroelectrics, and Frequency Control*, 50(11):1486–1500, 2003.

[106] T. Huttunen, J.P. Kaipio, and P. Monk. The perfectly matched layer for the ultra weak variational formulation of the 3D Helmholtz problem. *International Journal for Numerical Methods in Engineering*, 2003. Submitted.

[107] T. Huttunen, P. Monk, F. Collino, and J.P. Kaipio. The ultra weak variational formulation for elastic wave problems. *SIAM Journal on Scientific Computing*, 2003. Accepted.

[108] T. Huttunen, P. Monk, and J.P. Kaipio. Computational aspects of the ultra-weak variational formulation. *Journal of Computational Physics*, 182:27–46, 2002.

[109] K. Hynynen. The role of nonlinear ultrasound propagation during hyperthermia treatments. *Medical Physics*, 18(6):1156–1163, 1991.

[110] K. Hynynen. Review of ultrasound therapy. *IEEE Ultrasonics Symposium*, pages 1305–1313, 1997.

[111] K. Hynynen and F.A. Jolesz. Demonstration of potential noninvasive ultrasound brain therapy through an intact skull. *Ultrasound in Medicine and Biology*, 24(2):275–283, 1998.

[112] F. Ihlenburg. *Finite Element Analysis of Acoustic Scattering*. Springer, 1998.

[113] F. Ihlenburg and I. Babuška. Dispersion analysis and error estimation of Galerkin finite element methods for the Helmholtz equation. *International Journal for Numerical Methods in Engineering*, 38:3745–3774, 1995.

[114] F. Ihlenburg and I. Babuška. Finite element solution of the Helmholtz equation with high wave number part I: the h-version of the FEM. *Computers Mathematics with Applications*, 30(9):9–37, 1995.

[115] F. Ihlenburg and I. Babuška. Finite element solution of the Helmholtz equation with high wave number part II: the h-p version of the FEM. *SIAM Journal of Numerical Analysis*, 34(1):315–358, 1997.

[116] Feng Kang. Finite element method and natural boundary reduction. In *Proceedings of the International Congress of Mathematicians*, pages 1439–1453, Warsaw, 1983.

[117] A. Karp. A convergent far field expansion for the two-dimensional radiation functions. *Communications on Pure and Applied Mathematics*, 14:427–434, 1961.

[118] G. Karypis. METIS - family of multilevel partitioning algorithms, June 2003. Available on: http://www-users.cs.umn.edu/ karypis/metis/.

[119] G. Karypis and V. Kumar. A fast and high quality multilevel scheme for partitioning irregular graphs. *SIAM Journal on Scientific Computing*, 20(1):359–392, 1998.

[120] J.B. Keller. Progress and prospects in the theory of linear wave propagation. *SIAM Review*, 21(2):229–245, 1979.

[121] J.B. Keller. Exact non-reflecting boundary conditions. *Journal of Computational Physics*, 82:172–193, 1989.

[122] K.R. Kelly, R.W. Ward, S. Treitel, and R.M. Alford. Synthetic seismograms: A finite-difference approach. *Geophysics*, 41:2–27, 1976.

[123] D.E. Keyes, Y. Saad, and D.G. Truhlar, editors. *Domain-Based Parallelism and Problem Decomposition in Computational Science and Engineering*. SIAM, 1995.

[124] S. Kim. Domain decomposition iterative procedures for solving scalar waves in the frequency domain. *Numerische Mathematik*, 79:231–259, 1998.

[125] A. Kirsch and P. Monk. Convergence analysis of a coupled finite element spectral method in acoustic scattering. *IMA Journal of Numerical Analysis*, 9:425–447, 1990.

[126] D. Komatitsch, J. Ritsema, and J. Tromp. The spectral-element method, Beowulf computing, and global seismology. *Science*, 298:1737–1742, 2002.

[127] D. Komatitsch and J. Tromp. Spectral-element simulations of global seismic wave propagation I. Validation. *Geophysical Journal International*, 149:390–412, 2002.

[128] D. Komatitsch, S. Tsuboi, J. Chen, and J. Tromp. A 14.6 billion degrees of freedom, 5 teraflops, 2.5 terabyte earthquake simulation on the Earth Simulator. In *Proceedings of the ACM / IEEE Supercomputing SC'2003 conference*, 2003. In Press.

[129] R. Kress. *Linear Integral Equations*. Springer-Verlag, 1989.

[130] E. Kühnicke. Three-dimensional waves in layered media with nonparallel and curved interfaces: A theoretical approach. *The Journal of the Acoustical Society of America*, 100(2):709–716, 1996.

[131] V.D. Kupradze. *Potential Methods in the Theory of Elasticity*. Israel Program for Scientific Translations, 1965.

[132] P.K. Kythe. *An Introdunction to Boundary Element Methods*. CRC Press, 1995.

[133] O. Laghrouche and P. Bettess. *Short wave modelling using special finite elements - Towards an adaptive approach*, chapter 10, pages 181–194. Mathematics of Finite Elements and Applications (MAFELAP 1999). Elsevier, 1999.

[134] O. Laghrouche and P. Bettess. Short wave modelling using special finite elements. *Journal of Computational Acoustics*, 8(1):189–210, 2000.

[135] O. Laghrouche, P. Bettess, and R.J. Astley. Modelling of short wave diffraction problems using approximating systems of plane waves. *International Journal for Numerical Methods in Engineering*, 54:1501–1533, 2002.

[136] O. Laghrouche, P. Bettess, and R. Sugimoto. Analysis of the conditioning number of the plane wave approximation for the Helmholtz equation. In *European Congress on Computational Methods in Applied Sciences and Engineering*, Barcelona, Spain, 11-14 September 2000. ECCOMAS.

[137] L.D. Landau and E.M. Lifshitz. *Theory of Elasticity*. Butterworth Heinemann, third edition, 1986.

[138] M. Lassas and E. Somersalo. Analysis of the PML equations in general convex geometry. *Proceedings of the Royal Society of Edinburgh. Section A. Mathematics.*, 131(5):1183–1207, 2001.

[139] P.P. Lele. A simple method for production of trackless focal lesions with focused ultrasound: physical factors. *Journal of Physiology*, 160:492–512, 1962.

[140] P.A. Lewin. Miniature pezoelectric polymer ultrasonic hydrophone probes. *Ultrasonics*, 19(5):213–216, 1981.

[141] G. Luo, J. J. Kaufman, A. Chiabrera, B. Bianco, J.H. Kinney, D. Haupth, J. T. Ryaby, and R.S. Siffert. Computational methods for ultrasonic bone assessment. *Ultrasound in Medicine and Biology*, 25(5):823–830, 1999.

[142] J.G. Lynn, R.L. Zwemer, A.J. Chick, and A.E. Miller. A new method for the generation and use of focused ultrasound in experimental biology. *Journal of General Physiology*, 26:179–193, 1942.

[143] M. Malinen, S.R. Duncan, T. Huttunen, and J.P. Kaipio. Feedforward and feedback control methods for ultrasound surgery. 2003. Submitted.

[144] M. Malinen, T. Huttunen, and J.P. Kaipio. Optimal control for the ultrasound induced heating of a tumor. In *4th International Conference on Inverse Problems in Engineering: Theory and Practice*, pages 429–436, Angra dos Reis, Brazil, May 26-31 2002.

[145] M. Malinen, T. Huttunen, and J.P. Kaipio. An optimal control approach for ultrasound induced heating. *International Journal of Control*, 76:1323–1336, 2003.

[146] M. Malinen, T. Huttunen, and J.P. Kaipio. Thermal dose optimization method for ultrasound surgery. *Physics in Medicine and Biology*, 48:745–762, 2003.

[147] G.D. Manolis, R.P. Shaw, and S. Pavlou. Elastic waves in nonhomogeneous media under 2D conditions: I. fundamental solutions. *Soil Dynamics and Earthquake Engineering*, 18(1):19–30, 1999.

[148] T.D. Mast, L.M. Hinkelman, L.A. Metlay, M.J. Orr, and R.C. Waag. Simulation of ultrasonic pulse propagation, distortion, and attenuation in the human chest wall. *The Journal of the Acoustical Society of America*, 106(6):3665–3677, 1999.

[149] T.D. Mast, L.P. Souriau, D.L.D. Liu, M. Tabei, A.I. Nachman, and R.C. Waag. A k-space method for large-scale models of wave propagation in tissue. *IEEE Transactions on Ultrasonics, Ferroelectrics, and Frequency Control*, 48(2):341–354, 2001.

[150] P. Mayer and J. Mandel. The finite ray element method for the Helmholtz equation of scattering: first numerical experiments. Technical Report 111, University of Colorado at Denver, Center for Computational Mathematics, 1997.

[151] O.Z. Mehdizadeh and M. Paraschivoiu. Investigation of a two-dimensional spectral element method for Helmholtz's equation. *Journal of Computational Physics*, 189:111–129, 2003.

[152] P. Monk and D. Wang. A least squares method for the Helmholtz equation. *Computer Methods in Applied Mechanics and Engineering*, 175:121–136, 1999.

[153] P.M. Morse and K.U. Ingard. *Theoretical Acoustics*. McGraw-Hill Book Company, 1968.

[154] Y. Nakamura and T. Otani. Study of surface elastic wave induced on backing material and diffracted field of a piezoelectric polymer film hydrophone. *The Journal of the Acoustical Society of America*, 94(3):1191–1199, 1993.

[155] A.A. Oberai and P.M. Pinsky. A numerical comparison of finite element methods for the Helmholtz equation. *Journal of the Computational Acoustics*, 8(1):211–221, 2000.

[156] A.A. Oberai and P.M. Pinsky. A residual-based finite element method for the Helmholtz equation. *International Journal for Numerical Methods in Engineering*, 49(3):399–419, 2000.

[157] P. Ortiz and E. Sanchez. An improved partition of the unity finite element model for diffraction problems. *International Journal for Numerical Methods in Engineering*, 50:2727–2740, 2001.

[158] Y.-H. Pao and C.-C. Mow. *Diffraction of Elastic Waves and Dynamic Stress Concentrations*. Crane-Russak Inc., New York, 1973.

[159] M. Pernot, J.-F. Aubry, M. Tanter, J.-L. Thomas, and M. Fink. Experimental validation of 3D finite differences simulations of ultrasonic wave propagation through the skull. *Proceeding of IEEE Ultrasonics Symposium*, pages 1547–1550, 2001.

[160] M. Pernot, J.-F. Aubry, M. Tanter, J.-L. Thomas, and M. Fink. High power transcranial beam steering for ultrasonic brain therapy. *Physics in Medicine and Biology*, 48:2577–2589, 2003.

[161] E. Perrey-Debain, J. Trevelyan, and P. Bettess. P-wave and S-wave decomposition in boundary integral equation for plane elastodynamics. preprint, 2002.

[162] E. Perrey-Debain, J. Trevelyan, and P. Bettess. Plane wave basis in integral equation for 3D scattering. In G.C. Cohen, E. Heikkola, P. Joly, and P. Neittaanmäki, editors, *Mathematical and Numerical Aspects of Wave Propagation - Waves 2003*, pages 292–297. Springer, 2003.

[163] E. Perrey-Debain, J. Trevelyan, and P. Bettess. Wave boundary elements: a theoretical overview presenting applications in scattering of short waves. *Engineering Analysis with Boundary Elements*, 2003. In Press.

[164] N. Phan-Thien. *Understanding Viscoelasticity*. Springer-Verlag, 2002.

[165] A. Piacentini. and N. Rosa. An improved domain decomposition method for the 3D Helmholtz equation. *Computer Methods in Applied Mechanics and Engineering*, 162:113–124, 1998.

[166] A.D. Pierce. *Acoustics: An Introdunction to Its Physical Principles and Applications*. The Acoustical Society of America, 1981.

[167] R. C. Preston, D.R. Bacon, A.J. Livett, and K. Rajendran. PVDF membrane hydrophone performance properties and their relevance to the measurement of the acoustic output of medical ultrasound equipment. *Journal of Physics E: Scientific Instrumentation*, 16:786–796, 1983.

[168] E. Priolo, J.M. Carcione, and G. Seriani. Numerical simulation of interface waves by high-order spectral modeling techniques. *The Journal of the Acoustical Society of America*, 95(2), 1994.

[169] Q. Qi and T.L. Geers. Evaluation of the perfectly matched layer for computational acoustics. *Journal of Computational Physics*, 139:166–183, 1998.

[170] A. Quarteroni. Domain decomposition methods for wave propagation problems. In D.E. Keyes, Y. Saad, and D.G. Truhlar, editors, *Domain-Based Parallelism and Problem Decomposition Methods in Computational Science and Engineering*, chapter 2, pages 21–28. SIAM, 1995.

[171] A. Quarteroni, R. Sacco, and F. Salieri. *Numerical Mathematics*. Springer, 2000.

[172] A. Quarteroni, A. Tagliani, and E. Zampieri. Generalized Galerkin approximations for elastic waves with absorbing boundary conditions. *Computer Methods in Applied Mechanics and Engineering*, 163:323–341, 1998.

[173] S. Robinson, R. Preston, M. Smith, and C. Millar. PVDF reference hydrophone development in the UK - from fabrication and lamination to use as secondary standards. *IEEE Transactions on Ultrasonics, Ferroelectrics, and Frequency Control*, 47(6):1336–1343, 2000.

[174] V. Rokhlin. Rapid solution of integral equations of scattering theory in two dimensions. *Journal of Computational Physics*, 86(2):414–439, 1990.

[175] M.E. Schafer and P.A. Lewin. Transducer characterization using the angular spectrum method. *The Journal of the Acoustical Society of America*, 85(5):2202–2214, 1989.

[176] R.S. Schechter, H.H. Chaskelis, R.B Mignogna, and P.P. Delsanto. Real-time parallel computation and visualization of ultrasonic pulses in solids. *Science*, 265:1188–1192, 1994.

[177] R.S. Schechter, K.E. Simmonds, N.K. Batra, R.B. Mignogna, and R.R. Delsanto. Use of a transient wave propagation code for 3D simulation of cw radiated trasducer fields. *Ultrasonics*, 37:89–96, 1999.

[178] A. Schuhmacher, J. Hald, K.B. Rasmussen, and P.C. Hansen. Sound source reconstruction using inverse boundary element calculations. *The Journal of the Acoustical Society of America*, 113(1):114–127, 2003.

[179] A. Selfridge and P. Goetz. Ellipsoidal hydrophone with improved characteristics. In *IEEE Ultrasonics symposium*, pages 1181–1184, 1999.

[180] J.J. Shirron and I. Babuška. A comparison of approximate boundary conditions and infinite element methods for exterior Helmholtz problems. *Computer Methods in Applied Mechanics and Engineering*, 164:121–139, 1998.

[181] I. Singer and E. Turkel. High-order finite difference methods for the Helmholtz equation. *Computer Methods in Applied Mechanics and Engineering*, 163:343–358, 1998.

[182] G.L.G. Sleijpen and D.R. Fokkema. BiCGstab(ℓ) for linear equations involving unsymmetric matrices with complex spectrum. *Electronic Transactions on Numerical Analysis*, 1:33–48, 1993.

[183] P.R. Stepanishen and K.C. Benjanim. Forward and backward projection of acoustic fields using FFT methods. *The Journal of the Acoustical Society of America*, 71(4):803–812, 1982.

[184] M. Stojek. Least-squares Trefftz-type elements for the Helmholtz equation. *International Journal for Numerical Methods in Engineering*, 41(5):831–849, 1998.

[185] J. Sun and K. Hynynen. Focusing of therapeutic ultrasound through a human skull: A numerical study. *The Journal of the Acoustical Society of America*, 104(3):1705–1715, 1998.

[186] J. Sun and K. Hynynen. The potential of transkull ultrasound therapy and surgery using maximum available skull surface area. *The Journal of the Acoustical Society of America*, 105(4):2519–2527, 1999.

[187] G. ter Haar. Ultrasound focal beam surgery. *Ultrasound in Medicine and Biology*, 21(9):1089–1100, 1995.

[188] G. ter Haar. Therapeutic ultrasound. *European Journal of Ultrasound*, 9:3–9, 1999.

[189] L.L. Thompson and P.M. Pinsky. A Galerkin least-squares finite element method for two-dimensional Helmholtz equation. *International Journal for Numerical Methods in Engineering*, 38:371–397, 1995.

[190] A.N. Tikhonov. Regularization of incorrectly posed problems. *Soviet Mathematics - Doklady*, 4:1624–1627, 1963.

[191] L.N. Trefethen. Group velocity in finite difference schemes. *SIAM Review*, 24(2):113–136, 1982.

[192] T.E. Vaughan and K. Hynynen. Effects of parameter errors in the simulation of transcranial focused ultrasound. *Physics in Medicine and Biology*, 47:37–45, 2002.

[193] H.A. Van Der Vorst. Bi-CGStab: A fast and smoothly converging variant of Bi-CG for the solution of nonsymmetric linear systems. *SIAM Journal on Scientific and Statistical Computing*, 13(2):631–644, 1992.

[194] N. Vykhodtseva, V. Sorrentino, F.A. Jolesz, R.T. Bronson, and K. Hynynen. MRI detection of the thermal effects of focused ultrasound in the brain. *Ultrasound in Medicine and Biology*, 26(5):871–880, 2000.

[195] R. Weiss. *Parameter-Free Iterative Linear Solvers*. Akademie Verlag, 1996.

[196] C.H. Wilcox. A generalization of theorems of Rellich and Atkinson. *Proceedings of the American Mathematical Society*, 7(2):271–276, 1956.

[197] G. Wojcik, B. Fornberg, R. Waag, L. Carcione, J. Mould, L. Nikodym, and T. Driscoll. Pseudospectral methods for large-scale bioacoustic models. *IEEE Ultrasonics Symposium Proceeding*, 2:1501–1506, 1997.

[198] G. Wojcik, T. Szabo, J. Mould, L. Carcione, and F. Clougherty. Nonlinear pulse calculations and data in water and a tissue mimic. In *IEEE Ultrasonics symposium proceedings*, pages 1521–1526, 1999.

[199] L. T. Yang and R. P. Brent. The improved BiCGStab method for large and sparse unsymmetric linear systems on parallel distributed memory architectures. In *Proceedings of the Fifth International Conference on Algorithms and Architectures for Parallel Processing (ICA3PP-02)*, pages 324–328, 2002.

[200] O. C. Zienkiewicz, R. L. Taylor, S. J. Sherwin, and J. Peiró. On discontinuous Galerkin methods. *International Journal for Numerical Methods in Engineering*, 58(8):1119–1148, 2003.